TECHNISCHE UNIVERSITÄT WIEN

Diplomarbeit

Commissioning and operation of a scaled cold flow model of a 10MW chemical looping combustion demonstration unit

ausgeführt zum Zweck der Erlangung des akademischen Grades eines Diplom-Ingenieurs
unter der Leitung von

Univ.Prof. Dipl.-Ing. Dr.techn. Hermann Hofbauer
Univ.Prof. Dipl.-Ing. Dr.techn. Tobias Pröll
Dipl.-Ing. Klemens Marx

am Institut für Verfahrenstechnik, Umwelttechnik und Technisches Biowissenschaften
E166

eingereicht an der Technischen Universität Wien

Fakultät für Maschinenwesen und Betriebswissenschaften

von

Michael Schinninger, BSc.
0825870
Oppenheimgasse 37/22/11, 1100 Wien

Wien, Juni 2013

Michael Schinninger, BSc.

Danksagung

An dieser Stelle möchte ich mich bei Univ.Prof. Dipl.-Ing. Dr.techn. Hermann Hofbauer und Univ.Prof. Dipl.-Ing. Dr.techn. Tobias Pröll für die Ermöglichung dieser Arbeit an diesem zukunftsweisenden Thema bedanken.

Weiters danke ich Dipl.-Ing. Klemens Marx für die ausgezeichnete Betreuung, die Unterstützung bei der Erstellung dieser Arbeit und für die Bereitstellung des von ihm entworfenen Kaltmodells.

Ein besonderer Dank gilt der Arbeitsgruppe Zero Emission Technologies, die mir mit Rat und Tat zur Seite standen und mich mit einem freundschaftlichen Arbeitsklima willkommen hießen.

Meinen Eltern danke ich besonders für die Unterstützung, die sie mir seit vielen Jahren zukommen lassen, und dafür, dass sie immer an meine Fähigkeiten geglaubt haben.

Auch meinen Kommilitonen unserer Lerngruppe „Team Boris“ gilt ein herzlicher Dank für die gemeinsamen Stunden in der Bibliothek und die fachlichen und weniger fachlichen Diskussionen.

Ein herzlicher Dank gebührt auch Mag.phil. Dr. Theodor Granser der viele Stunden für die sprachliche Korrektur dieser Arbeit aufgewendet hat.

Besonders will ich mich auch bei Dir, Sandra, für dein Verständnis und deine Unterstützung bedanken und deinen Eltern, die mich in Wien herzlich aufgenommen haben.

Abstract

The reduction of greenhouse gases, in particular CO_2, is one of the main tasks of mankind in this century. To deplete or stop the effects of climate change it is inevitable to decrease CO_2 concentration in the atmosphere. As an exclusive energy supply based on renewable sources will not be achievable in the next years, it is necessary to improve available concepts for CO_2 reduction and develop them with regard to commercial applications.

One of these concepts is carbon capture and storage (CCS). In this concept CO_2 formed in combustion process is concentrated and stored. One of the energy efficient ways to separate CO_2 from a combustion process is chemical looping combustion (CLC). This technology uses an unmixed combustion, which means that the formed CO_2 is not mixed with the depleted combustion air. To provide the necessary oxygen for the combustion process, a solid oxygen carrier is used. This solid oxygen carrier is transported between two reactors by a circulating fluidized bed. The so called dual circulating fluidized bed (DFB) is a rector design, which is successfully tested for pilot plant scale (140kW).

To reduce the risks coming up with an up-scaling to 10MW, a cold flow model was designed. This model was scaled up to depict the flow pattern of a full scale plant and to show occurring phenomena.

The study focuses on the commissioning of this 10MW cold flow model of a CLC plant and the first fluid dynamics investigations. For this reason a pressure transmitting system was set up, which opens the possibility to record and display the pressure profiles in the model. These pressure profiles are characteristic for different flow patterns and help to calculate the pressure drops in the full scale plant. Moreover the solids discharge of the recirculation cyclones were optimized to ensure a stable measurement. The bed material discharge could be reduced by a factor of 100, by installing a vortex tube and optimization of the gas outlet position.

To reduce the consumption of materials (steam, air) in the operating full scale plant, fluidization of the loop seals was varied in the cold flow model. This variation leads to an optimal operating point with a reduced fluidization, whereby bed material circulation is held constant. The reductions reached are 15% in the lower loop seal and 30% in the upper loop seal.

To investigate the influence of the fluidization in the reactors on the bed material circulation, a sensitivity analysis was accomplished. The results of this analysis show that the primary fluidization air has the highest impact on the solids circulation rate. The only parameter which has an even higher influence is the inventory in the reactor system.

Kurzfassung

Die Menschheit hat in den nächsten Jahrzehnten eine wichtige Aufgabe, die Ausstoßung von Treibhausgasen und allen voran CO_2 zu reduzieren. Diese Maßnahme ist unumgänglich, um den Klimawandel zu reduzieren bzw. zu stoppen. Da die alleinige Energieversorgung mit regenerativen Verfahren zum heutigen Zeitpunkt und in den nächsten Jahrzehnten nicht möglich sein wird, ist es notwendig, vorhandene Konzepte zur CO_2 Reduzierung in Hinblick auf eine großtechnische Anwendung zu erforschen.

Eines dieser Konzepte ist „carbon capture and storage“, kurz CCS. Hierbei wird das bei einer Verbrennung entstehende CO_2 konzentriert und anschießend gespeichert. Unter den Technologien, die dieses Konzept anwenden, hat „chemical looping combustion“ (CLC) einen besonderen Stellenwert, da es eine besonders energieeffiziente Abtrennung von CO_2 ermöglicht. Diese Technologie wendet eine getrennte Verbrennung an, um die Verbrennungsluft nicht mit dem, in den Abgasen enthaltenen CO_2 zu mischen. Um den Sauerstoff, welcher für die Verbrennung notwendig ist, bereit zu stellen, wird ein fester Sauerstoffträger eingesetzt. Dieser Sauerstoffträger wird mittels zirkulierender Wirbelschichten zwischen den Reaktoren transportiert. Dieses Reaktordesign wird zweifach zirkulierende Wirbelschicht genannt und im Technikumsmaßstab (140kW) erfolgreich betrieben.

Um das Risiko, welches ein Scale-up auf 10MW mit sich bringt, zu reduzieren wurde ein Kaltmodell entworfen. Dieses Kaltmodell wurde dahingehend skaliert, die Strömungszustände in einer Heißanlage abzubilden und auftretende Phänomene untersuchen zu können.

Die vorliegende Studie befasst sich mit der Inbetriebnahme dieses 10MW Kaltmodells einer CLC Anlage und ersten fluiddynamischen Untersuchungen. Dazu wurde ein Druckmesssystem aufgebaut, welches ermöglicht, die Druckprofile im Modell aufzuzeichnen. Diese Druckprofile geben Aufschluss über vorherrschende Strömungszustände und lassen Rückschlüsse auf Druckverluste in der Heißanlage zu. Des Weiteren wurde der Bettmaterialaustrag der vorhandenen Zyklone optimiert, um einen stabilen Messbetrieb zu gewährleisten. Durch Anpassung der Positionen der Gasauslässe und Installation von Tauchrohren wurde eine Reduktion des Bettmaterialaustrages um den Faktor 45 erreicht.

Um den Aufwand an Betriebsstoffen (Luft, Dampf) im Betrieb der Heißanlage reduzieren zu können, wurde die Fluidisierung der Siphone im Kaltmodell variiert. Durch diese Variation konnte ein optimaler Betriebspunkt gefunden werden, welcher bei verringerter Fluidisierung die Bettmaterialzirkulation konstant halten konnte. Durch diese Optimierung konnten im unteren Siphon die eingesetzten Gasmengen um 15 % und im oberen Siphon um 30% reduziert werden.

Der Einfluss der Fluidisierungsluft in den Reaktoren, auf den Bettmaterialumlauf wurde mittels einer Sensitivitätsanalyse ermittelt. Dabei wurde festgestellt, dass die primären Fluidisierungsstufen den großen Einfluss auf den Umlauf haben. Den größten Einfluss auf den Umlauf hat jedoch das vorhandene Bettmaterial im Reaktorverbund.

Table of Content

1 Introduction

1.1 Global warming

Fighting against climate change is one of the biggest challenges society, politics and scientists have to master this century. Greenhouse gases such as carbon dioxide are interacting with the sunlight leading to a temperature increase of the Earth's atmosphere; known as global warming (greenhouse gas effect).

In Earth's history the concentration of CO_2 naturally fluctuated, with peaks being below 280 ppm in the last 650 000 years. Since the Industrial Revolution and the accompanied exposition of carbon stored in fossil fuels the concentration has risen to reach 382 ppm in 2007 [**1**], [**2**].

In 2006, anthropogenically caused carbon dioxide (CO_2) emission had been 36.3 Gt in relation to 550Gt of naturally occurring emission; this is only a small part. Anyhow it is enough to destabilize the natural CO_2 balance [**3**].

The Intergovernmental Panel on Climate Change (IPCC) predicts an increase of global temperature of 1.4-5.8°C in the period from 1990 to 2100 causing:

- arctic ice melting,
- rising of oceanic sea level,
- extreme weather phenomena, and
- defrosting of the perma-frost soil.

These effects of climate change are already affecting the lives of many people. They cause floods, droughts and other weather extremes, which can destroy an entire crop and threaten the base of life of many people.

In 1997, the members of the United Nations Framework Convention on Climate Exchange took the first step and signed the Kyoto Protocol. All members were committed to a reduction of greenhouse gases till 2012 by 5.2% compared to emission levels in 1990 and a trading system when exceeding these limits. Austria's objective was a reduction by 13% which was not reached as shown in Table 1.1. Therefore CO_2-certificats had to be bought from other countries[**4**] such as Spain, the Netherlands, Estonia, and Latvia

Table 1.1: Greenhouse gas emissions trends in Austria from 1990 to 2010 [5]

	1990	2008	2009	2010
Total greenhouse gas emissions Mt CO_2-eq.	78.2	87.0	80.1	84.4
Relative emissions based on emission levels in 1990	100%	111.3%	102.4%	108%

The invention of new and further development of existing CO_2 reduction or prevention technologies is crucial to achieve the agreed emission reduction levels. It is expected that switching to renewable energy production methods cannot be achieved within reasonable timescales [**6**].

1.2 Mitigation strategies

Among today's state of the art technologies, there are some useful measures in order to reduce CO_2 emission from human sources:

- Use of renewable energy sources
- Nuclear power
- Increasing energy efficiency
- Fuel switch
- Carbon capture and storage (CCS)

All these technologies have their advantages and disadvantages, from final disposal of radioactive waste to energy storage problems for renewable energy sources. The CCS technologies have the short-term advantage that some of them can be equipped to commercial power plant, or use common fuels like gas or coal. These advantages make them to transition technologies for a CO_2 free energy production.

As the name says CCS is a technology based on capturing enriched CO_2 and the following storage. CCS only makes sense in large scale units, because it wouldn't be efficient to capture CO_2 from transport or building sector. For profitable compression of CO_2 a highly enriched gas stream is needed. For power plants these four possible ways are common to obtain such a stream.

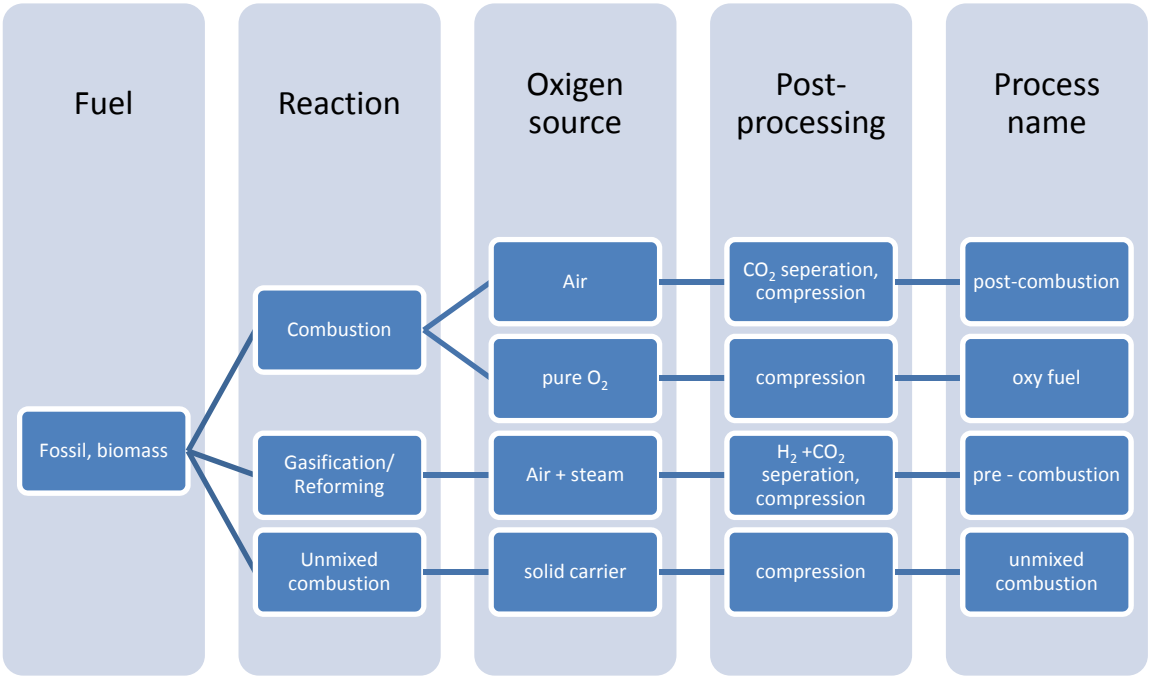

- **Post-combustion capture** is a technology which works with the exhaust gases of common combustion plants. This makes it easy to equip most conventional power plants with post-combustion. The main parts are a CO_2 separation and compression unit. The separation system is based on a chemical absorption and because of low CO_2 concentrations and the high amount of flue gases the separation units get very big. The post combustion process is well developed and pilot plants are successfully implemented in conventional power plants. Because of low CO_2 split off rates and the high costs for flue gas scrubbing this technology is not the most effective possibility.

- **Oxy fuel combustion** uses a pure O_2 stream burning. As combustion with pure oxygen would cause very high temperatures in the vessel, a recirculation of the flue gas is needed. The O_2 stream is normally provided by an O_2 separation unit, which decreases the energy efficiency of the plant. The flue gas mainly consists of H_2O and CO_2 because there is no nitrogen in the combustion air. The water can be separated easily by a condenser.
- **Pre-combustion capture** is a technology in which fuel is converted to synthesis gas in a reforming step. After reforming the syngas reacts with steam to CO_2 and H_2. CO_2 can be separated from the H_2 stream via a pressure swing absorption column. The remaining H_2 can be used for several industrial processes or can be burnt.
- **Unmixed combustion** is based on not mixing fuel and air during the combustion. Oxygen gets selectively bound to a support material in one reaction zone. In another reaction zone fuel is oxidized and generates a flue gas, which mainly contains CO_2 and H_2O. The second generated off gas stream consists of depleted air. The advantage of this technology is that O_2 or CO_2 separation is not needed. This leads to higher efficiencies than other processes.

After separating and compressing the CO_2 it has to be transported, stored or used. The transport can be done with pipelines, tankers and rail tankers. For storage two opportunities are known now.

- **Storage in geological traps** is the only commercially used technology for CO_2 storage nowadays [**7**]. Supercritical CO_2 is pressed in porous rock layers, which are covered by a layer of low permeability rock.
- **Storage in ocean** is applicable in depths where the density of CO_2 is higher than the sea water (about 3000m depth) or dissolved in a so called sinking plume (about 1000m depth). The biggest concern is about the local pH reduction and the influence on aquatic flora and fauna. Because of this uncertainty deep sea storage is not used in technical dimensions.

CO_2 is also used in commercial production processes like the synthesis of urea with ammonia or the synthesis of methanol with hydrogen enriched synthesis gas. Carbon dioxide is as well used in oil production to increase the productivity of oil and gas reservoirs by improving oil mobility.

1.3 Chemical looping

1.3.1 Principle

Chemical looping combustion (CLC) is a so called unmixed combustion process. The oxygen for the oxidation of the fuel is provided from a solid carrier, produced in an oxidation process with the combustion air. The process allows an easy separation of oxygen and nitrogen from the air. To put this into practice, two connected reactors are needed. Figure 1.1 depicts the concept of a chemical looping combustion. In the air reactor (AR) the oxygen carrier (OC) reacts with the oxygen supplied from the air. This OC is then transported to the second reactor, the so called fuel reactor (FR). Here the fuel reacts with the provided oxygen from the OC to CO_2 and H_2O, which are the main components of the FR flue gas. After reduction of the OC in the FR it is transported back to the air reactor where it is oxidized again closing the continuous chemical looping process cycle. The H_2O from the flue gas can be condensed and the remaining CO_2 can be compressed and transported to an adequate storage or used in further processes. The flue gas from the air reactor contains oxygen depleted air, which can be released to the atmosphere without concern. CLC goes along with nearly no energy penalty, only the compression of CO_2, which is needed in all of the CCS technologies, will require additional energy.

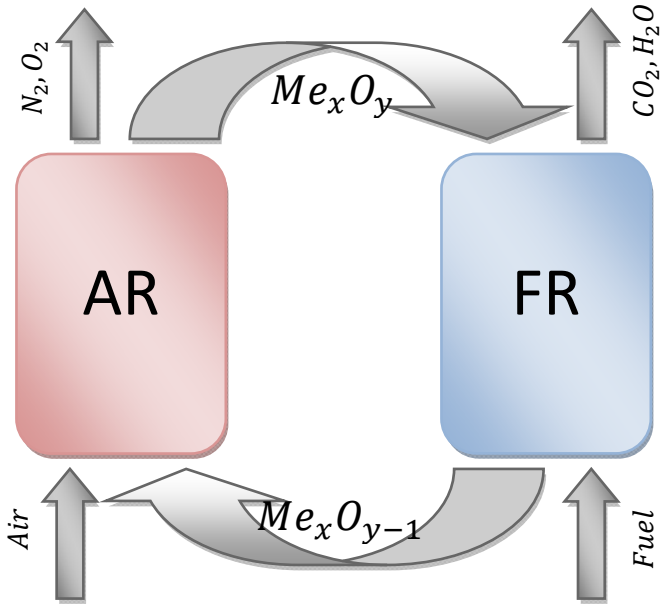

Figure 1.1: CLC-process concept

1.3.2 Reactions

In the air and fuel reactor several reactions occur. The beating heart of CLC is the oxidation and the reduction of the oxygen carrier. The highly irreversible combustion reaction

$$C_nH_{2m} + (2n + m)O_2 \Leftrightarrow nCO_2 + mH_2O \quad (1.1)$$

is separated by the CLC processes in two reactors. The general reaction (1.2) in the AR is given. The oxidation reaction of the fuel in the fuel reactor is shown in equation (1.3). According to thermodynamics the entire energy released has to be the same as in conventional combustion.

$$O_2 + 2Me_xO_{y-1} \Leftrightarrow 2Me_xO_y \quad (1.2)$$

$$C_nH_{2m} + (2n + m)Me_xO_y \Leftrightarrow mH_2O + nCO_2 + (2n + m)Me_xO_{y-1} \quad (1.3)$$

Reaction(1.3)is the result of several reaction steps inside the FR. The most influencing are:

the partial oxidation of the fuel,

$$C_nH_{2m} + nMeO_y \Leftrightarrow nCO + mH_2 + nMeO_{y-1} \quad \textbf{(1.4)}$$

the oxidation of CO and H_2,

$$CO + MeO_y \Leftrightarrow CO_2 + MeO_{y-1} \quad \textbf{(1.5)}$$

$$H_2 + MeO_y \Leftrightarrow H_2O + MeO_{y-1} \quad \textbf{(1.6)}$$

the stream reforming of hydrocarbons

$$C_nH_{2m} + nH_2O \overset{cat.}{\Longleftrightarrow} nCO + (n+m)H_2 \quad \textbf{(1.7)}$$

and the water-gas shift reaction

$$CO + H_2O \overset{cat.}{\Longleftrightarrow} CO_2 + H_2 \quad \textbf{(1.8)}$$

Some oxygen carriers show a behavior called CLOU. The so called CLOU oxygen carriers are able to release free oxygen, whereby other oxygen carriers has to interact with the fuel to get reduced [**8**][**9**]. Reaction (1.9) depicts the release of oxygen by a CLOU oxygen carrier

$$2\ MeO_y \Leftrightarrow 2MeO_{y-1} + O_2 \quad \textbf{(1.9)}$$

The oxidation of the fuel with the released oxygen follows reactions (1.10) and (1.11)

$$C_nH_{2m} + \frac{n}{2}O_2 \Leftrightarrow nCO + mH_2 \quad \textbf{(1.10)}$$

$$nCO + 2mH_2 + \left(\frac{n}{2} + m\right)O_2 \Leftrightarrow nCO_2 + 2mH_2O \quad \textbf{(1.11)}$$

This reaction path occurs parallel to reaction (1.1) with the advantage that the reaction is not heterogeneous, which allows for higher reaction rates. A disadvantage could be that the OC releases to much O_2 and pollutes the FR off gas stream.

Depending on the Oxygen carrier, the released energy in the air reactor is higher or lower compared with direct combustion. This difference will be balanced in the fuel reactor, which needs the remaining energy or provides the missing. Table 1.2 shows the reaction enthalpies of the main oxygen carriers used compared with the reaction heat of direct combustion.

Table 1.2: Reaction enthalpy in the air reactor [10]

Reaction	$\Delta H\ \left(\frac{kJ}{mol}\right)$	$\frac{\Delta H}{\Delta H_{dir,comb}}$
$O_2 + {}^1/_2\, CH_4 \Leftrightarrow {}^1/_2\, CO_2 + H_2O$	-401.39	1.00
$O_2 + {}^4/_3\, Fe \Leftrightarrow {}^2/_3\, Fe_2O_3$	-539.12	1.34
$O_2 + 4FeO \Leftrightarrow 2Fe_2O_3$	-554.29	1.38
$O_2 + 4Fe_3O_4 \Leftrightarrow 6Fe_2O_3$	-481.04	1.20
$O_2 + 2Ni \Leftrightarrow 2NiO$	-467.96	1.17
$O_2 + 2Co \Leftrightarrow 2CoO$	-466.67	1.16
$O_2 + {}^3/_2\, Co \Leftrightarrow {}^1/_2\, Co_3O_4$	-446.65	1.11
$O_2 + 2Cu \Leftrightarrow 2CuO$	-296.25	0.74
$O_2 + 2Cu_2O \Leftrightarrow 4CuO$	-282.82	0.70
$O_2 + 2Mn \Leftrightarrow 2MnO$	-772.49	1.92
$O_2 + 4MnO \Leftrightarrow 2Mn_2O_3$	-359.17	0.89
$O_2 + 6MnO \Leftrightarrow 2Mn_3O_4$	-449.45	1.12

1.3.3 Oxygen carriers

The oxygen carrier has a significant influence on the CLC-process, hence many research groups are focusing in development and optimization of oxygen carriers. Nowadays two kinds of oxygen carriers (OC) are in use or in development, natural and artificial ones. The natural OC, like ilmenite or Fe-ores are mostly cheap and easily available. Artificial OC are normally supported by an inert material, because the active substances are more expensive. Most of the recently studied materials are based on Ni, Fe, Cu, Mn and Co, which are supported by inert materials like Al_2O_3, MgO, TiO_2, $MgAl_2O_4$, ZrO_2, and SiO_2.

- high mechanical stability (limit particle breakage and attrition)
- satisfying reactivity in oxidation and reduction condition
- complete conversion of fuel
- temperature stability over wide range (no sintering or deactivation)
- low costs and high availability
- medical and environmental compatibility
- sufficient oxygen transport capacity R_0

To compare different potential carrier materials Lyngfelt [**10**] defined the oxygen transport capacity ratio as followed:

$$R_0 = \frac{m_{ox} - m_{red}}{m_{ox}} \qquad \textbf{(1.12)}$$

where m_{ox} is the mass of the carrier in the fully oxidized state and m_{red} the mass of the fully reduced carrier. Thus, R_0 describes the oxygen transport capability of the oxygen carrier ranging between 0.02 - 0.1 for typical oxygen carriers [**11**].

Another commonly used characteristic number is the actual degree of oxidation defined as actual mass of the oxygen carrier, m_{actual} divided by the mass difference of the oxygen carrier between fully oxidized state and fully reduced state (equation (1.13)). Where $X_s = 1$ stands for completely oxidized material and $X_s = 0$ means completely reduced matter.

$$X_s = \frac{m_{actual} - m_{red}}{m_{ox} - m_{red}} \quad \textbf{(1.13)}$$

The required oxygen carrier circulation rate is mainly depending on the requirement that sufficient oxygen is transported from the air to the fuel reactor and that enough heat is transported between the reactors. The circulation rate required to fulfill the oxygen balance can be calculated by prescribing the oxygen transport capacity R_0, the stoichiometric amount of oxygen needed for fuel combustion $\dot{n}_{O2,FR}$ and the degree of oxidation of the oxygen carrier at the air reactor exit $X_{s,AR}$ and the fuel reactor exit $X_{s,FR}$.

$$\dot{m}_{OC} = \frac{\dot{n}_{O_2,FR} \cdot M_{O_2}}{R_0 \cdot (X_{s,AR} - X_{s,FR})} \quad \textbf{(1.14)}$$

In practice the minimal required oxygen carrier circulation rate can be derived from (1.7) when fully utilizing the oxygen carrier transport capacity; which is at $X_{s,AR}$=100% and $X_{s,FR}$=0%. Anyhow, since the oxygen carrier temperature is limited, the solids circulation rate is practically limited by the heat transport requirement. This means that typically the oxygen transport capacity of the oxygen carrier is never fully used [**12**].

Although many different particles have been investigated by now, no general recommendation for the best oxygen carrier is given. The best choice is strongly depending on the operating conditions such as the type of fuel used. An overview of particle development strategies for a nickel based oxygen carrier is given in Table 1.3. It is shown that the support material and the sintering temperature of the oxygen carrier are strongly influencing the oxygen carrier performance. The CH_4 index is defined as the fraction of methane leaving the reactor when X_s was between 0.95 and 0.99 and the crushing strength was averaged form 30 particles.

Table 1.3: Spray dried Ni-based oxygen carriers [13**]**

Oxygen carriers with 40 weight-% active NiO		**Sintering temperature**		
		1400°C		1500°C
		Crushing strength	CH_4 index	Crushing strength
Main support	additional support	N	%	N
α-Al_2O_3, CTC3000sg,	5% MgO, Magchem30	2.0	0.69	1.6
$MgAl_2O_4$, CTC55		1.3	2.5	-
α-Al_2O_3, CTC3000sg,	1% MgO, Magchem30	1.6	3.9	2.7
$MgAl_2O_4$, E-SY2000		1.6	1.6	3.5
$MgAl_2O_4$, AR78		2.1	0.13	3.5
α-Al_2O_3, CTC3000sg,	10% MgO, Magchem30	2.5	0.21	5.0

1.3.4 Status

In 1954 Lewis and Gilliland [**14**] patented a CO_2 production process, which should be able to produce cheap and pure CO_2. For this purpose a metallic oxygen carrier should provide oxygen for the combustion of a fuel. The basic idea of chemical looping combustion was born. Richter and Knoche [**15**] re-established the idea in the beginning of the seventies. Instead of CO_2 production their intention was to improve the reversibility of combustion processes by using the concept of unmixed combustion fulfilled by the chemical looping processes. Later, in 1987, Ishida et al. [**16**] introduced the name "chemical looping combustion" first in an evaluation of the potential of CLC for power generation. The first continuous operating chemical looping unit was built in 2004 [**17**] having a size of 10kW fuel input power. Since then the interest is growing in several countries [**18**]. Up to now a 140kW chemical looping unit for gaseous fuels [**19**] and a 100kW unit for solid fuels [**20**] have been built and successfully put into operation. The three main research issues currently being investigated are:

- reactor design,
- scale up and
- oxygen carrier materials.

Figure 1.2 shows the 140 kW pilot rig for chemical looping combustion at Vienna University of Technology. At present this pilot rig has the highest fuel input capacity which is successfully in operation.

Figure 1.2: 140 kW chemical looping combustion plant at Vienna University of Technology

1.4 Objective of this work

To continue the path of bringing chemical looping combustion technology to industrial readiness the reactor design of a potential next scale chemical looping combustion demonstration plant using gaseous fuels at a 10MW thermal input has been developed. Based on this, a cold flow model has been designed and built. Within this work four main objectives have been determined:

- To commission a CLC cold flow model of a 10MW plant. Which means:
  - to install the gas supply for all fluidization stages,
  - to set up a pressure transmitting and recoding system using LabVIEW,
  - to develop a control system for supply pressure, solids control valve and magnet valves,
  - to reach stable measurement conditions and accomplish first fluid dynamic measurements.
- To characterize the particle distribution of the used bed material.
- To optimize the loop seal fluidization by variation of gas distribution.
- To examine riser fluidization influence on the solids flow rate via a sensitivity analysis and the impact of the global inventory.
- To characterize solids control valve (SCV) operation behavior.
- To measure pressure and solids flux with activated bed material cooler for part load operation.

2 Theory

2.1 Fluidization technology

2.1.1 Particle classification

Bed materials used in fluidization technologies are particles of different sizes and shapes. In order to calculate and predict fluidization parameters, the particle properties should be known. The most important ones are:

- particle size distribution,
- particle diameter,
- particle shape,
- particle density, and
- particle porosity.

To characterize the size distribution of the particles they get assigned to classes i with the class range Δx_i defined as follows:

$$\Delta x_i = x_i - x_{i-1} \tag{2.1}$$

where x_i is the particle size of the higher range end and x_{i-1} of the lower end. Equation (2.2) shows the cumulative size distribution $Q_r(x_i)$ which describes the fraction of particles smaller than the particle size of class i. If the quantity of particles in class i is divided by the class range, one obtains the distribution density $q_r(x_i)$ described in equation (2.3).

$$\mathrm{Q_{r,i}} = \mathrm{Q_r}(\mathrm{x}_i) = \frac{amount\ x_{min} \dots x_i}{amount\ x_{min} \dots x_{max}} \tag{2.2}$$

$$\mathrm{q_{r,i}} = \mathrm{q_r}(\mathrm{x}_i) = \frac{amount\ in\ class\ i}{\Delta x_i} \tag{2.3}$$

The correlation between these two equations is as follows:

$$\mathrm{q_{r,i}} = \frac{\Delta Q_{r,i}}{\Delta x_i} \qquad \text{or} \qquad \mathrm{q_r}(x_i) = \frac{\mathrm{d}Q_r(x_i)}{\mathrm{dx}} \tag{2.4}$$

Depending on the measurement method used to quantify the amount of particles in a class, different values of the index r are used. Table 2.1 shows the values of r depending on the measurement method.

Table 2.1: Indexing of measurement method [21]

Indices	Measurement method	Distribution
$\boldsymbol{r = 0}$	number ($\sim x^0$)	$\mathrm{Q_{0,i}}, \mathrm{q_{0,i}}$
$\boldsymbol{r = 1}$	length ($\sim x^1$)	$\mathrm{Q_{1,i}}, \mathrm{q_{1,i}}$
$\boldsymbol{r = 2}$	area($\sim x^2$)	$\mathrm{Q_{2,i}}, \mathrm{q_{2,i}}$
$\boldsymbol{r = 3}$	volume($\sim x^3$)	$\mathrm{Q_{3,i}}, \mathrm{q_{3,i}}$
$\boldsymbol{r = 3^*}$	mass($\sim \rho \cdot x^3$)	$\mathrm{Q_{3^*,i}}, \mathrm{q_{3^*,i}}$

The index 0 stands for a method where the number of particles belonging to a class is determined. One gets a quantity distribution, which is one of the most used distributions. The second often used

distributions are the volume or the mass distribution which are equal when the particle density is independent on the particle size. This distribution can be measured by weighting the particle fractions in the classes by sieving. Figure 2.1 shows the particle size distribution density q_3 and the cumulative distribution Q_3 of the used cold flow model bed material. This distribution varies while the bed material is in use. Due to attrition and agglomeration the range of existing particle sizes can expand.

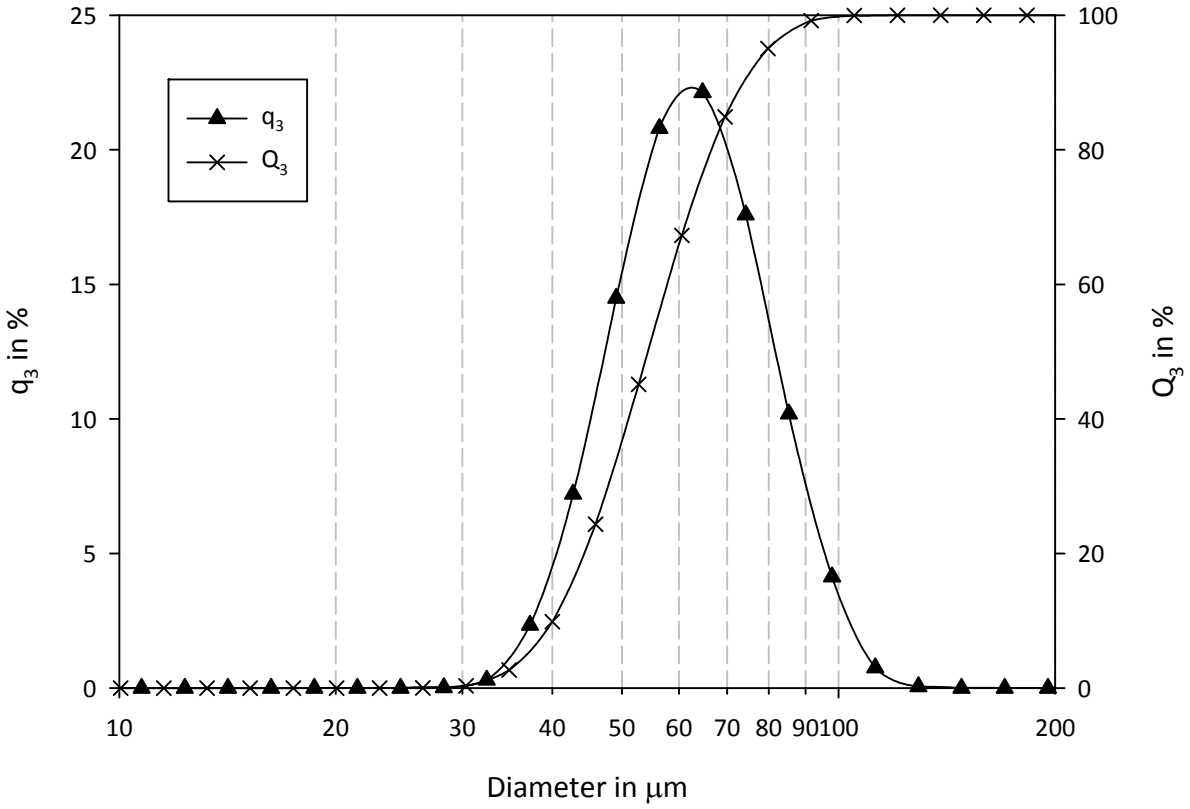

Figure 2.1: Q_3 and q_3 of used cold model bed material

In most cases the detailed information of the particle size distribution would cause complex calculation methods. Therefore for different applications different average diameters are introduced and used. Table 2.2 gives an overview of applicable equivalent particle diameters.

Table 2.2: Overview of applicable equivalent particle diameters

Symbol	Notation	Equation
$\boldsymbol{d_P}$	sieve diameter	-
$\boldsymbol{d_s}$	surface base diameter	$d_S = \sqrt{\frac{S_P}{\pi}}$
$\boldsymbol{d_V}$	volume based diameter	$d_V = \sqrt[3]{\frac{6V_P}{\pi}}$
$\boldsymbol{d_{SV}}$	Sauter mean diameter	$d_{SV} = \frac{6V_P}{S_P}$

In fluidization technologies the Sauter mean diameter is the most commonly used particle diameter. Particles of different size and density show a strongly different behavior when fluidized. Geldart [**22**] introduced a classification of particles allowing a prediction of the fluidization behavior. Particles are arranged in four groups with regard to the main properties such as particle diameter and particle density. The particle groups by Geldart and their main properties are listed below:

Group A: Fine powders with a particle diameter of d_p=30-100 µm and much lower cohesion influence than group C particles. Between U_{mf} and U_{mb} this group shows good fluidization properties and a homogenous bed expansion. Most cracking catalysts belong to group A.

Group B: Particles with a particle size range from 100 to 800μm show no cohesive forces. As soon as U_{mf} is reached the system starts bubbling, so a homogenous phase doesn't exist in this group. Because of heavy bubbling, the solids are very well mixed. Silica sand is a classic representative of this group.

Group C: This group contains very fine particles ($d_p \leq 20\ \mu m$). The cohesive forces cause difficulties when fluidized. Occurrence of plugs and channels is typical for this group. Flour is an example of this group. Fluidization of particles of this group is difficult to obtain and requires mechanisms reducing the influence of the cohesive forces such as vibrations.

Group D: In this group coarse particles ($d_p \geq 1mm$) with high density are located. The system is mainly spouting causing poor solids mixing. Coffee beans and corn fit in this group.

The boundaries between the groups have been evaluated several times. A summary is given by Grace [**23**]. The difference between group A and group B is the occurrence of bubble free fluidization where the bed expansion is homogeneous. Only particles of group A show this behavior. For group B particles minimum fluidization velocity U_{mf} and minimum bubbling velocity U_{mb} coincide. Equation (2.5) is recommended by Grace [**23**] to estimate the A-B boundary region

$$\left(d_p^*\right)_{AB} = 101\left(\frac{\Delta p}{\rho_g}\right)^{-0.425} \quad or \quad Ar_{AB} = 1.03\ x\ 10^6\left(\frac{\Delta p}{\rho_g}\right)^{-1.275} \tag{2.5}$$

For C-A boundary Grace [**23**] provides the following equation:

$$\left(d_p^*\right)_{CA} = 0.68\ to\ 1.1 \quad or \quad Ar_{CA} \approx 0.31.\ to\ 1.3 \tag{2.6}$$

The boundary between group B and D is defined by Grace [**23**] with following conditions:

$$\left(d_p^*\right)_{BD} = 53 \quad or \quad Ar_{BD} = 1.45\ x\ 10^5 \tag{2.7}$$

As the original diagram given by Geldart [**22**] has been evaluated for fluidized beds operated at ambient temperature and pressure using air, Yang [**24**] modified the diagram. The modified diagram (Figure 2.2) shows the dimensionless density versus Archimedes number and powder groups. Defined as followed:

$$Dimensionless\ Density = \frac{\rho_p - \rho_g}{\rho_g} \qquad Ar = \frac{\rho_g \cdot d_{sv}^3 \cdot \left(\rho_p - \rho_g\right) \cdot g}{\mu^2} \tag{2.8}$$

It turns out that Geldart's particle classification is also applicable to fluidized beds at elevated temperature and pressure when extending his diagram using non-dimensional particle characteristics.

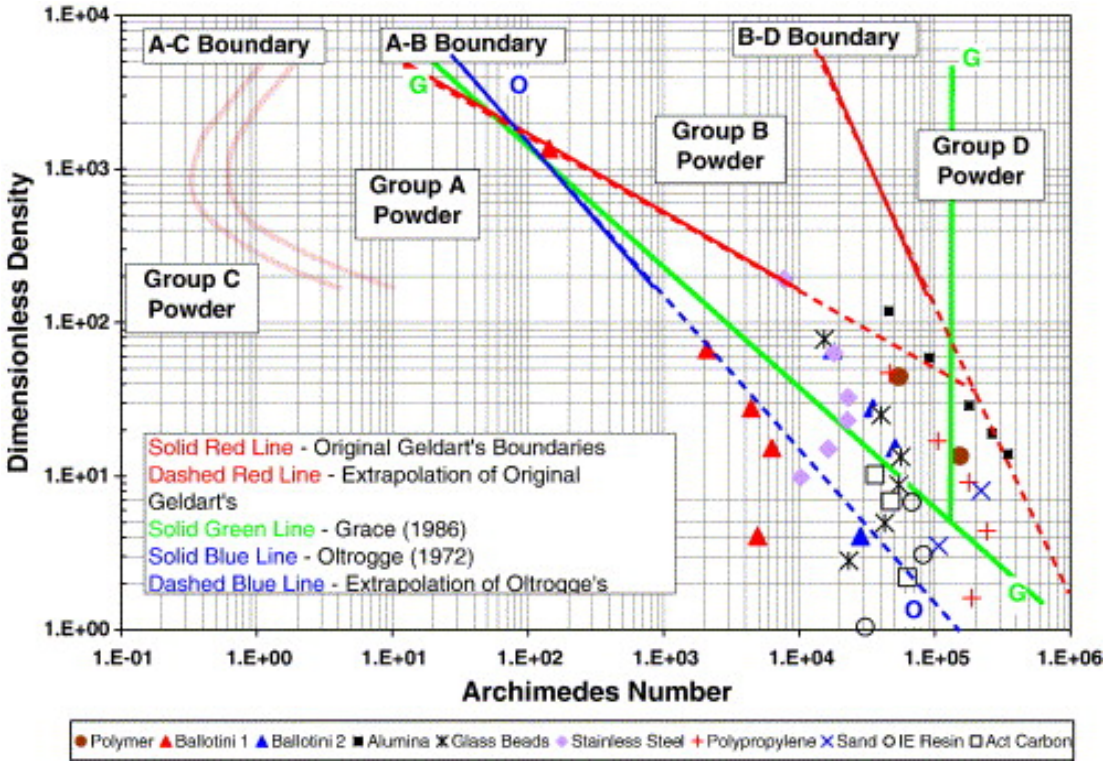

Figure 2.2: Particle classification diagram according to Yang [24] showing the dimensionless density against Archimedes number and different particle groups.

To consider the effect of particle shape the effective diameter (d_{eff}) is used. It describes the particle diameter of a spherical particle showing similar hydrodynamic behavior. To calculate this effective diameter we use a one-parameter calculation which leads to the following equation:

$$d_{eff} = \phi_s \, d_{sph} \tag{2.9}$$

The equivalent spherical diameter d_{sph} can be determined by different measurement methods, such as weighing a certain number of particles or fluid displacement of nonporous particles. It is defined as the diameter of sphere having the same volume as the particle. The second parameter in Equation (2.9) is sphericity ϕ_s, which is defined as the ratio of the surfaces of sphere and particle of same volume [**25**].

Besides particle diameter particle density is an important factor in fluidization technologies. The particle density includes pores and hollows, leading to a smaller density compared to the density of the solid material. Equation (2.10) shows the definition of particle density and equation (2.11) the definition of absolute density.

$$\rho_P = \frac{m_P}{V_P} \tag{2.10}$$

$$\rho_{P_{abs}} = \frac{m_P}{V_P - V_{pores}} \tag{2.11}$$

The definition of the density of the loose bulk of particles is quite similar to particle density and is given as follows:

$$\rho_b = \frac{\sum m_p}{V_b} \tag{2.12}$$

Voidage ϵ is an often used parameter for hydrodynamic calculations. It is defined as the ratio between void space and total volume:

$$\epsilon_b = 1 - \frac{\sum m_p}{\rho_p \cdot V_b} \quad \text{or} \quad \epsilon_b = 1 - \frac{\rho_b}{\rho_P} \tag{2.13}$$

The voidage of the bed material depends on the particle distribution and the mean diameter of it. Particle mixtures with high amount of small particles show smaller voidage, because small particles can fill the void space between the bigger ones. Anyhow, when fluidizing a bulk of particles the porosity changes because of the bed expansion.

2.1.2 Flow regimes

If gas is introduced from below a fixed bed of particles, different two-phase flow patterns will occur. Depending on the gas velocity inside the column different fluidization regimes occur (Figure 2.3). These are fixed bed, delay bubbling or bubble free fluidization, bubbling fluidization, slugging fluidization, turbulent fluidization, fast fluidization and dilute pneumatic conveying.

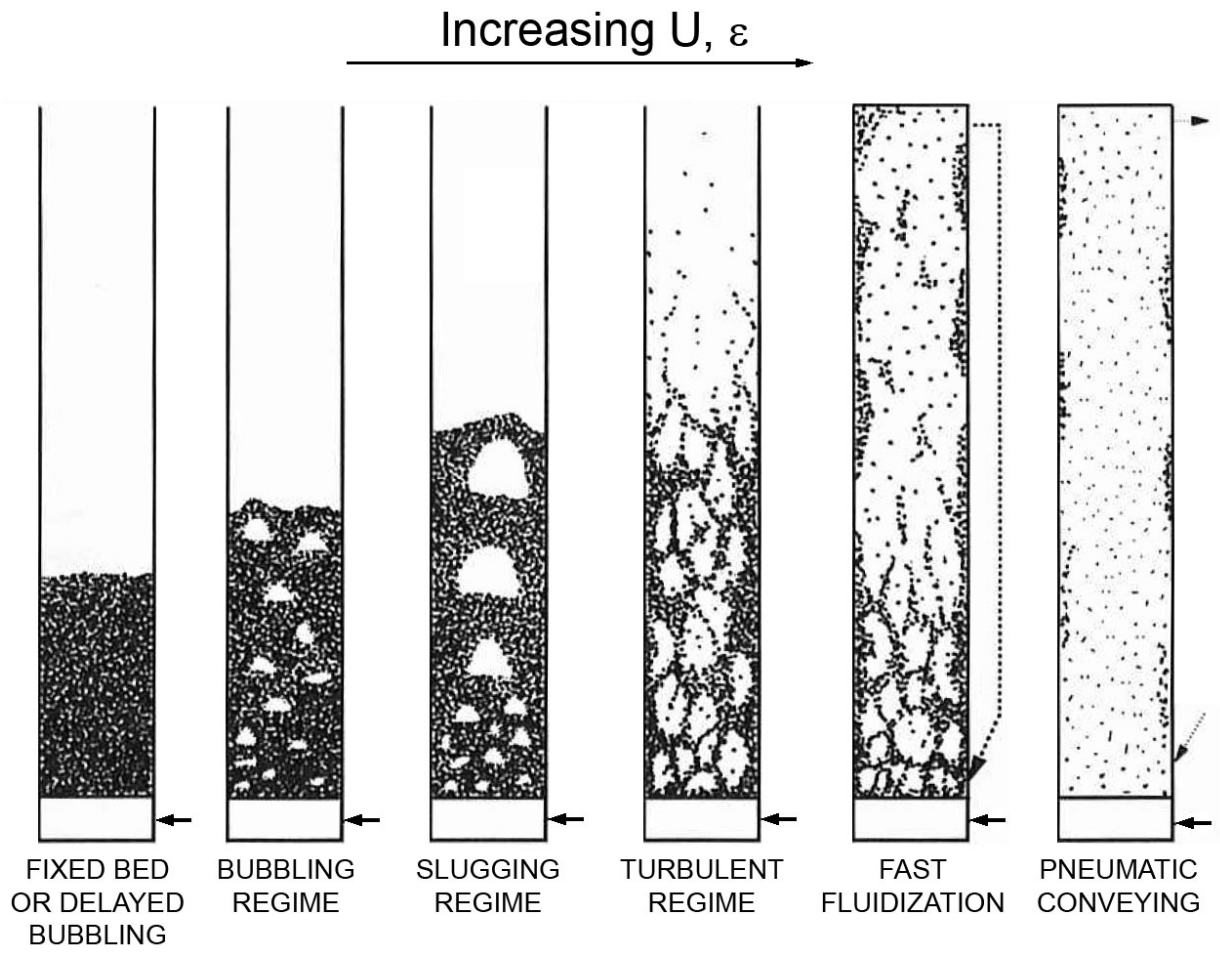

Figure 2.3: Flow patterns in gas-solids fluidized beds [23] (adapted from [12]).

Minimum fluidization velocity U_{mf} is needed to pass over the transition from fixed bed to fluidized bed state. It can be predicted by equation (2.14) after Bi and Grace [**26**].

$$U_{mf} = \frac{\mu_g}{\rho_g \cdot d_p} \cdot \underbrace{\sqrt{27.2^2 + 0.0408\, Ar} - 27.2}_{Re_{mf}} \qquad \textbf{(2.14)}$$

For the particles of Geldart's group A a regime of bubble free fluidization occurs, limited by U_{mf} and the minimum bubbling velocity U_{mb}. U_{mb} strongly depends on particle properties. Geldart and Abrahamsen [**27**] published equation (2.15) to predict U_{mb}.

$$U_{mb} = 33\, d_p \left(\frac{\rho_g}{\mu_g}\right)^{0.1} \qquad \textbf{(2.15)}$$

Increasing the gas velocity causes a growth of bubbles until their diameter gets comparable the reactors diameter. This leads to the point where the flow behavior changes and slugging occurs. In shallow beds this effect doesn't occur, because the bubbles are not able to grow to the required size for slugging [**26**]. According to Steward and Davison [**28**] the minimum slugging velocity U_{ms} can be calculated by the following equation:

$$U_{ms} = U_{mf} + 0.007\sqrt{g\, D} \qquad \textbf{(2.16)}$$

The pressure drop is a useful indicator for the boundary from bubbling regime to turbulent regime. Gas velocity U_c can be estimated by equation (2.17)[**26**].

$$Re_c = 1.24\, Ar^{0.45} \qquad (2 < Ar < 1x10^8) \qquad \textbf{(2.17)}$$

The solids entrainment velocity U_{se} was used by Bi and Grace [**26**] to define the boundary from turbulent to fast fluidization. To calculate U_{se} they developed equation (2.18).

$$Re_{se} = 1.53\, Ar^{0.5} \qquad (2 < Ar < 4x10^6) \qquad \textbf{(2.18)}$$

To get an overview over fluidization regimes of certain fields of application a flow regime diagram can be very useful. The usage of a dimensionless flow regime map with dimensionless velocity U* versus dimensionless particle diameter d_p* as axes is recommended by Bi and Grace [**26**]. The definition of the two parameters is given in equation (2.19).

$$U^* = \frac{Re}{Ar^{1/3}} \qquad d_p^* = Ar^{1/3} \qquad \textbf{(2.19)}$$

With this dimensionless axes and the equations for the transition velocities ((2.15), (2.17), (2.18)) it is possible the draw Figure 2.4. All relevant fluidization regimes are included in this diagram. Below U_{mf}* fixed or packed beds are located, by increasing the velocity between U_{mf}* and U_c* the bed starts bubbling. Further enhancement velocity (between U_c* and U_{se}*) leads to turbulent fluidization.

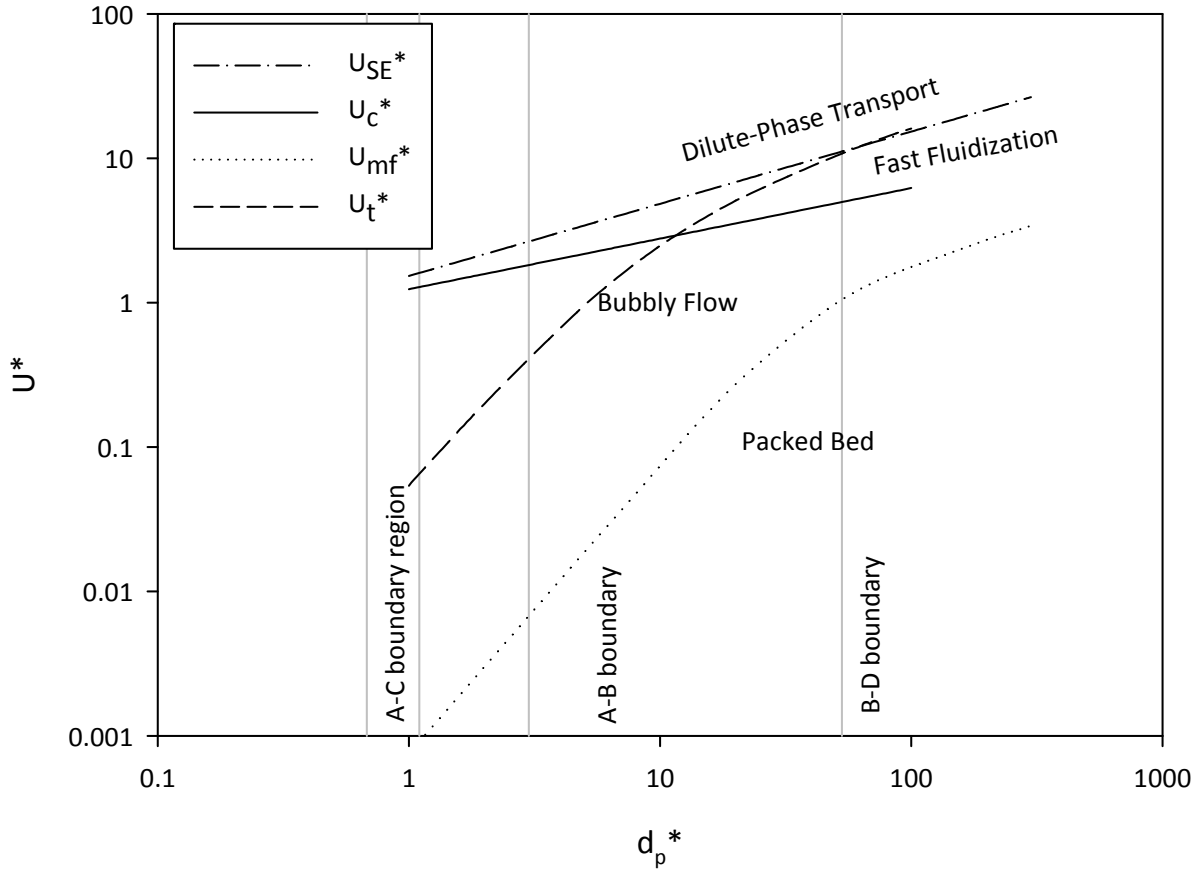

Figure 2.4: Flow regime map adapted from Grace [29]

The force balance of a particle exposed to an upward directed gas flow is given in (2.19). It includes the forces of gravity and buoyancy, friction and acceleration.

$$\frac{\pi(\rho_p - \rho_g)}{6} d_p^3 \cdot g - C_D \cdot A_p \cdot \frac{\rho_g U_0^2}{2} = \frac{\pi}{6} \cdot d_p^3 \cdot \rho_p \cdot \frac{dU_0}{dt} \qquad \textbf{(2.20)}$$

If particle acceleration reaches zero, the particle starts floating. Equation (2.20) can be simplified and the necessary gas velocity is called terminal velocity U_t:

$$U_t = \sqrt{\frac{4}{3} \frac{(\rho_p - \rho_g)}{\rho_g} \frac{d_s \cdot g}{C_D}} \qquad \textbf{(2.21)}$$

The drag coefficient C_D is a function of the Reynolds number. Clift et al. [**30**] proposed an approximation for the drag coefficient in ten regions which are shown in Figure 2.5. The correlations which are used and their range of validity are summed up in Table 2.3.

Table 2.3: Correlations to approximate the drag coefficient, w=log10Re [30]

	Correlation	Range of validity
A	$C_D = \frac{3}{16} + \frac{24}{Re}$	$Re < 0.01$
B	$C_D = \frac{24}{Re} \cdot [1 + 0.1315 \cdot Re^{0.82-0.05 \cdot w}]$	$0.01 \leq Re < 20$
C	$C_D = \frac{24}{Re} \cdot [1 + 0.1935 \cdot Re^{0.6305}]$	$20 \leq Re < 260$
D	$\log_{10} C_D = 1.6435 - 1.1242 \cdot w + 0.1558 \cdot w^2$	$260 \leq Re < 1500$
E	$\log_{10} C_D = -2.4571 + 2.5558 \cdot w - 0.9295 \cdot w^2 + 0.1049 \cdot w^3$	$1500 \leq Re < 1.2x10^4$
F	$\log_{10} C_D = -1.9181 + 0.6370 \cdot w - 0.0636 \cdot w^2$	$1.2x10^4 \leq Re < 4.4x10^4$
G	$\log_{10} C_D = -4.3390 + 1.5809 \cdot w - 0.1546 \cdot w^2$	$4.4x10^4 \leq Re < 3.38x10^5$
H	$C_D = 29.78 - 5.3 \cdot w$	$3.38x10^5 \leq Re < 4x10^5$
I	$C_D = -0.49 + 0.1 \cdot w$	$4x10^5 \leq Re < 10^6$
J	$C_D = 0.19 - \frac{8x10^4}{Re}$	$10^6 \leq Re$

In practice the calculation of U_t requires iteration steps because the Reynolds Number is dependent on it.

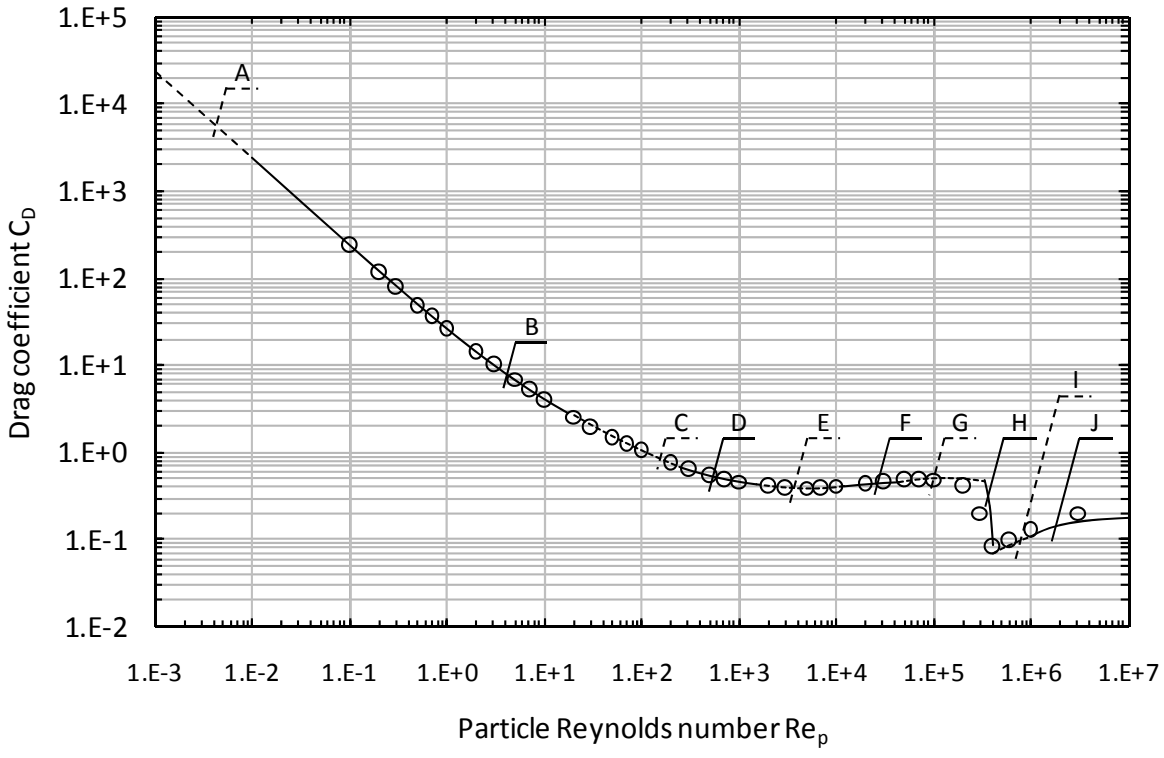

Figure 2.5: Drag coefficient for spheres as a function of the Reynolds Number [31]

2.1.3 Fluid mechanical basics

Since the voidage of a fluidized bed changes with the fluidization state, the actually occurring gas velocity is usually not known. Therefore superficial gas velocity U_0 is used in fluidized bed engineering. It is calculated as follows:

$$U_0 = \frac{\dot{Q}}{A} \tag{2.22}$$

The prediction of the pressure drop in the fixed bed is based on a model of parallel channels which change their diameter. Many scientists observed this fluid dynamical behavior. One correlation, which provides good predictions, is the Carman-Kozeny equation (2.23) [**32**]. This correlation is valid for Re-numbers < 1 where the pressure drop is linearly depending on gas velocity.

$$\frac{\Delta p}{h} = 180\frac{(1-\epsilon)^2}{\epsilon^3}\cdot\frac{\mu_g \cdot U_0}{d_{SV}^2} \qquad Re < 1 \tag{2.23}$$

For Re > 1 where the viscous forces are dominating this linear dependency had been extended by Ergun [**33**] . Equation (2.24) shows the modified Carman-Kozeny equation after Ergun [**33**]

$$\frac{\Delta p}{h} = 150\frac{(1-\epsilon)^2}{\epsilon^3}\cdot\frac{\mu_g \cdot U_0}{d_{SV}^2} + 1.75\cdot\frac{1-\epsilon}{\epsilon^3}\cdot\frac{\rho_g \cdot U_0^2}{d_{SV}} \tag{2.24}$$

The pressure drop in the fixed bed increases with the gas velocity until minimum fluidization velocity is reached. Bubbling fluidized beds are characterized by the equilibration of the forces of bed weight, buoyancy and particle drag. This means that the bed pressure remains constant for bubbling fluidized beds. Equation (2.25) shows a relation to calculate the pressure drop between U_{mf} and U_t.

$$\Delta p \cdot A = A \cdot h_{mf} \cdot \left(1-\epsilon_{mf}\right)\cdot\left(\rho_p - \rho_g\right)\cdot g \tag{2.25}$$

If the gas velocity increases over U_t, the pressure drop increases square-proportionally with the gas speed. At this point the bed material is elutriated from distinct surface of the bubbling fluidized bed. This flow pattern should be impeded in fluidized bed applications because of the high bed material discharge. In circulating fluidized bed technologies this flow pattern is desired.

2.2 Scale-up

2.2.1 General Aspects

Often physical events are too complex to be described analytically without simplification or the calculation time effort is economically not justified. In this case empirical tests are needed to predict the behavior. In engineering science it is often not possible, or connected with high costs, to test behavior in a full scale plant. In mind of this fact the common approach is to start with a bench scale experiment. The next step is a preparative scale followed by a pilot plant scale. In the final step the process is put into commercial scale; this is the most expensive step. Before going to commercial step it is crucial to identify potential problems and to eliminate them to pave the way for a successful commercialization. The typical scale-up approach is shown in Figure 2.6

Figure 2.6: Approach of scale-up taken from [34]

For successful scale-up the detailed knowledge of the scaling laws are necessary to predict the observed effects at a certain scale at another scale. The dimensional analysis is a powerful method to describe these scaling laws.

2.2.2 Dimensional Analysis

In order to be able to describe phenomena in absolute terms scientists have to compare one thing with another. In physics the process of describing an event or object is based on basic properties such as mass, length, speed, shape, time and color. These properties are all referred to something else, so an object has the length of a meter stick or the foot of somebody or the color of an orange. Some of those properties are comparative as “equal” or “unequal” such as e.g. shape or color. Others are also “larger” or “smaller” like length or mass.

The two types of physical properties which appear in quantitative analysis are: base quantities and derived quantities. While base quantities form a complete set of basic blocks, derived quantities are specified by physical operations:

- comparison if two samples **A** and **B** equal or unequal (**A**=**B** or **A≠B)**
- addition of two samples (**A**+**B**=**C)**

They also have to obey the mathematical operation of numbers:

- the identity law (if **A**=**B** and **B**=**C**, then **A**=**C**)
- the commutative law (**A**+**B**=**B**+**A)**
- the associative law [(**A**+**B**)+**C**=**A**+(**B**+**C**)]

This leads to the concept of larger and smaller, subtraction, multiplication and division. To find the underlying base quantities one has to check these specifications. For example the speed of an object can be compared with the speed of another object by resolving if it is either equal or unequal. Furthermore it is evident that the speed is summable and therefore can be adopted as a base quantity. Other properties, such as the color of objects, are comparable, but not summable. This means that the operation of adding the color red to the color red is meaningless since the color remains unchanged. Such an operation is not unique meaning that n.A equals A for any value of n. Anyhow, when going deeper into color physics, one can add to the information of a color the associated wavelength and intensity of the reflected light. This allows applying the above mentioned mathematical operations. Consequently color is not a physical quantity [**35**].

For dimensionless analysis it's important to define a system of units. This system can be defined freely with the restriction to be linearly independent.

For many years many different units for length, temperature or mass have been used. In former times length was often compared with body parts like hands, fingers and weight with stones. Today the common used system is the standardized SI system. Table 2.4 shows the base quantities of the SI system from which the unit of a derived quantity Q can be written in the form of a dimensional product:

$$\dim Q = L^{\alpha} M^{\beta} T^{\gamma} I^{\delta} \Theta^{\epsilon} N^{\zeta} J^{\eta} \qquad \textbf{(2.26)}$$

The exponents are in the form of integers, which can be positive, negative or zero. If all exponents are zero the quantity Q is a so called dimensionless quantity having a unit of 1 [**36**].

Table 2.4: Base quantities and dimensions used in the SI [36**]**

Base quantity		**Dimension**	**Base unit**	
Name	Symbol	Symbol	Name	Symbol
Length	l, x, r etc.	L	meter	m
Mass	m	M	kilogram	kg
Time, duration	t	T	second	s
Electric current	I, i	I	ampere	A
Thermodynamic temperature	T	Θ	kelvin	K
Amount of substance	n	N	mole	mol
Luminous intensity	I_v	J	candela	cd

In order not to compare apples with pears it is necessary that physical equations are dimensionally homogeneous. This means that the numerically describing quantity of a physical event Q_0 has to be calculated from a set of numerical quantities ($Q_1 \ldots Q_n$).following the equation:

$$Q_0 = f(Q_1, Q_2, \ldots, Q_n) \quad \textbf{(2.27)}$$

The principle of absolute significance of relative values says that the equation can only be relevant if Q_0 and f change by the same factor when the base units are changed. For dimensional homogeneity an equation has to follow some restrictions:

- both sides of the equation must have the same dimension,
- all terms in a sum or subtraction must have the same dimension, and
- arguments of special functions (exponential, logarithmic, …) must be dimensionless.

As a consequence the form of a physical equation is independent of the amount of the base units.

The first step in dimensional analysis is to find a complete set of independent variables ($Q_1, Q_2, \ldots, Q_n$) completely describing the physical process or event Q_0. "Completely" means that no other quantity is affecting the value of Q_0 and "independent" that the variables are not connected to each other. Finding the correct set of variables Q_1-Q_n is a key issue in dimensional analysis. After completeness and independence check dimensionless groups are formed like in equation (2.28),

$$\Pi_i = \frac{Q_{k+1}}{Q_1^{N(k+i)1} Q_2^{N(k+i)2} \ldots Q_k^{N(k+i)k}} \quad \textbf{(2.28)}$$

where k is the number of the dimensionally independent subset $Q_1 \ldots Q_k$. If the dimensions of $Q_1 \ldots Q_n$ only contain length, mass and time, k has to be ≤ 3. We also build a dimensionless term for the dependent variable Q_0:

$$\Pi_0 = \frac{Q_0}{Q_1^{N01} Q_2^{N02} \ldots Q_k^{N0k}} \quad \textbf{(2.29)}$$

Now we can write equation (2.27) in an alternative form.

$$\Pi_0 = f(Q_1, Q_2, \ldots, Q_k; \Pi_1, \Pi_2, \ldots \Pi_{n-k}) \quad \textbf{(2.30)}$$

As all physically meaningful equations have to be dimensionally homogeneous, the variables $Q_1 \ldots Q_k$ have to disappear.

$$\Pi_0 = f(\Pi_1, \Pi_2, \ldots \Pi_{n-k}) \quad \textbf{(2.31)}$$

Equation (2.31) follows the Buckingham's Π-Theorem saying:

"When a complete relationship between dimensional physical quantities is expressed in dimensionless form, the number of independent quantities that appear in it is reduced from the original n to n-k, where k is the maximum number of the original n that are dimensionally independent" [**35**].

We now are able to describe the event Q_0 in the reduced form (2.31) allowing a significant reduction in measurement effort.

Assuming that we have two systems, 1 and 2, with the same physical phenomena occurring, but which actually are different, one can say under particular conditions, that the systems are similar, if the dimensionless terms of system 1 and 2 are equal.

2.2.3 Difficulties in scaling

The main factor in successful scaling is the set of used independent quantities. The use of wrong or too many quantities can completely damage the effectiveness of the dimensional analysis or reduce the simplification. Too many quantities can lead to an unnecessarily complicated equation. To find a complete set of independent quantities and to build the dimensionless form are the most important steps and can affect the results significantly.

The next possible problem is to find materials which lead to the same dimensionless numbers as in the full scale process. To simulate for instance the flow pattern of a fluidized bed with cold air, the bed material size has to be smaller and the particle density has to be higher than in a large plant. This leads to the problem that not all dimensionless numbers can be exactly the same value in the model as in the full scale process. Additionally natural constants, i.e. earth gravitation, can cause problems in experiment design since they typically don't distinguish between model and plant.

2.2.4 Scaling in fluidized bed systems

Leon R. Glicksman [**37**] applied the dimensional analysis to find dimensionless groups describing gas and solids motion in fluidized beds. These should be capable to predict the fluid-dynamical behavior between a model and the corresponding plant. These dimensionless numbers are summarized in Table 2.5:

Table 2.5: Full set of scaling relations by Glicksman [37**]**

Dimensionless Number	Equation
Reynolds number	$Re_p = \frac{d_P \cdot U \cdot \rho_G}{\eta_G}$
Froude number	$Fr_p = \frac{U^2}{g \cdot d_P}$
Density ratio	$\frac{\rho_P}{\rho_G}$
Bed height to particle diameter ratio	$\frac{H_B}{d_P}$
Bed diameter to particle diameter ratio	$\frac{D}{d_P}$
Sphericity	ϕ_s
Particle distribution	-

Additional to the full set of dimensionless numbers the dimensionless circulation rate and the simplified Archimedes number can be defined. These Dimensionless numbers are not linear independent from the full set.

Table 2.6: Additional dimensionless Numbers[38**]**

Dimensionless Number	Equation
Dimensionless solids circulation rate	$\frac{G_S}{\rho_P \cdot U}$
Simplified Archimedes number ($\rho_P \gg \rho_G$)	$Ar = \frac{\rho_P \cdot \rho_G \cdot d_P^3 \cdot g}{\eta_G^2}$

The cheapest way to scale a hot fluidized bed is to use a model operated with air at ambient temperature and pressure. This leads to one unique set of operating conditions in the model. The application of this set of equations often leads to very large model referring to model geometry. Therefore Glicksman et al [**37**] simplified the scaling relationships and verified their accuracy [**39**].

The following derivation refers to low Reynolds numbers where the Ergun equation (2.24) contains only the first term. Thus,

$$\frac{\beta \cdot h}{\rho_p \cdot U_0} \rightarrow 150 \frac{(1-\epsilon)^2}{\epsilon^3} \cdot \frac{\mu_g \cdot h}{\rho_p \cdot U_0 \cdot (\phi_s \cdot d_P)^2} \; for \frac{\rho_g \cdot U_0 \cdot d_p}{\mu_g} \rightarrow 0 \qquad \textbf{(2.32)}$$

For the minimum fluidization velocity, at this limit, it can be written,

$$\frac{\Delta p}{L} = \left(\rho_p - \rho_g\right) \cdot g \cdot \left(1 - \epsilon_{mf}\right) = 150 \frac{\left(1-\epsilon_{mf}\right)^2}{\epsilon_{mf}^3} \cdot \frac{\mu_g \cdot U_{mf}}{(\phi_s \cdot d_P)^2} \qquad \textbf{(2.33)}$$

Neglecting the density difference ρ_p-ρ_g and replacing it by ρ_p leads to,

$$u_{mf} = \frac{\rho_p \cdot g \cdot \left(1-\epsilon_{mf}\right)}{\left[150 \frac{\left(1-\epsilon_{mf}\right)^2}{\epsilon_{mf}^3} \cdot \frac{\mu_g}{(\phi_s \cdot d_P)^2}\right]} \qquad \textbf{(2.34)}$$

Substituting equation (2.34) into equation (2.32) leads to,

$$\frac{\beta \cdot h}{\rho_p \cdot U_0} = \frac{g \cdot (1-\epsilon)^2}{U_{mf} \cdot \left(1-\epsilon_{mf}\right) \cdot \epsilon^2} \frac{\epsilon_{mf}^3 \cdot h}{\rho_p \cdot U_0} \qquad \textbf{(2.35)}$$

and

$$\frac{\beta \cdot h}{\rho_p \cdot U_0} Fr = \frac{U_0}{U_{mf}} \frac{(1-\epsilon)^2 \cdot \epsilon_{mf}^3}{\epsilon^2 \cdot \left(1-\epsilon_{mf}\right)} \qquad \textbf{(2.36)}$$

Equation (2.35) and (2.36) guarantee that for low particle Reynolds numbers $\beta \cdot h/\rho_p \cdot U_0$ remains identical, if u_0/u_{mf}, ϵ_{mf} and Fr are held constant. Concerning the influence of ϵ_{mf}, the particle diameter and sphericity have to be constant. With these insights the governing parameters from Table 2.5 can be reduced to the simplified ones:

$$Fr_D = \frac{U_0^2}{gh}, \frac{\rho_p}{\rho_g}, \frac{U_0}{U_{mf}}, \frac{h_1}{h_2}, \frac{G_S}{\rho_P U_0}, bed\ geometry, \phi\ , particle\ size\ distribution \qquad \textbf{(2.37)}$$

Glicksman [**39**] showed that the same set of dimensionless parameters applies for high Reynolds numbers too.

2.2.5 Cyclones

Since the invention of cyclone in 1886 by O.M. Morse [**40**], many different types of cyclones have been designed and many calculation models have been invented. In general a cyclone is used to separate solids from a gas stream by using centripetal forces. The field of application of modern cyclones is very wide. From dust separators in vacuum cleaners to high temperature multi-cyclones in emission control systems, cyclones of different shape and design are used. Typically a cyclone consists of 4 parts,

- gas inlet,
- body with cylindrical and conical part,
- gas outlet and
- solids outlet.

These 4 parts can be modified for the special needs of the separation task. Figure 2.7 shows different gas inlet designs for cyclones, whereby all designs have advantages and disadvantages for specific tasks. The multitude of variable parameters makes it hard to find the best design.

One of the most important factors for the design of a cyclone is the solids load which is defined as the ratio of solids mass $\dot{m}_S$ to gas mass $\dot{m}_g$.

$$\mu_S = \frac{\dot{m}_S}{\dot{m}_g} \tag{2.38}$$

In CFB applications high solids loads of 5 to 15 are common [**41**]. For these recirculation cyclones several design optimizations are proposed [**42**], [**43**], [**44**], such as vortex tubes, eccentric gas outlets and special gas inlets.

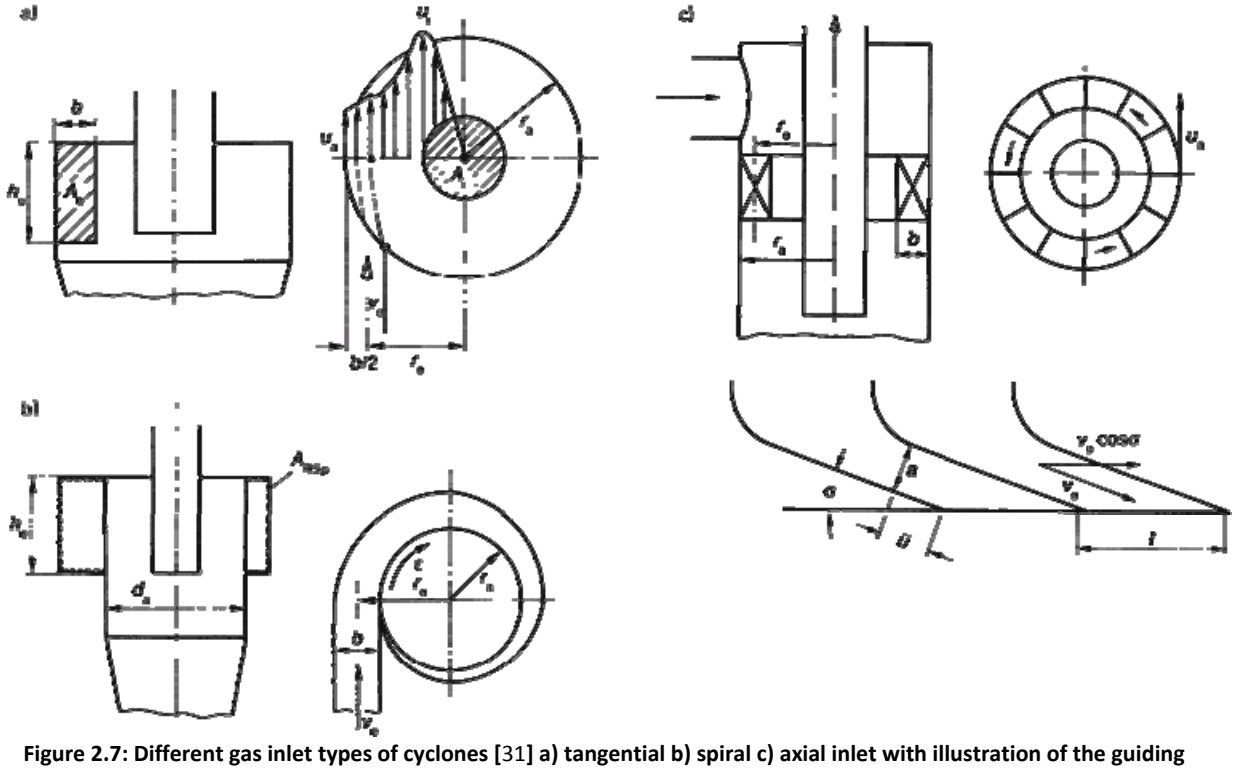

Figure 2.7: Different gas inlet types of cyclones [31] a) tangential b) spiral c) axial inlet with illustration of the guiding blades

2.2.6 Linear sensitivity analysis

The linear sensitivity analysis is a method to show the influence of a variable parameter on a dependent variable. The main point is that only one parameter is varied in a range around a standard point where the system is reacting in a linear way. Otherwise the error in case of linearization is too high.

This method is used in the present work to show the influence of the different fluidization stages on the global and internal solids flow. The dependent variable is Gs_i and the variable parameters are the gas flow rates V_j, whereby i stands for AR und FR and j for the different fluidizations like AR primary, AR secondary and so on.

The sensitivity is then defined as

$$S_{i,j,\pm 10\%} = \frac{\Delta Gs_i(\pm 10\%)}{\Delta V_j(\pm 10\%)} \quad \textbf{(2.39)}$$

where ΔGs_i is

$$\Delta Gs_i(\pm 10\%) = \frac{Gs_i(+10\%) - Gs_i(-10\%)}{Gs_i(stand.)} \quad \textbf{(2.40)}$$

and ΔV_j

$$\Delta V_j(\pm 10\%) = \frac{V_j(+10\%) - V_j(-10\%)}{V_j(stand.)} \quad \textbf{(2.41)}$$

Analogously to this the sensitivity for ±20% is defined.

This procedure makes is possible to show the influence of many variables in one graph. But it is important to mention that the interactions of different parameters are not included in this kind of analysis.

2.2.7 DFB Systems

The development of dual fluidized bed systems at Vienna University of Technology has started in the 1970's. Since then many different dual fluidized bed systems have been designed, because for every application different requirements are needed. The main differences are the flow pattern in the two fluidized beds. The differences range from bubbling regime to fast fluidization in both reactors. Depending on the application, the designs were modified to get optimal conditions. Figure 2.8 a) shows an early combustion reactor design with two bubbling beds, where in the upward zone the secondary combustion air is preheated. In Figure 2.8 b-d) one can see fast fluidized beds combined with bubbling beds.

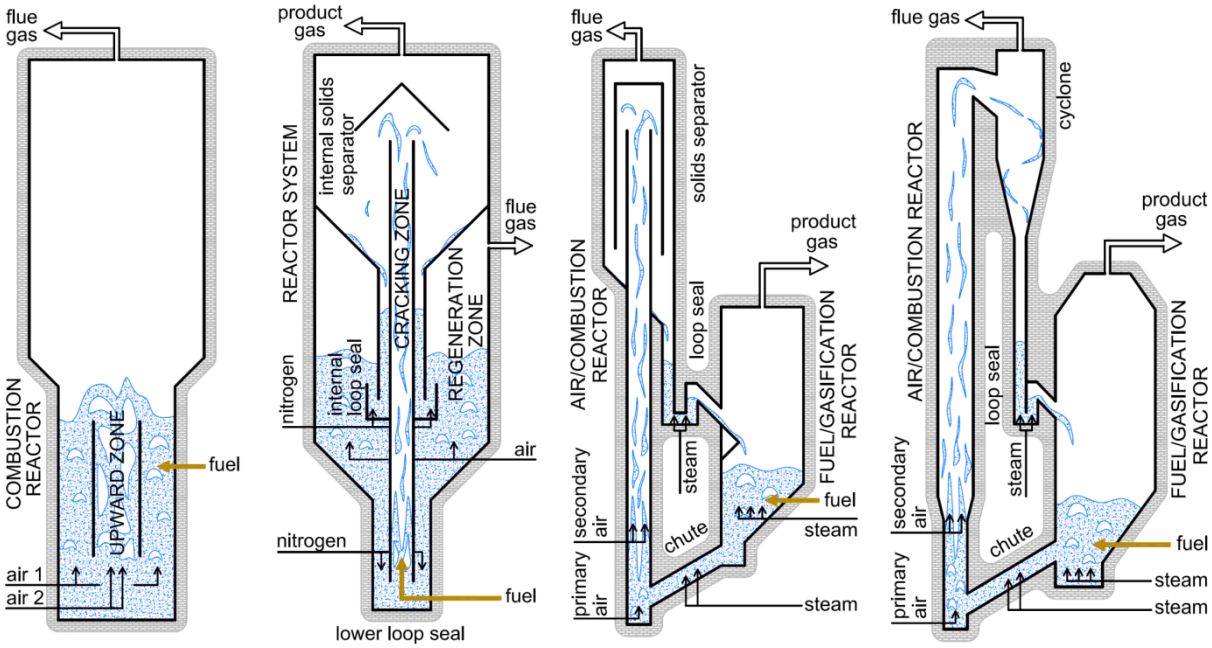

Figure 2.8: Different DFB systems a) early combustion reactor b) FCC reactor c) and d) gasifiers reactor system [45**]**

In chemical looping applications the gas-solids contact is crucial because of the occurring heterogeneous reactions in the air reactor and fuel reactor. The challenge is to increase the gas-solids contact time and provide the required solids circulation rate, which is needed for heat and oxygen transport, should be high enough. With respect to these requirements at least one of the reactors must have a fast fluidization or pneumatic conveying regime.

In the fuel reactor the reaction rate is obviously lower than in the air reactor [**46**], which leads to a significantly higher influence of gas-solids contact time. In bubbling bed fuel reactors the gas bypass through the bubble phase is problematic because no chemical looping reactions are expected in the solids-free bubbles. This Problem can be minimized by deep bed and low fluidization numbers. As mentioned in chapter 2.1.2 slugging is an issue which should not be neglected in very deep beds. Low fluidization numbers require high reactor cross section areas, high solids inventories and cause large bed pressure drops. Additionally, the particle free freeboard is lost reactor volume, because no relevant chemical looping reactions are expected in the absence of solids. Turbulent or fast fluidized beds have the advantage of low solids inventory. This fact can reduce the investment costs for the bed material for an increasing plant. The second advantage is that the whole reactor height is available for the gas solids contact [**47**].

To optimize CLC operation, the reactor design should fulfill the following requirements [**12**]:

- optimal gas-solids contact in both reactor zones,
- high global solids circulation for sufficient oxygen transport,
- low reactor footprint for upscale, and
- simple operation.

To satisfy these requirements the dual circulating fluidized bed system (DCFB) has been developed at Vienna University of Technology [**48**],[**49**]. It consists of two circulating fluidized beds (CFB). The designs shown in Figure 2.9 fulfill the scale-up relevant issues such as low reactor footprint, high gas-solids interaction and low inventory. Basically, the design incorporates two solids loops: the global

loop and the internal loop. The entrained bed material from the AR is separated by a cyclone and sent to the upper loop seal (ULS). This loop seal is fluidized by steam and avoids gas exchange between the AR and the FR. The global loop is closed by the FR and the lower loop seal which transports the solids back to the AR. The internal solids loop including the fuel reactor is closed by the fuel reactor cyclone, and the internal loop seal. One advantage of DCFB concept is the lower loop seal, which stabilizes the solids and acts like a hydraulic link. The LLS also allows a largely independent operation of the two solids loops. Thus the FR can be operated with respect to maximum fuel conversion. The DCFB reactor system also avoids solids accumulation as long as the loop seal is fluidized properly.

The maximal temperatures for the heat integration of a chemical looping system are limited by the specific properties of the oxygen carrier. Depending on agglomeration tendency and material melting point of the oxygen carrier maximal temperatures reached are between 800 and 1000°C. As the adiabatic combustion temperature for an air/fuel ratio of 1.1 is in the range of 1900°C, the excess energy has to be withdrawn. This can be done by cooling the bed material in an external heat exchanger or by direct cooling of the reactor vessels. In fluidized bed applications evaporative water walls can be used to cool the vessel. In this case the heat transfer between bed material and water varies with vessel temperature and solids-wall contact [**50**]. These parameters cannot be influenced significantly by the operator. Therefore off-design load operation is difficult if only water walls are used. To avoid this problem most CFB applications are using fluidized bed heat exchangers controlled by e.g. a solid control valve. In order to keep the size of this heat exchanger within reasonable limits, a combination of both equipments is assumed to be the most effective.

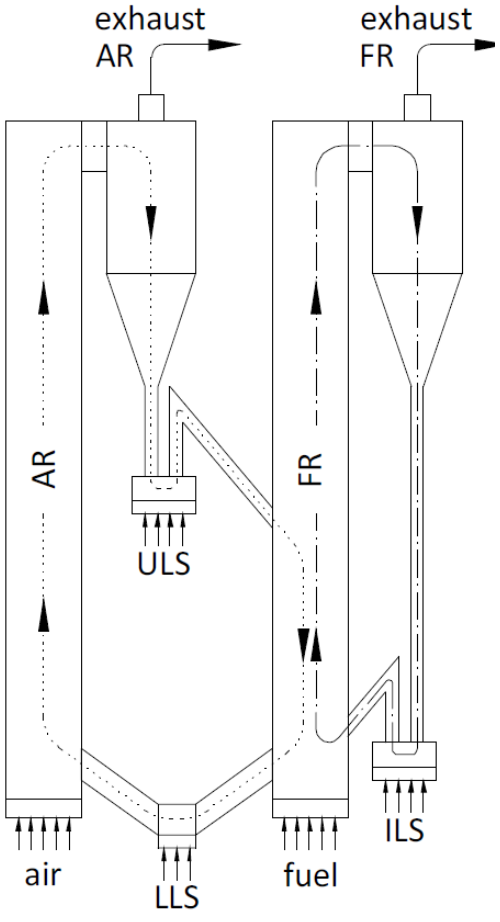

Figure 2.9: Scheme of a DCFB concept [51**]**

3 Experimental

3.1 Description of the CFM

Based on the design of a potential next scale chemical looping demonstration plant developed by Marx et. al. [**47**] a cold flow model has been developed. The basic design requirements were:

- Size: 10MW fuel input power (or thermal power)
- Fuel: natural gas
- Dual circulating fluidized bed concept
- Use of experience gained in CLC operation and design
- Keeping track of commercial used components in fluidized bed applications

On this basis the following characteristic plant parameters have been determined by Marx et al. [**52**]:

Table 3.1: Characteristics of the full scale plant [52**]**

Item	Symbol	Value	Unit
Fuel input power (based on LHV)	P_{fuel}	10	MW
Fuel	$-$	CH_4	-
Fuel reactor temperature	ϑ_{FR}	900	°C
Air reactor temperature	ϑ_{AR}	960	°C
Global air/fuel ratio	λ	1.1	-
Fuel flow rate	V_{fuel}	1 005	Nm³/h
Air flow rate	V_{air}	10 786	Nm³/h
FR exhaust gas flow rate	$V_{FR,exh}$	12 932	m³/h
AR exhaust gas flow rate	$V_{AR,exh}$	39 786	m³/h
FR circle cross-section area	A_{FR}	Ø 0.9m→0.636	m²
AR rectangular cross-section area	A_{AR}	1.2x1.2m→1.44	m²
FR superficial outlet velocity	$U_{0,FR}$	5.65	m/s
AR superficial outlet velocity	$U_{0,AR}$	7.67	m/s
Riser height	H	~15	m

In the chosen design only the AR is equipped with water walls because the AR reactions are always strongly exothermal. Depending on the oxygen carrier (Table 1.2) the reactions in the FR are endothermic or exothermic. The external fluidized bed heat exchanger is placed in the return loop of the air rector, between ULS and AR. The benefits of this arrangement are:

- possibility of part load operation,
- controllable solids flow through the bed material cooler,
- the bed material cooler can be fluidized by air,
- the fluidization air takes part in the air reactor oxidation.

Figure 3.1 shows the used CFM design based on a dual circulating fluidized bed concept (DCFB). With respect to the heat transport of the full scale plant the CFM possesses a bed material cooler and a quadratic air reactor cross section, which is usual if finned walls are applied. At the top of the AR and FR two cyclones are attached to recycle the bed material and separate the flue gas.

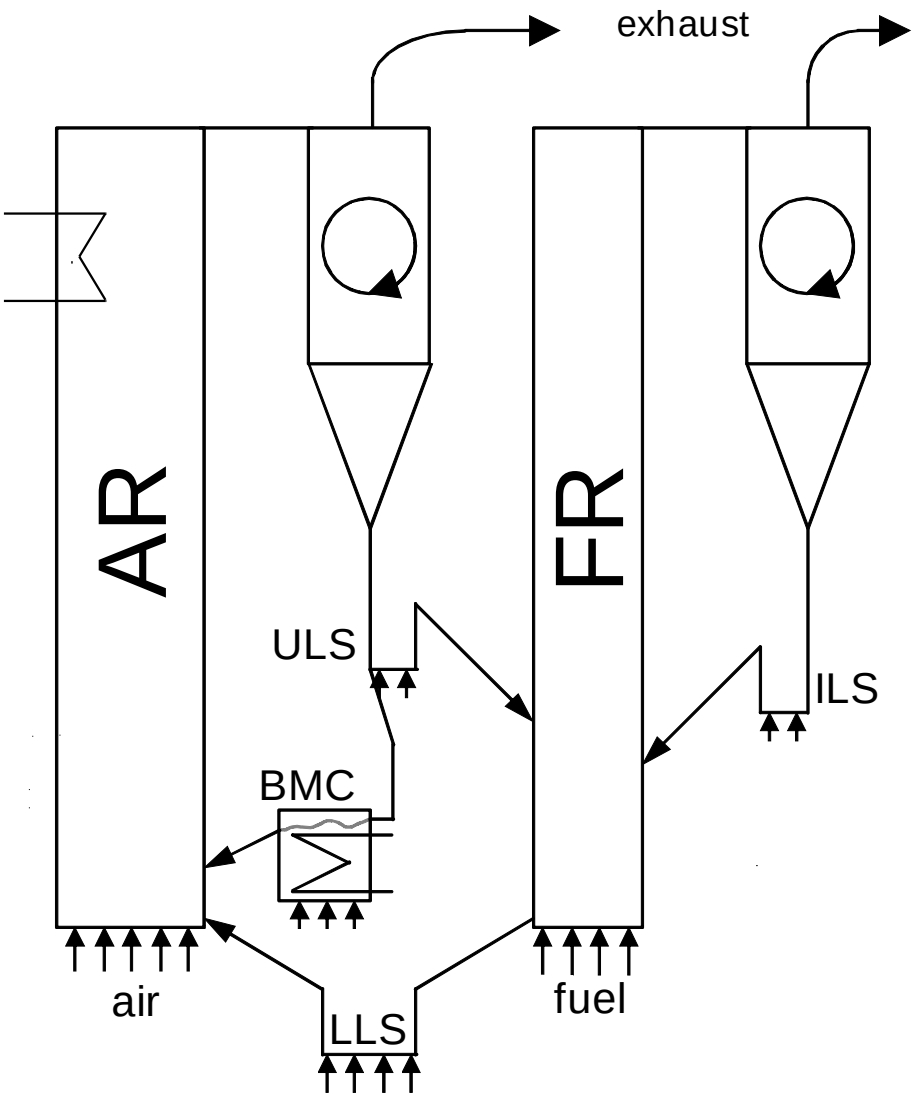

Figure 3.1: Scheme of the used DCFB concept [47**]**

To reach a consistent fluidization over the risers' height and to control the solids flow rate, the air reactor has additional air inlets for the primary, secondary and tertiary combustion air, shown in Figure 3.2. The fuel reactor also has additional gas fluidization stages. These are necessary to account for the formation of CO_2 and H_2O during combustion. According to equation (3.1) the combustion of i. e. CH_4 causes a tripling of the volume. This causes a three times higher gas flow in the full scale plant at the fuel reactor exit than at the FR inlet.

$$CH_4 + 4Me_xO_y \rightarrow CO_2 + 2H_2O + 4Me_xO_{y-1} \quad \textbf{(3.1)}$$

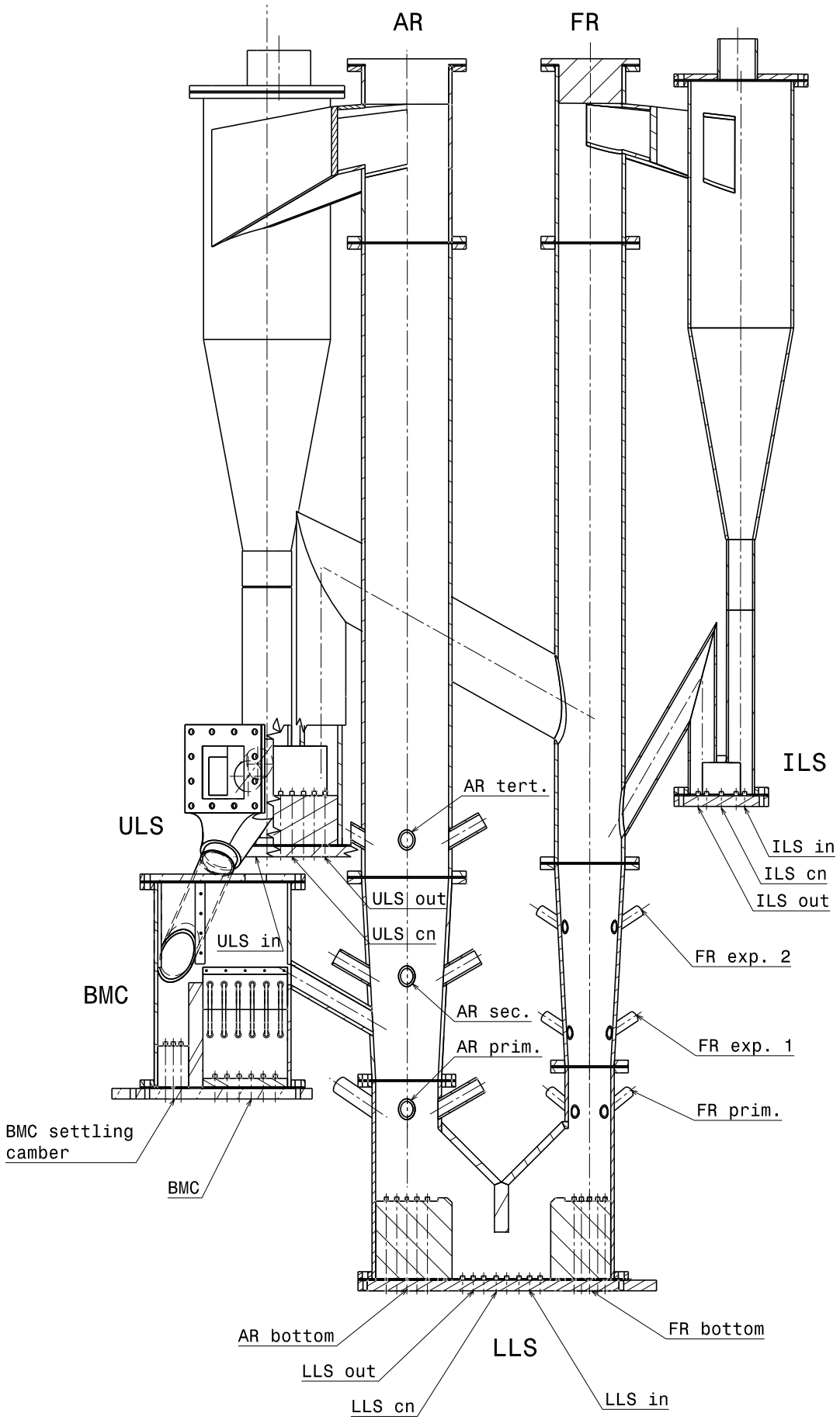

Figure 3.2: Sketch of the used CFM

The gas distribution at the primary air reactor and fuel reactor gas inlets and the loop seals is obtained through gas distribution by small nozzles made of sintered metal; in this case silencers used in pneumatic systems (Figure 3.3). For a steady fluidization the pressure drop through the valves has to be sufficiently high to obtain a homogeneous gas distribution [**25**].

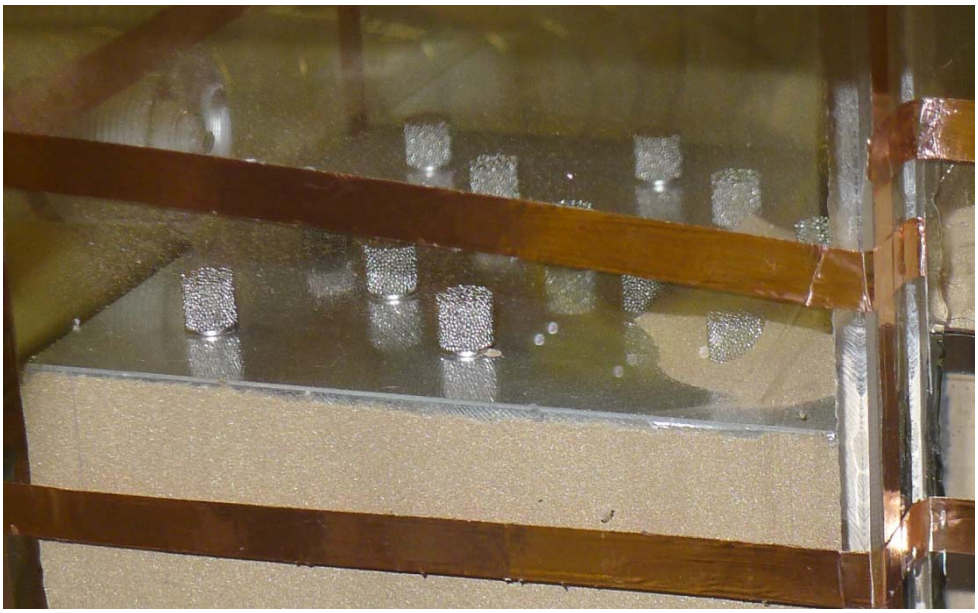

Figure 3.3: Fluidization valves

To study the operation of the loop seals in detail the fluidization area has to be divided into three areas as shown in Figure 3.2.

Between ULS and BMC a solids control valve (SCV) is installed (Figure 3.4). It consists of a stainless steel cone, which is moved by a computer controlled multiphase stepper motor. This cone opens and closes a hole in the ULS wall and can control the solids transport to the bed material cooler.

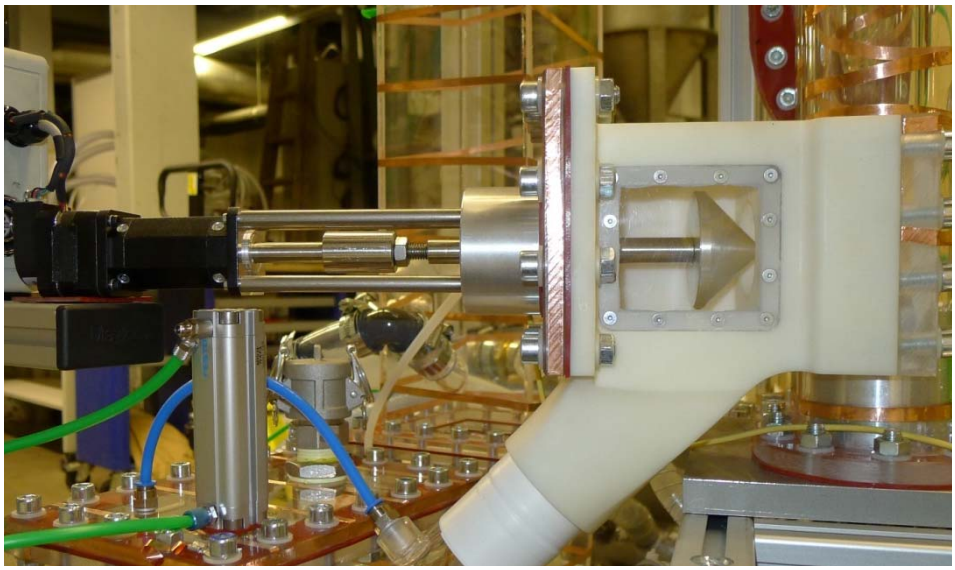

Figure 3.4: Solids control valve

The bed material cooler consists of a settling chamber and a heat exchanger chamber. To determine the quantity of solids flowing to the BMC a pneumatic slider is placed and the accumulation of solids in the chute from the ULS to the BMC is determined.

Both chambers of the BMC are fluidized with air. This fluidization is needed to allow the solids transport across the BMC. As depicted in Figure 3.2 the solids leave the BMC over a slide directing the solids back to air reactor.

To approach the pressure drops and flow pattern in the BMC the cooling elements which would be needed in the full scale plant are executed as scaled plastic pipes (Figure 3.5).

In the lid of the BMC a refill valve is placed needed to fill in new bed material or recycle deposited material from the exhaust gas filters.

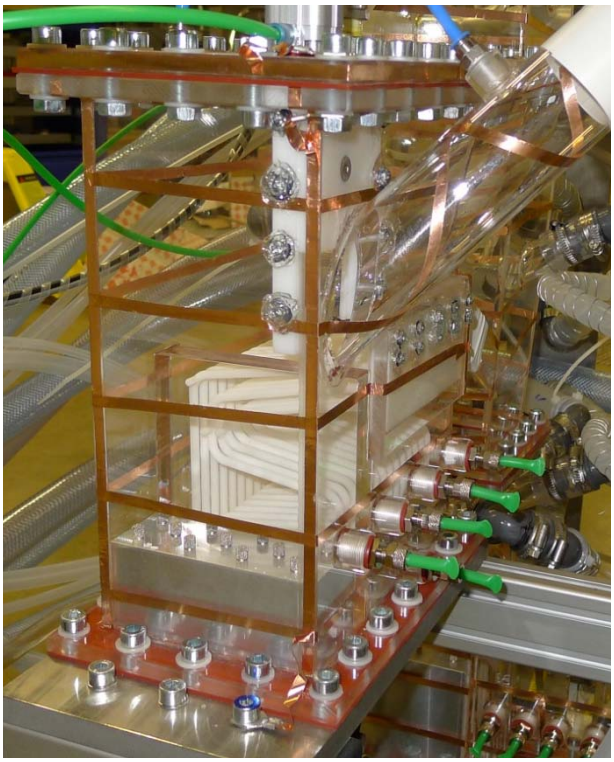

Figure 3.5: Bed material cooler

To separate the solids from the air in the Reactor two cyclones are attached behind the risers. The gas inlets of these cyclones are tangential and designed according to Hugi [**53**] for high solids loads.

The air leaving the cyclones is cleaned by two cyclone filter combinations from Mann+Hummel (Europiclon 800 & 400). The special design of these filter combinations allows an easy evaluation of the discharged bed material. The collecting containers can be dismantled and weighted, allowing a fast quantification of the discharged material.

To measure the pressure distribution inside the system several pressure measurement ports are distributed over the whole model. To prevent bed material from blocking the pressure ports cotton wool is used.

As the bronze bed material reaches high velocities, the whole acryl glass parts charge themselves by electrostatic forces. To avoid sediments and electrical shocks the whole model is lagged with a self-adhesive copper strap connected which is grounded.

3.1.1 Air supply

The main air supply is a 10 bar(g) pressure line, which can handle a maximum of approximately 450 Nm^3/h provided by a screw compressor and a gas cooler package (Mahle MSK-G 45kW/10bar). The pressure of the supply air is reduced by an automatic pressure controller to 7 bar(g). This air then is distributed to several variable area flow meters. After the variable area flow meters the air flow rate is controlled by valves and the air is supplied the CFM using.

The different fluidization places are shown in Figure 3.2, where the gas flow to the loop seals can be stopped by magnetic valves attached to the gas distribution system. This allows stopping the fluidization for short periods in three different areas, inlet, centre and outlet.

3.2 Applications of scaling laws

The scaling of the cold flow model is based on the principles of Glicksman described in Chapter 2.2.4. Complete matching of the full set of dimensionless numbers (Table 2.5) would cause a geometrical scaling of 1:4.68 in FR and 1:4.9 in AR. This scaling would lead to high air flow rates and dimensions which are not suitable for the laboratory at the Vienna University of Technology. Therefore the scaling was reduced to 1:10. Moreover the criteria for the simplified set are satisfied. Therefore the simplified set of dimensionless numbers (equation (2.37)) is used for a scaling of 1:10.

Table 3.2 shows the relevant scaling parameters and the corresponding dimensionless numbers for the fuel reactor. The gas properties belong to air at ambient pressure and ambient temperature and the particle properties to bronze particles with a mean effective diameter of 50 µm.

Table 3.2: Fuel reactor scaling properties

			Perfect match					
	Unit	**FR hot**	Full set		Simplified set, 1:10		**Scale 1:10**	
$\boldsymbol{U_s}$	$\frac{m}{s}$	5.65	2.61		1.78		2.19	
$\boldsymbol{d_p}$	μm	200	42.69		35.31		50	
$\boldsymbol{\rho_p}$	$\frac{kg}{m^3}$	3425	14994		14994		8900	
$\boldsymbol{\rho_g}$	$\frac{kg}{m^3}$	0.27	1.18		1.18		1.18	
$\boldsymbol{\mu_g}$	$Pa \cdot s$	4.6E-05	1.8E-05		1.82E-05		1.82E-05	
Dimensionless numbers			abs.	rel. ($^{hot}/_{cold}$)	abs.	rel. ($^{hot}/_{cold}$)	abs.	rel. ($^{hot}/_{cold}$)
$\boldsymbol{Fr_P}$	-	1.64E+04	1.64E+04	1	Fr_D= 3.61	1	Fr_D= 5.44	0.66
$\frac{\boldsymbol{\rho_p}}{\boldsymbol{\rho_g}}$	-	1.26E+04	1.26E+04	1	1.26E+04	1	7495	1.68
$\boldsymbol{Re_D}$	-	7.35	7.35	1	4.16	1.76	7.35	1
$\frac{\boldsymbol{U_s}}{\boldsymbol{U_{mf}}}$	-	233.5	233.5	1	233.5	1	233.5	1
$\frac{\boldsymbol{D}}{\boldsymbol{d_p}}$	-	4500	4500	1	2548	1.76	1771	2.54
$\boldsymbol{\phi_s}$	-	0.9	0.9	1	0.95	0.95	0.95	0.95
$\frac{\boldsymbol{Gs}}{\boldsymbol{\rho_p \cdot U_s}}$	-			0.49		0.73		0.99
Scale	-	1:1	1:4.68		1:10		1:10	
Gas volume flow rate	$\frac{m^3}{h}$	12.932	272		41		50	

The reason for not using the perfect matched simplified set of scaling laws for a scale of 1:10 is that the flow pattern in the cold flow model wouldn't be the same as in the hot plant. Therefore the parameters have been adjusted to fit the flow pattern. As shown in Figure 3.6 the perfectly matched simplified set of scaling laws is located in the high velocity bubbling fluidized bed regime instead of the turbulent fluidized bed regime.

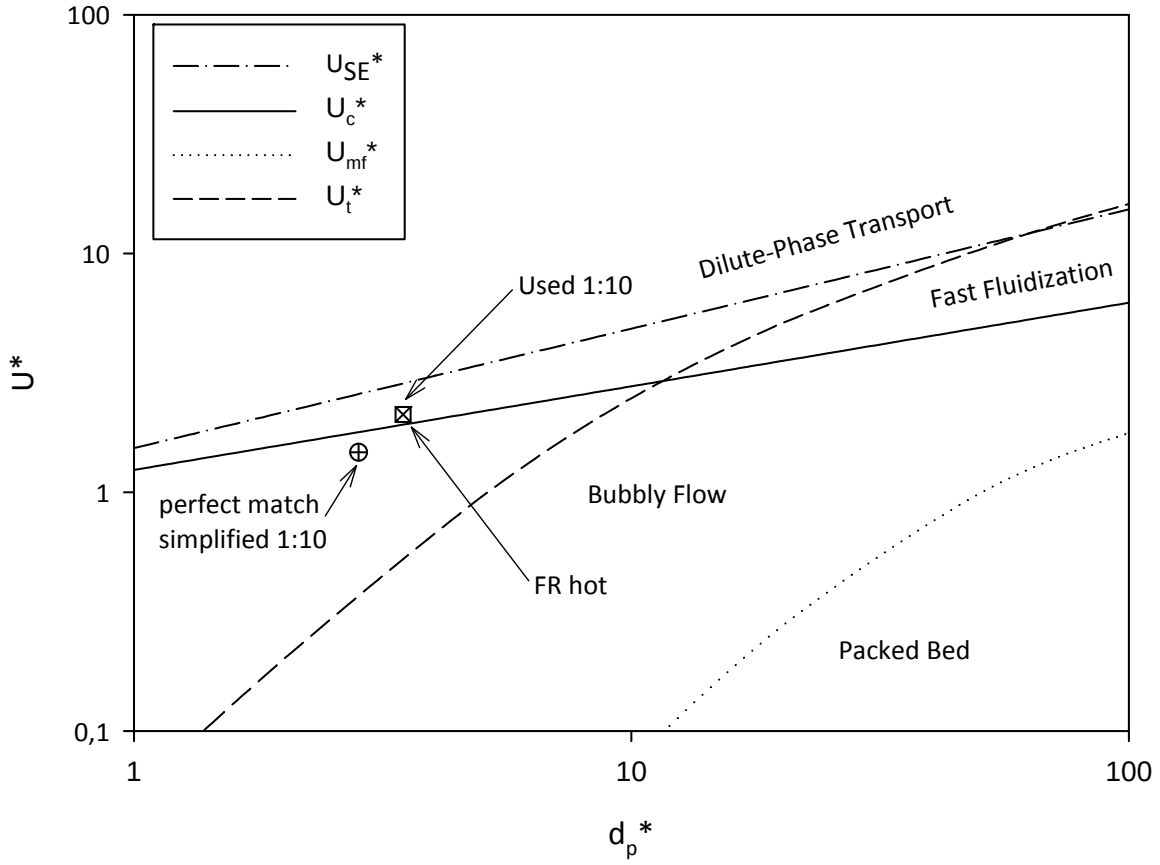

Figure 3.6: Flow regime map for FR scaling

The same procedure is used for the air reactor scaling. Table 3.3 shows the properties of the used materials and the calculated dimensionless numbers.

Table 3.3: Air reactor scaling properties

			Perfect match					
	Unit	**AR hot**	Full set		Simplified set, 1:10		**Scale 1:10**	
$\boldsymbol{U_s}$	$\frac{m}{s}$	7.67	2.43		2.43		3.23	
$\boldsymbol{d_p}$	μm	200	40.54		33.98		50	
$\boldsymbol{\rho_p}$	$\frac{kg}{m^3}$	3425	14670		14670		8900	
$\boldsymbol{\rho_g}$	$\frac{kg}{m^3}$	0.28	1.18		1.18		1.18	
$\boldsymbol{\mu_g}$	$Pa \cdot s$	4.6E-05	1.8E-05		1.8E-05		1.8E-05	
Dimensionless numbers			abs.	rel. ($^{hot}/_{cold}$)	abs.	rel. ($^{hot}/_{cold}$)	abs.	rel. ($^{hot}/_{cold}$)
$\boldsymbol{Fr_P}$	-	3.0E+04	3.0E+04	1	$Fr_D = 5$	1	$Fr_D = 8.9$	0.56
$\frac{\boldsymbol{\rho_p}}{\boldsymbol{\rho_g}}$	-	1.24E+04	1.24E+04	1	1.24E+04	1	7.5E+03	1.65
$\boldsymbol{Re_D}$	-	9.25	9.25	1	5.45	1.7	10.75	0.86
$\frac{\boldsymbol{U_s}}{\boldsymbol{U_{mf}}}$	-	350.5	350.5	1	350.5	1	350.5	1
$\frac{\boldsymbol{D}}{\boldsymbol{d_p}}$	-	6000	6000	1	3531	1.7	2382	2.5
$\boldsymbol{\phi_s}$	-	0.9	0.9	1	0.95	0.95	0.95	0.95
$\frac{\boldsymbol{Gs}}{\boldsymbol{\rho_p \cdot U_s}}$				0.74		0.74		0.9
Scale	-	1:1	1:4.9		1:10		1:10	
Gas volume flow rate	$\frac{m^3}{h}$	39785	736		126		170	

Analogously to the FR scaling the AR scaling with the perfectly matched simplified set leads to a shift in the flow regime. As Figure 3.7 shows, the perfectly matched simplified set would drift into the fast fluidization region. To prevent of this the properties were changed to fit the flow pattern.

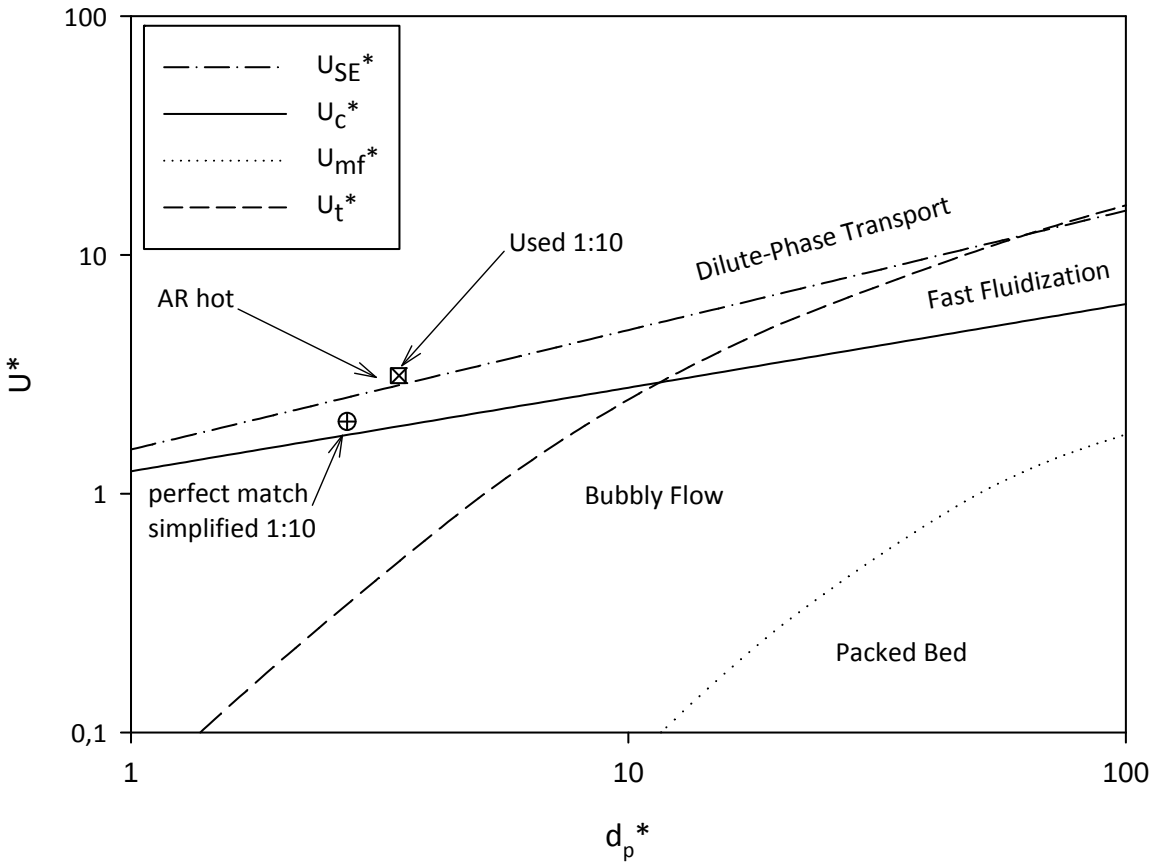

Figure 3.7: Flow regime map for AR scaling

3.3 CFM particle characterization

The bed material used for cold flow model testing was procured from by ECKA granules and is made of bronze with a particle distribution between 45-63 µm (ECKA Zinnbronze 89/11 kugelig AK 0,045-0,063 mm). The particle size distribution is determined using three different methods: sieving, microscope and by laser diffraction.

3.3.1 Particle sieve analysis

Sieve analysis is a widespread and simple analysis method to determine particle size distribution. To separate the different particle classes sieves with different mesh openings are used. The applicability of the method is limited by particle size. To analyze particles smaller than 100 µm air jet sieves have to be used because the particles tend to agglomerate causing measurement errors. For this reason an air jet sieve from ALPINE (LS-N/AC) operating with HAVER & BOECKER DIN ISO 3310-1 sieves is used. Figure 3.8 shows the principle of the air jet sieve. Below the sieve a vacuum is generated causing that particles smaller than mesh size are sucked through the mesh. Additionally a rotating arm distributes fresh air from below the sieve and provides a mixing of the solids and causes agglomerates to break. As the fraction smaller than sieve diameter is lost in an air jet sieve, the analysis has to start with the smallest mesh opening. After a fixed time of sieving the weight loss of the sieved material is determined and the remaining solids are transferred to the next sieve. Using particle sieve analysis the mass distribution of a bulk of solids can be determined.

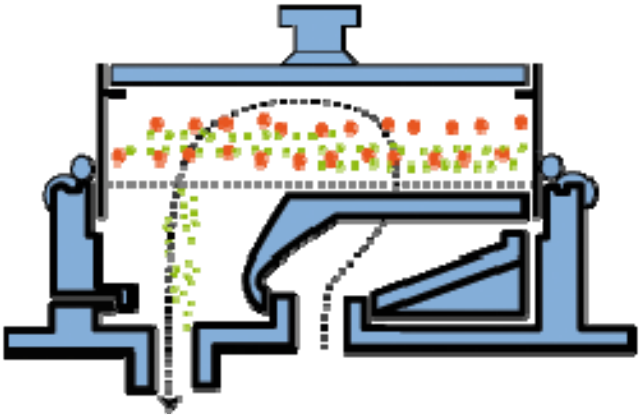

Figure 3.8: Basic principle of air jet sieving (www.labopolis.com)

3.3.2 Particle size analysis by microscopy

The particle size distribution analysis with a microscope is based on a graphical analysis of a picture, taken by a microscope (OLYMPUS BX61 and OLYMPUS BX-UCB). Figure 3.9 a) shows such an image, but this picture is not useful for an analysis because many particles touch each other causing an overestimation of the particle size. In this case the graphic analysis program is not able to separate these particles, which would cause high particle sizes or exclude these particles. Therefore it is important to distribute the particles well.

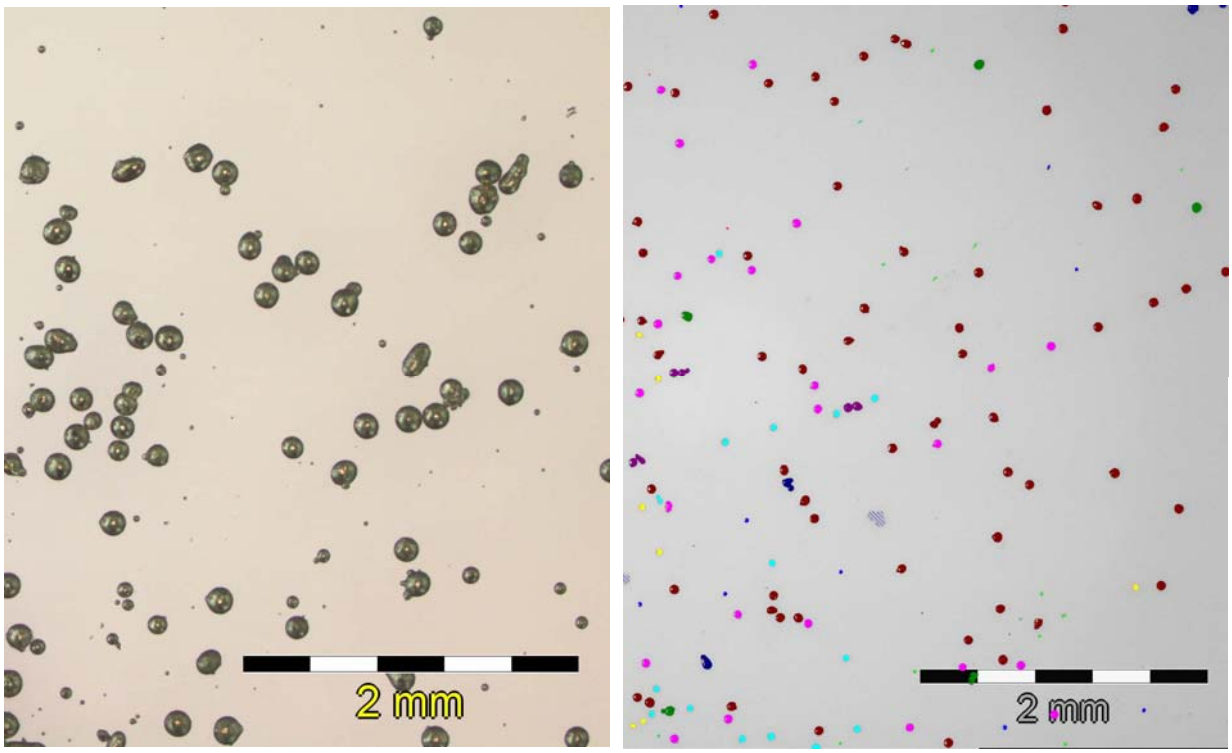

a) b)

Figure 3.9: a) Microscope picture of the bed material
b) Picture after graphical processing indicating different particle size classes in different colors

As depicted in Figure 3.9 b), the graphical processing software classifies the particles marking them by different colors. Then these colored particles are counted. To avoid counting of agglomerated particles the maximum particle size can be limited manually. Compared with the sieve analysis, which delivers a mass distribution, this optical method provides a counted diameter distribution and allows for determination of the particle sphericity.

3.3.3 Particle analysis using Mastersizer 2000

The Mastersizer 2000 from Malvern analyses the particle size distribution with the low angel laser light scattering (LALLS) method. This method uses the principle that particles passing a laser light ray scatter the light beam. In this case the scattering angle and the intensity of the scattered laser light depend on particle size and particle quantity. Figure 3.10 shows a schematic layout of LALLS size distribution analyzer. Basically the Mastersizer 2000 consists of a laser light source, a sample cell, different lenses, several detectors and a data handling system.

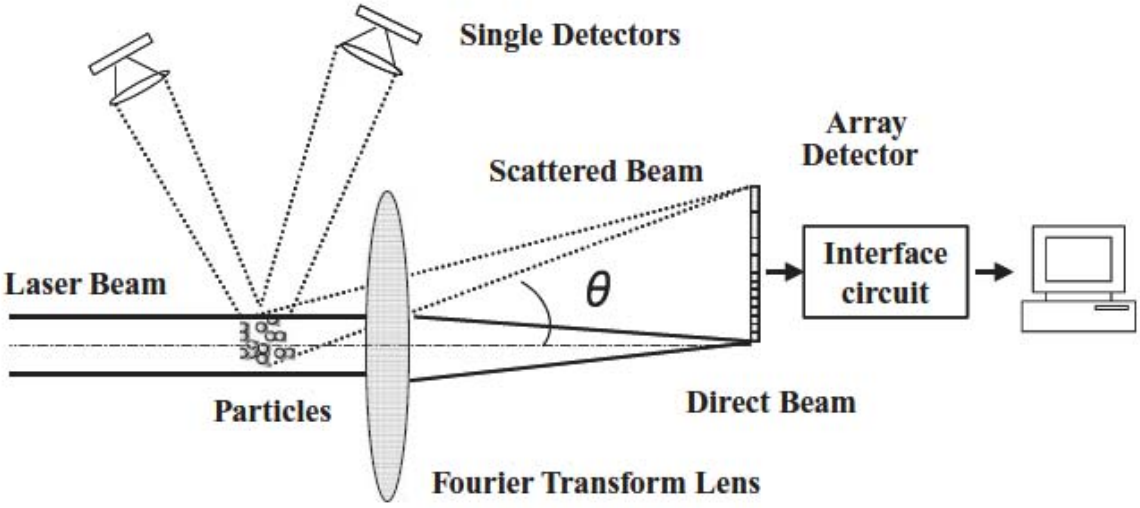

Figure 3.10: Schematic layout of LALLS size distribution analyzer [54**]**

To interpret the diffraction pattern several approximations are used. The Mastersizer 2000 is able to use Fraunhofer Approximation or Mie Theory, which is necessarily used for accurate results for particles smaller than 50 µm.

To obtain representative results the particles have to be distributed evenly in the sample cell. For this purpose the Hydro2000S dispersing module is used. In this module the particles are dispersed in water by a mixer and an ultrasonic vibrator is used for agglomeration break-up and a well suspending.

3.3.4 Bulk density

Bulk density is an important parameter for the used solids flow rate measurement method. It is determined by weighing the volume of a bulk of particles. Therefore a vessel of defined volume is used where the bulk of particles is introduced. To calculate the exact volume of the vessel it is filled with water and temperature and mass are measured. According to equation (2.12) the bulk density can be calculated from the bed material mass and the vessels volume.

3.4 Measurement system

The cold flow measurement equipment includes the determination of pressures and volume flow rates. In addition the discharge of solids from the cyclone and the solids circulation rate are determined.

3.4.1 Pressure measurement

For the pressure measurement small holes with a diameter of 1 mm are drilled into the cold flow model wall. On top of these holes an adapter with a 1/8” internal screw thread is attached. To prevent bed material from flowing out of the reactor, these adapters are filled with cotton wool. To connect the adapter with the pressure transmitter (Kalinsky DS2-240), flexible tubes with an internal diameter of 4 mm and a suitable male end fitting is used. The flexible tubes are bundled in two 32 port multi plugs allowing for flexible use of the pressure measuring equipment. Figure 3.11 shows the used pressure measurement ports and their position on the cold flow model.

For pressure measurement ports CAR 1 and CFR 1 pressure transmitters (Epcos AUR 0.100 F C4 TN H S2.0) are directly attached instead of using a hose as described above. This allows for a faster reaction on pressure alternations.

“Kalinsky DS2-240” and “Epcos AUR 0.100 F C4 TN H S2.0” pressure transmitters work with a supply voltage of 10-30 V and a current output of 4-20 mA, which is proportional to pressure. As the measurement card only allows the recording of voltages, the voltage over a 250 Ω electric shunt is measured causing a voltage drop of 1-5V. To record the data two National Instruments data acquire cards of the type “NI PCIe-6323” are used.

An overview of the used multiplug ports and the used data acquriing ports are given in Table 10.1 in the Apendix on page I.

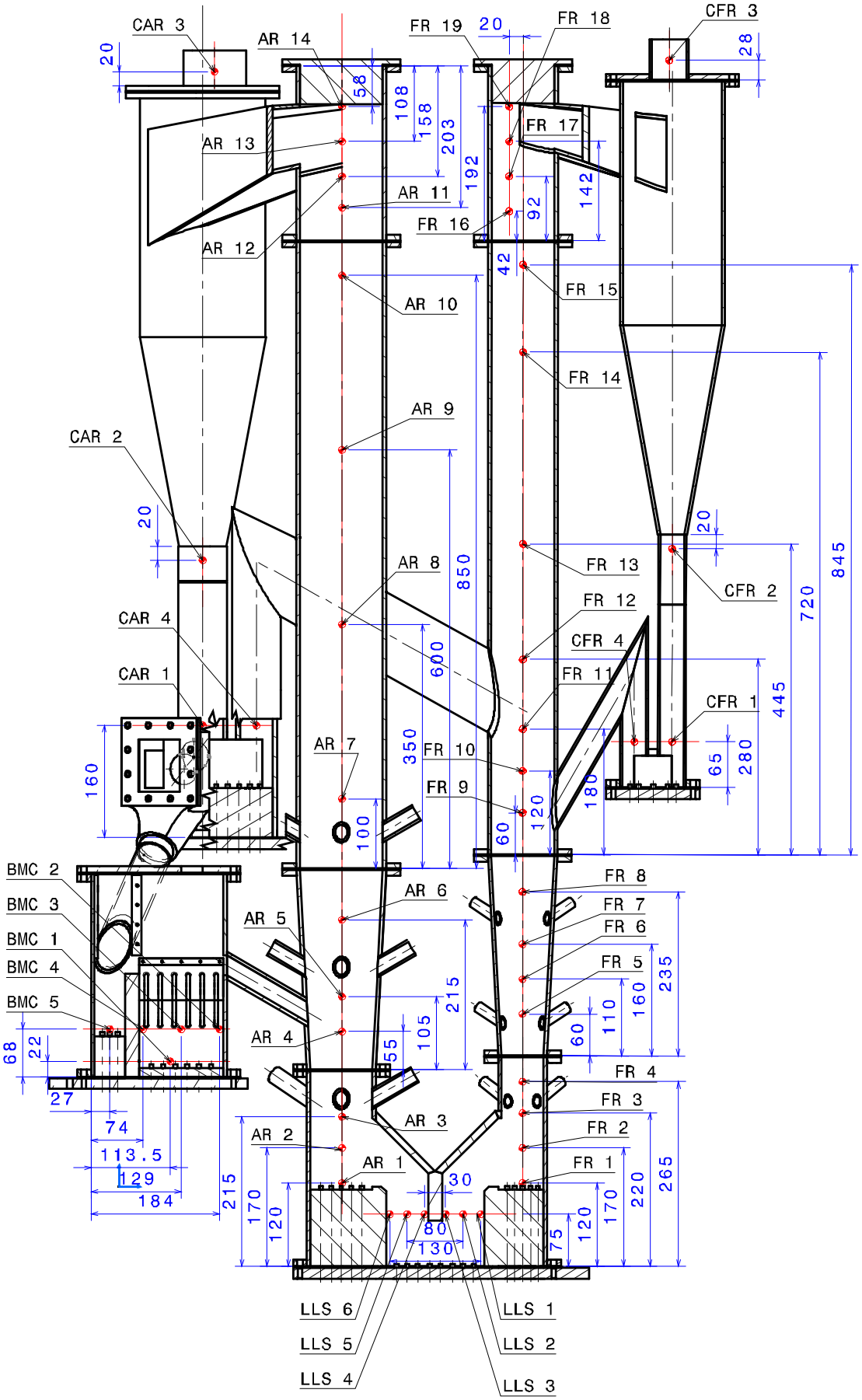

Figure 3.11: Pressure measurement nozzles with name and position on the cold flow model

3.4.2 Volumetric flow rate

To measure and adjust the air flow rates variable area flow meters are used. This method is based on the drag forces of a shaped weight in a diverging tube. The elevation of the weight depends on the flow rate of the gas in the tube.

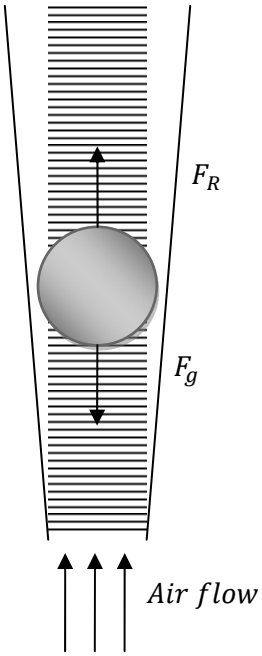

The weight starts floating as soon as drag force and weight force are equal. Since the drag coefficient depends on the gas properties, such as density and viscosity, these variable area flow meters have to be calibrated for a certain temperature, pressure and type of gas. The data of this calibration is given in Table 3.5.

Table 3.4: Specified conditions for the used variable area flow meters

Parameter	Value	Dimension
T_0	20°C	°C
p_0	8	bar
ρ_0	1.293	kg/Nm³
μ_0	0.018326	mPa s

The variable area flow meters used are produced by KROHNE and are of type VA40 and DK48 depending on the flow rate of the gas. A summary of measurement rages is given in Table 3.5.

Table 3.5: Variable area flow meters used in the cold flow model

	Operating range	Dimension
AR bottom	1.5-15	Nm³/h
AR 1	21-200	Nm³/h
AR 2	21-200	Nm³/h
AR 3	21-200	Nm³/h
FR bottom 1	1.5-15	Nm³/h
FR bottom 2	0.47-4.3	Nm³/h
FR 1	6-60	Nm³/h
FR 2	6-60	Nm³/h
FR 3	6-60	Nm³/h
cone	5. 4-50	Nl/h
BMC	0.42-4	Nm³/h
BMC settling camber	0.28-2.5	Nm³/h
ULS inlet	190-1600	Nl/h
ULS center	190-1600	Nl/h
ULS outlet	190-1600	Nl/h
LLS Inlet	280-2300	Nl/h
LLS center	190-1600	Nl/h
LLS outlet	280-2300	Nl/h
ILS inlet	87-610	Nl/h
ILS center	62-430	Nl/h
ILS outlet	87-610	Nl/h

3.4.3 Cyclone discharge measurement

The discharge of solids from the cyclone is determined by weighting of the solids collected in the dust filters. These dust filters (MANN+HUMMEL Europiclon®) are a combination of a cyclone and a paper-filter. The solids elutriation of the cyclone is measured by shaking the dust filters and weighing of the dust filters solids collection chamber. The solids discharge rate is determined after equation (3.2).

$$\dot{m}_{discharge} = \frac{m_{discharge}}{\Delta t} \quad \textbf{(3.2)}$$

3.4.4 Mass flow measurement

The solids flow rate in the AR and FR riser is measured by stopping the fluidization in the appropriate loop seal (upper or internal loop seal) and by determining the solids accumulation in the appropriate loop seal downcomer. Equation (3.3) is used to calculate the corresponding solids flux.

$$G_{S_i} = \frac{A_{down\ comer\ i} \cdot \Delta H \cdot \rho_{bulk}}{\Delta t \cdot A_{riser\ i}} \quad \textbf{(3.3)}$$

Table 3.6 gives the relevant cross sections for the calculation of the solids flux.

Table 3.6: Cross sections for solids flow calculation

Reactor	$A_{down\ comer}$ m²	A_{riser} m²
AR	2,83E-3	1,44E-2
FR	9,08E-4	6,36E-3

To obtain representative values for the solids flow rate the measurement height should be 60 mm with a minimum of 5 total sample-times taken. In some conditions, i.e. very high solids circulation rates, 60 mm of solids accumulation is no longer measurable; then the height has to be reduced to 50 or even 40 mm.

3.4.5 Data-acquisition system

The data acquisition system is built up in National Instrument LabView, which is a graphical coding language. It is optimized for scientific use and contains several features for data acquisition and storage.

The data acquisition system meets the following requirements:

- Acquisition of the pressure sample data.
- Storage of all relevant values into a text (.txt) file with an adjustable writing interval.
- Visualization of pressure history and pressure profile with a variable sample size for the calculation of average values.
- Possibility to include comments.
- Input fields for fluidization rates.
- Integration of an automatic control for the input pressure controller.
- Control options for the multi phase motor.
- Control output for magnetic valves and a pneumatic slider.

The data acquisition card, which is built into a computer, is adjusted to deliver a sample every 25 ms. These samples are stored in global variables making it easier to have an overview on the program and to use variables several times.

To store the recorded data the program builds a new file every hour and creates a specified header. This file is filled with pressure data, fluidization rates, stepping motor position and time. The storage timing is user-adjustable by a numeric input variable on the “Control” front-panel. It is also possible to deactivate data storage in the “Control” panel and to define the save path of the file and to set a comment.

On the “Control” panel there are also switches for the magnetic valves, the BMC slider and the input pressure control. The input pressure can be set by a numeric input and the actual pressure and the actual controller value are shown on the “Control” panel. The maximum controller value which is transmitted to the pressure controller is set to 8.5 V corresponding to a pressure value of 8.5 barg. To release the pressure smoothly when the program is stopped a procedure is integrated regulating the pressure to atmospheric conditions slowly.

The motor control panel contains the settings for the multi phase motor. One can define the moving distance~~,~~ and possible position errors are shown. If the program gets stopped the piston moves back to the default position where the vent is closed.

In the pressure profile panel the pressure profiles of the air and fuel reactor risers and downcomers are shown. One can also adjust the sample size in order to determine average values via a numeric input field. The pressure history panel shows the pressure history of all pressure transmitters, which can be averaged by the numeric input called “Average”. To register the fluidization rates the panel “Fluidization” provides numeric inputs which are stored in the record file. The last panel “Input” contains the heights of the pressure transmitting nozzles. These heights are needed to visualize the pressure profiles.

3.5 Measurement techniques and procedures

3.5.1 Design fluidization rates

To reach the required gas velocities in the reactors and loop seals the needed gas streams were calculated. These calculated design fluidization rates are summed up in Table 3.7.

Table 3.7: Calculated design fluidization rates

	Value	Unit
AR bottom	9	Nm^3/h
AR prim.	85	Nm^3/h
AR sec.	35	Nm^3/h
AR tert.	35	Nm^3/h
FR bottom 1	0	Nm^3/h
FR bottom 2	3	Nm^3/h
FR prim.	13	Nm^3/h
FR exp 1	16	Nm^3/h
FR exp 2	16	Nm^3/h
Cone	35	Nl/h
BMC	2,8	Nm^3/h
BMC settling	1,6	Nm^3/h
ULS in	750	Nl/h
ULS cn	500	Nl/h
ULS out	750	Nl/h
LLS in	1100	Nl/h
LLS cn	400	Nl/h
LLS out	1100	Nl/h
ILS in	240	Nl/h
ILS cn	240	Nl/h
ILS out	240	Nl/h

These calculated fluidization rates serve as base points for the cyclone discharge and the loop seal operation optimization.

3.5.2 Cyclone particle discharge optimization

A cyclone is a device where gas and solids are separated utilizing centripetal forces. Such cyclones are characterized by the particle cut-off diameter and the solids deposition rate. While the cut-off particle diameter indicates the border of the particle diameter where solids are separated in the cyclone or elutriated with the gas stream, the solids deposition rate is the sum of solids (all particle diameters) elutriated with gas. Optimization of cyclone performance can mean adjusting the cut-off diameter with respect to the process or minimization of solids deposition rate. In circulating fluidized bed applications the cyclone solids elutriation is crucial to keep the solids inventory stable for long term operation. Especially in chemical looping the solids inventory is a critical value since the process performance, such as combustion efficiency, is strongly related to solids inventory.

The main parameters influencing the solids discharge are

- cyclone inlet flow pattern,
- gas and solids flow in the conical and converging part of the cyclone, and the
- flow pattern at the cyclone outlet.

In the selected design the position of the vortex finder is eccentric with the position of the eccentricity and the depth of the vortex finder being adjustable. Figure 3.12 shows the geometries of the cyclone and the vortex tube. To investigate the influence of the outlet position the lid with the eccentric gas outlet was rotated, where angle α is the parameter which is varied.

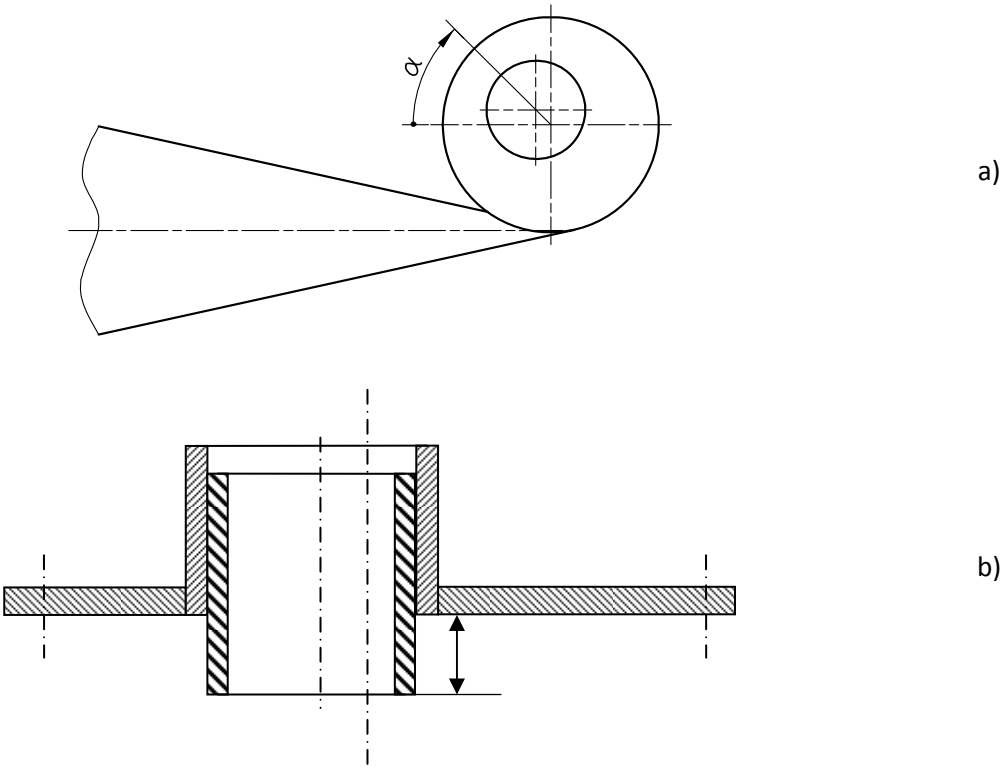

Figure 3.12: a) Geometry of the cyclone b) Geometry of the vortex tube

To observe the influence of a vortex tube depth an adjustable pipe is installed. The depth of the vortex tube is measured as shown in Figure 3.12 b) and is varied between 0–15 mm.

3.5.2.1 Air reactor cyclone

To quantify the solids discharge of the cyclones the model is in operation for 15 min and afterwards the solids collected in the filter cyclone combinations are weighed. To determine the effect of the outlet position the lid is rotated. The influence of the solids flow rate and the air speed is determined by variation the fluidization in the AR from 99 Nm^3/h to 164 Nm^3/h. The effect of the vortex tube depth was investigated at the AR, only for the positions 0 and 15 mm.

The distribution of fluidization air is shown in Table 3.8; 164 Nm³/h is the design fluidization of the AR. The FR was only fluidized at the bottom to prevent the fluidization valves from blocking and to retain the global solids flow. The LLS and the ULS was fluidized under design conditions and the BMC was deactivated.

Table 3.8: Fluidization for AR discharge measurements

	AR bottom Nm³/h	AR prim. Nm³/h	AR sec. Nm³/h	AR tert. Nm³/h	FR bottom 2 Nm³/h
AR 99 Nm³/h	9	90	0	0	3
AR 149 Nm³/h	9	90	40	0	3
AR 164 Nm³/h	9	85	35	35	3

3.5.2.2 Fuel reactor cyclone

At the FR cyclone the influence of the discharge and the pressure drop on the vortex tube depth from 0-15 mm was investigated. Therefore the solids entrainment is measured in the filter system over 10 min operation time.

A variation of the solids flow rate was reached by staging the fluidization air in the reactor. The fluidization of the FR for the different experiments can be seen in Table 3.9. AR is only fluidized at the bottom and LLS and ILS are fluidized under design conditions. ULS and BMC are deactivated for these experiments.

Table 3.9: Fluidization for FR discharge experiments

	AR bottom Nm³/h	FR bottom 02 Nm³/h	FR prim. Nm³/h	FR exp. 1 Nm³/h	FR exp. 2 Nm³/h
FR 48 Nm³/h staged	9	3	13	16	16
FR 48 Nm³/h	9	3	45	0	0

For the pressure drop measurements the average of the difference between FR18 and CFR3 was taken and averaged over one minute measurement time.

3.5.3 Optimization of the loop seal operation

To reduce the needed fluidization gas demand and investigate the influence of the loop seals fluidization on the solids circulation system the fluidization of the three fluidization areas in the loop seals are varied. In these experiments two of the three areas are always held at constant conditions and the third is varied. The first loop seal investigated is the LLS because it is expected to mostly influence the fluid-dynamics of the system.

3.5.3.1 Lower loop seal (LLS)

The loop seal optimization is done by varying the air stream in one fluidization area, while the other fluidizations are held constant. In Table 3.10 the constant values and the variation ranges are given. For testing the LLS operation, only the global solids loop is operated.

The AR, ULS and the FR bottom fluidization stages are operated at design conditions given in Table 3.7. To prevent the FR primary fluidization nozzles from blockage the air flow rate in these is set to 6 Nm³/h. The FR expansion fluidization nozzles, the ILS and the BMC are not fluidized.

Table 3.10: Ranges of the fluidization rates considered in the LLS optimization procedure

	Constant	Variation	Unit
LLS in	400	0-2300	Nl/h
LLS cn	200	0-1500	Nl/h
LLS out	400	0-2000	Nl/h

3.5.3.2 Upper loop seal (ULS)

For the ULS operation investigation optimum fluidization conditions in the LLS are taken. The range of fluidization rates are shown in Table 3.11. The AR and the FR bottom fluidization are set to design fluidization (see Table 3.7) and the FR primary fluidization stage is set to 6 Nm³/h to avoid blockage by bed material. The ILS, the rest of the FR and the BMC are fluidized.

Table 3.11: Ranges of the fluidization rates considered in the ULS optimization procedure

	Constant	Variation	Unit
LLS in	700	-	Nl/h
LLS cn	500	-	Nl/h
LLS out	1000	-	Nl/h
ULS in	300	0-1500	Nl/h
ULS cn	200	0-1500	Nl/h
ULS out	300	0-2000	Nl/h

3.5.3.3 Internal loop seal (ILS)

As in the investigations of the other loop seals two of the three fluidization areas are held constant, while the other one is varied. The internal loop seal measurements are done by operating only the internal loop with a slight AR fluidization only and a not fluidized ULS and BMC. The air flow rates for AR bottom and AR primary are 3 Nm³/h and 1 Nm³/h to avoid blockage of the fluidization nozzles. The FR bottom was fluidized with 3 Nm³/h and the FR primary with 45 Nm³/h. Table 3.12 shows the variation range of fluidization air and the constant air rates.

Table 3.12: Ranges of the fluidization rates considered in ILS optimization procedure

	Constant	Variation	Unit
LLS in	700	-	Nl/h
LLS cn	500	-	Nl/h
LLS out	1000	-	Nl/h
ILS in	100	100-500	Nl/h
ILS cn	100	100-400	Nl/h
ILS out	100	100-600	Nl/h

3.5.4 Linear sensitivity analysis

To study the influence of deviations from the design conditions a linear sensitivity analysis is carried out with the solids flow rates in the AR and FR riser being in focus of the investigation. The theoretical background of the linear sensitivity analysis is given in Chapter 2.2.6. This analysis allows for a better understanding of the reaction of the system on varied parameters which can be used for solids flow regulation.

The varied parameters are shown in Table 3.13. The exactly calculated values are rounded to fit the scale of the variable area flow meters.

Table 3.13: Variations for linear sensitivity analysis in Nm³/h

	+20% Nl/h	+10% Nl/h	Design Nl/h	-10% Nl/h	-20% Nl/h
AR bottom	11	10	9	8	7
AR prim.	105	95	85	75	65
AR sec.	45	40	35	30	25
AR tert.	45	40	35	30	25
FR bottom	3.6	3.3	3	2.7	2.4
FR prim	16	14	13	12	10
FR exp 1	20	18	16	18	20
FR exp 2	20	18	16	18	20

The variation of the FR expansion nozzles (FR exp 1 and 2) describes the influence of the reaction rate. As said before these air streams simulate the expansion of the fuel according to equation (3.1). So a higher stream in FR expansion 2 simulates a slower reaction in the FR, because the expansion is on a higher reactor level.

3.5.5 Influence of global solids inventory

In the operation of a fluidized bed solids inventory is a key parameter. While in bubbling fluidized beds the bed height is related to the inventory, in circulating fluidized beds the inventory has a multitude of effects. It influences the solids distribution in the riser and has a strong effect on the solids entrainment rate. Furthermore if the inventory is selected inappropriately, it can cause server malfunction in CFB operation by causing choking. Therefore the effect of the global bed inventory is investigated. Based on the design conditions, where a global inventory of 35 kg has been calculated, the effect of ±5 kg global bed inventory is investigated. These experiments are carried out with the ascertained loop seal fluidizations.

The other fluidizations are set to design conditions as shown in Table 3.7. The solids flow rate is measured as described in Chapter 3.4.4.

3.5.6 Impact of SCV on BMC solids flow rate

The measurements of the influence of the SCV on the DCFB system and the BMC are done as follows:

- Fluidization rates are set to design conditions (see Table 3.7),
- SCV opening range from 0-3.8 mm
- Gs_{FR} measurement as described in chapter 3.4.4,
- Gs_{AR} measurement with briefly closed SCV,
- solids flow rate measurement through the BMC by measuring the time needed to fill a specific volume in the connection pipe between SCV and BCM settling chamber.

The measurement of Gs_{AR} had to be modified, because the solids flow out of the downcomer through the SCV. As depicted in Figure 3.13, the SCV had to be closed to ensure that no bed material flows out of the measurement volume, which would cause too small solids flow rates.

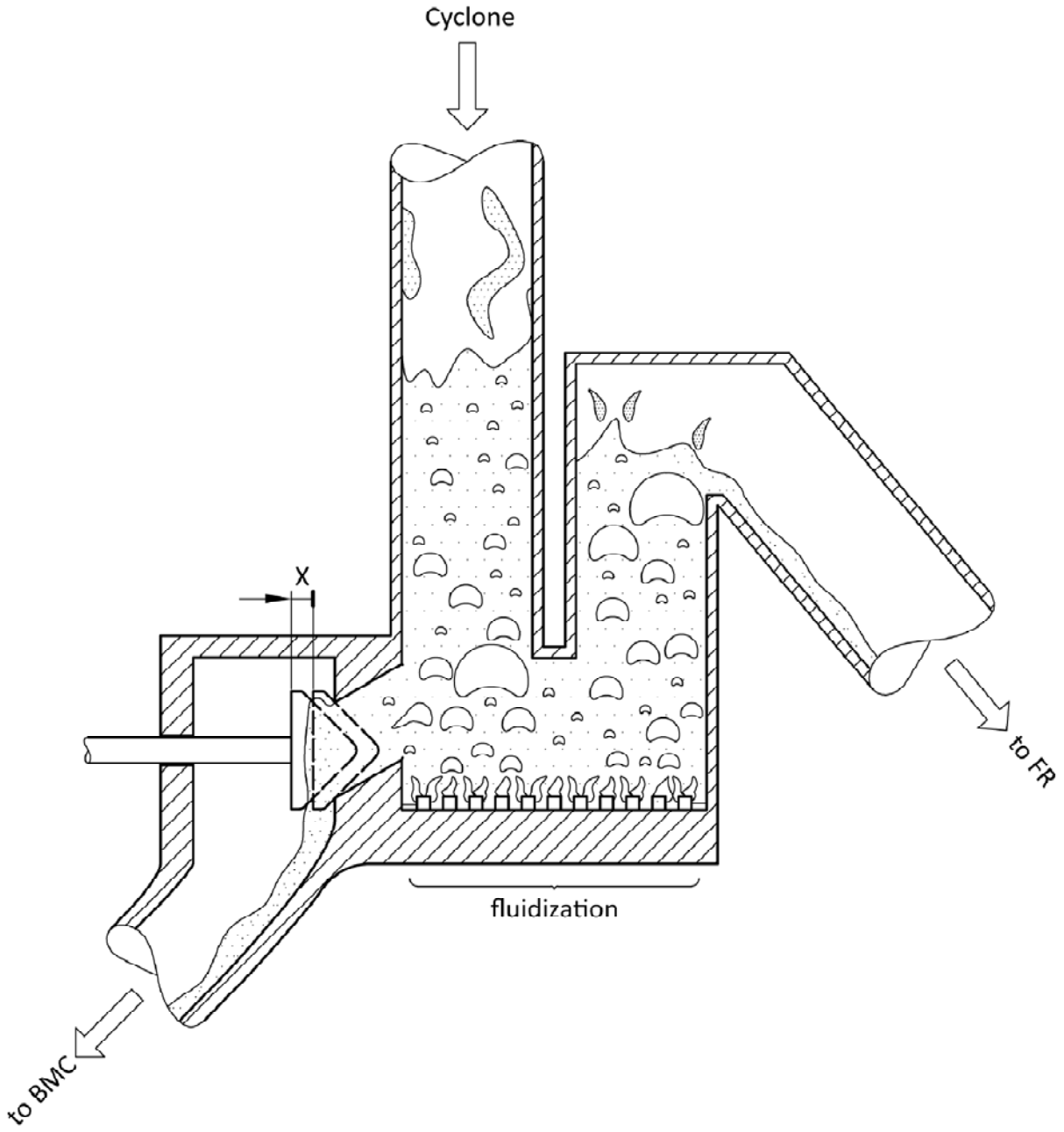

Figure 3.13: Detail sketch of ULS and SCV

The solids flow rate to the BMC is determined by measuring the time of the solids to fill a pre-determined volume. Therefore the solids valve placed at the BMC inlet is closed and the solids accumulation on the pipe to the BMC is observed. Two specific volumes in the connecting shaft between ULS and BMC have been prescribed allowing for measurement of either low or high solids flow rates to the BMC. Equation (3.4) shows the calculation of the mass flow through the BMC.

$$\dot{m}_{BMC} = \frac{V \cdot \rho_B}{\Delta t} \qquad \textbf{(3.4)}$$

To compare this mass flow with the AR solids entrainment flux Gs_{AR} the mass flow ratio γ_{BMC} to the BMC is defined as follows

$$\gamma_{BMC} = \frac{\dot{m}_{BMC}}{G_{s,AR} \cdot A_{AR}} \quad \textbf{(3.5)}$$

3.5.7 Pressure profile at design conditions

The pressure profile of a circulating fluidized bed is a characteristic plot, which contains a lot of information about the solids distribution and the flow pattern. The design fluidization measurement is carried out using the fluidization rates given in Table 3.7 and the optimized loop seal fluidizations (see Table 4.7). The bed material cooler is fluidized and the mass flow ratio through the BMC is 0.32. These parameters were kept constant for 5 min and the measured pressure drops are averaged.

The solids fraction can be calculated from the data of the pressure profile by equation (3.6).

$$\epsilon_S = \frac{V_p}{V_{tot}} = \frac{A \cdot \Delta p \cdot \frac{1}{\rho_p \cdot g}}{A \cdot \Delta z} = \frac{\Delta p}{\Delta z} \cdot \frac{1}{\rho_p \cdot g} \quad \textbf{(3.6)}$$

This parameter gives information about the solids distribution in the reactor system.

4 Results

4.1 Particle characterization

4.1.1 Particle size distribution

The results of the particle size distribution measurements are shown in Figure 4.1. The difference in the mean diameters can be explained by the different measurement methods used. The optical method via microscope delivers a slightly bigger mean diameter than the others because of agglomerated particles which cannot be separated by the software. The average diameter is about 50-65 µm which fits the specification.

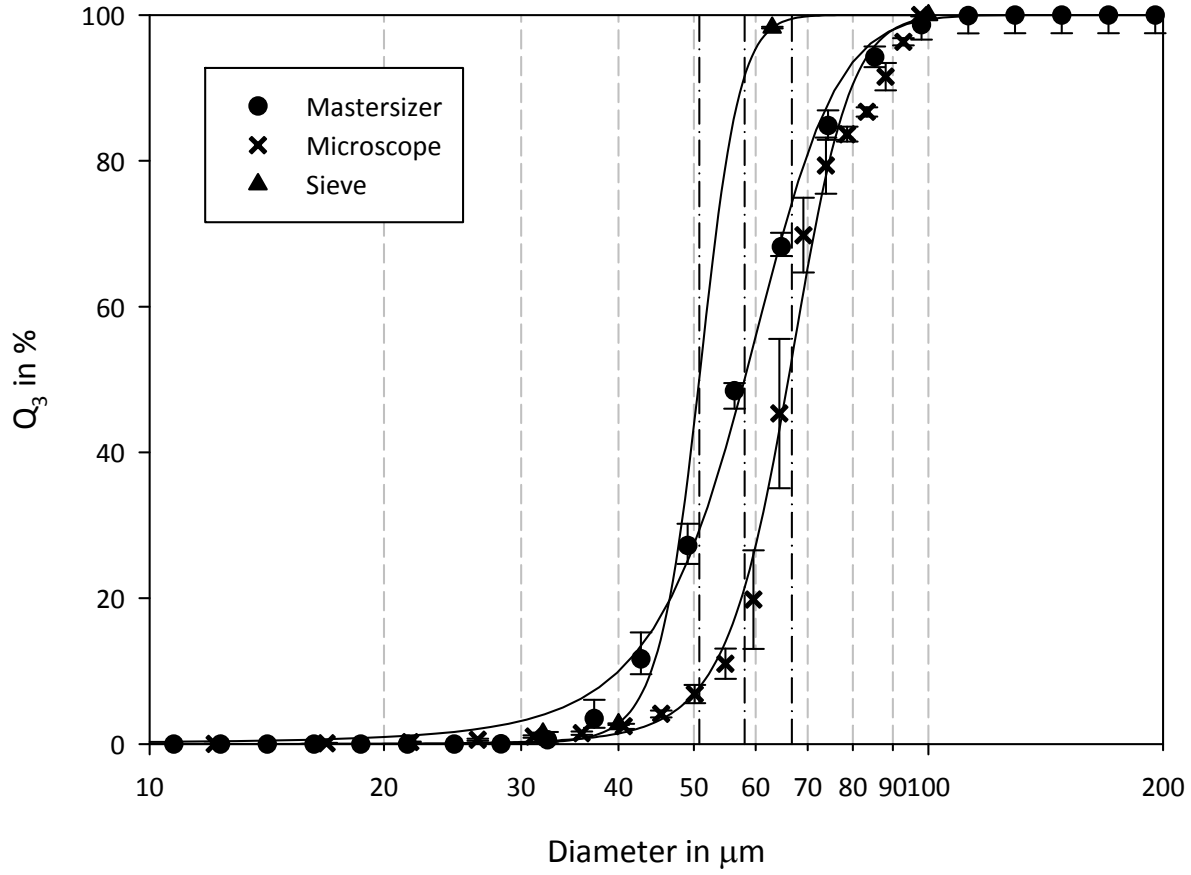

Figure 4.1: Cumulative bed material size distribution depending on measurement method

The median values depending on the measurement method are summed up in Table 4.1. According to equation (4.1) the sauter diameter does not differ much from the volume base diameter when the sphericity is near to one.

$$d_{SV} = \phi_s \cdot d_3 \tag{4.1}$$

Table 4.1: Median Values depending on measurement method

	Sieve	Microscope	Mastersizer
$d_{50,3}$ in µm	51	66	58

4.1.2 Bulk density

To determine the volume of the vessel the mass of water was divided by the density of the water at measurement temperature. To get the bulk density of the bed material the weight of the bronze powder was divided by the volume of the vessel. To adapt the temperature to the values for the density of water found in literature they have to be linearly interpolated between 296.15 and 297.15K.

Table 4.2: Results of bed material bulk density analysis

Nr.	Mass		Temperature water	Density water[55]	Volume	Bulk density
	bronze	water				
	g	g	°C	kg/m³	m³	kg/m³
1	2173	431.5	23.7	997.3	0.000431762	5033
2	2174	429.9	23.7	997.3	0.00043107	5044
3	2175	433.0	23.7	997.3	0.000434209	5009
Average	2174	431.2	23.7	997.3	0.000432347	5029

As shown in Table 4.2 the used bed material has average bulk density of 5029 kg/m³. This leads to a voidage of about 57%.

4.2 Cyclone particle discharge optimization

4.2.1 Air reactor cyclone

The first measurements are done without a vortex finder and over a time period of 15 minutes with design fluidization rates (chapter 3.5.1) and 30 kg inventory. Because of the high discharge and an upmoving strand in the cyclone the first varied parameter was the outlet position. To keep the solids flow rate rather constant the measurement time was reduced to 10 min and the discharged bed material was refilled after every measurement. This variation doesn't affect the discharge as much as needed. Therefore a vortex tube was installed. The variation of the outlet position has been done from 45° to 185°. A complete rotation of the lid was not possible because of the geometric arrangement of the exhaust filters.

Figure 4.2 shows the discharge of the air reactor with respect to the position of the gas outlet without a vortex finder tube emerged into the cyclone body. The experiment was carried out with a global solids inventory of 30 kg and the AR riser fluidized at design conditions. By rotating the outlet from 45° to 5° a reduction of the discharge of about 25% is reached. Anyhow, for stable operation of a circulating fluidized bed these values are far too high causing a loss of the total inventory in 5.8-8.3 hours.

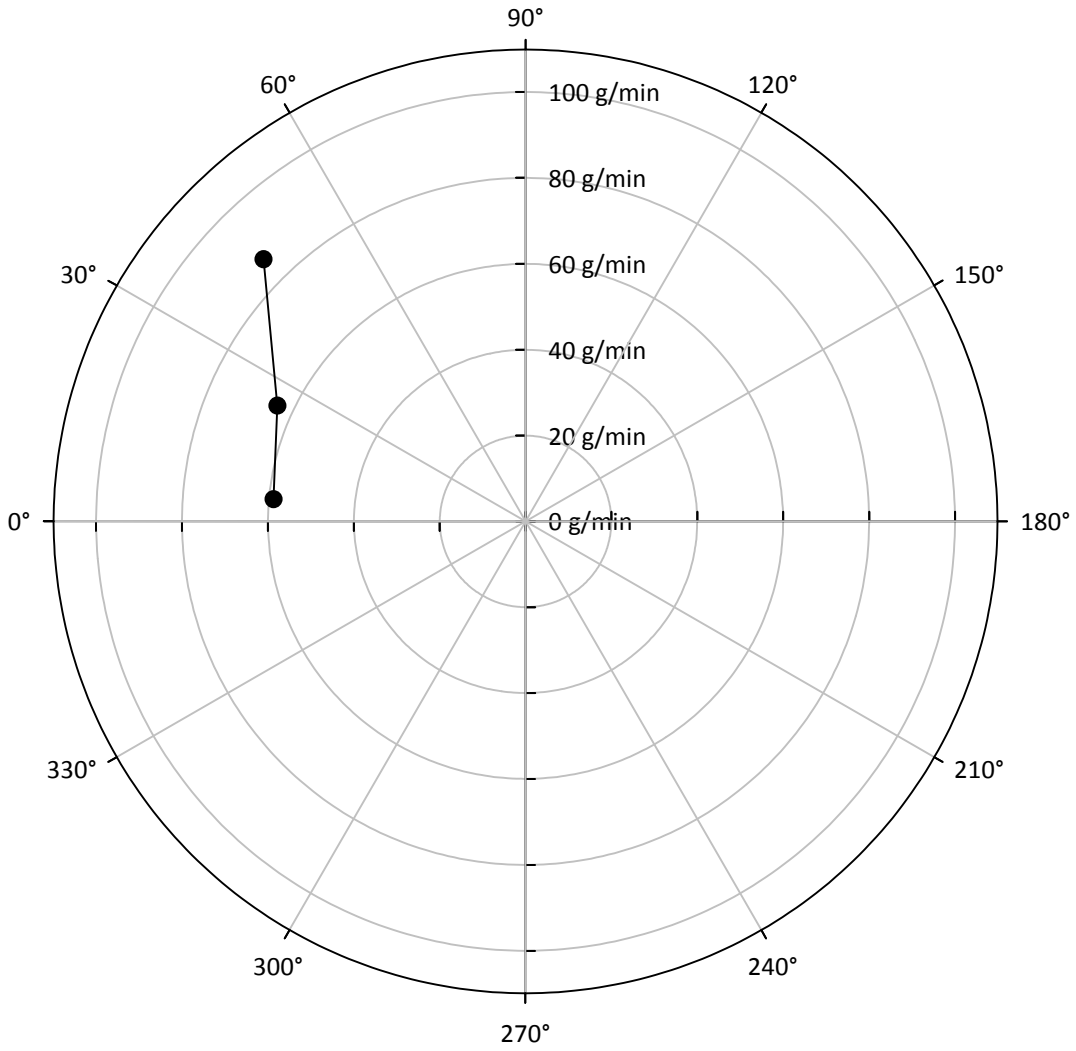

Figure 4.2: Discharge of the air reactor cyclone without vortex finder, 30 kg inventory and 164 Nm³/h

To reduce this solids loss to reasonable values a tube was added to the vortex finder reaching 15mm into the cyclone body(Figure 3.12b). The AR cyclone solids discharge depending on the solids circulation rate (which is related to the solids entrance loading) at a vortex finder length of 15 mm is shown in Figure 4.3. The vortex tube allows a reduction of the discharge from 86.2g/min to 9.92 g/min at an angular position of 45°. Additionally this solids loss can be reduced by changing the position of the vortex tube. By doing so the solids loss is reduced to even below 1.8 g/min. This means that emptying of the system now takes more than 275 hours (considering a solids inventory of 30 kg) which is a reduction by a factor of 47.9 compared to a cyclone without a vortex finder tube. As expected, the discharge decreases with decreasing solids flow rates.

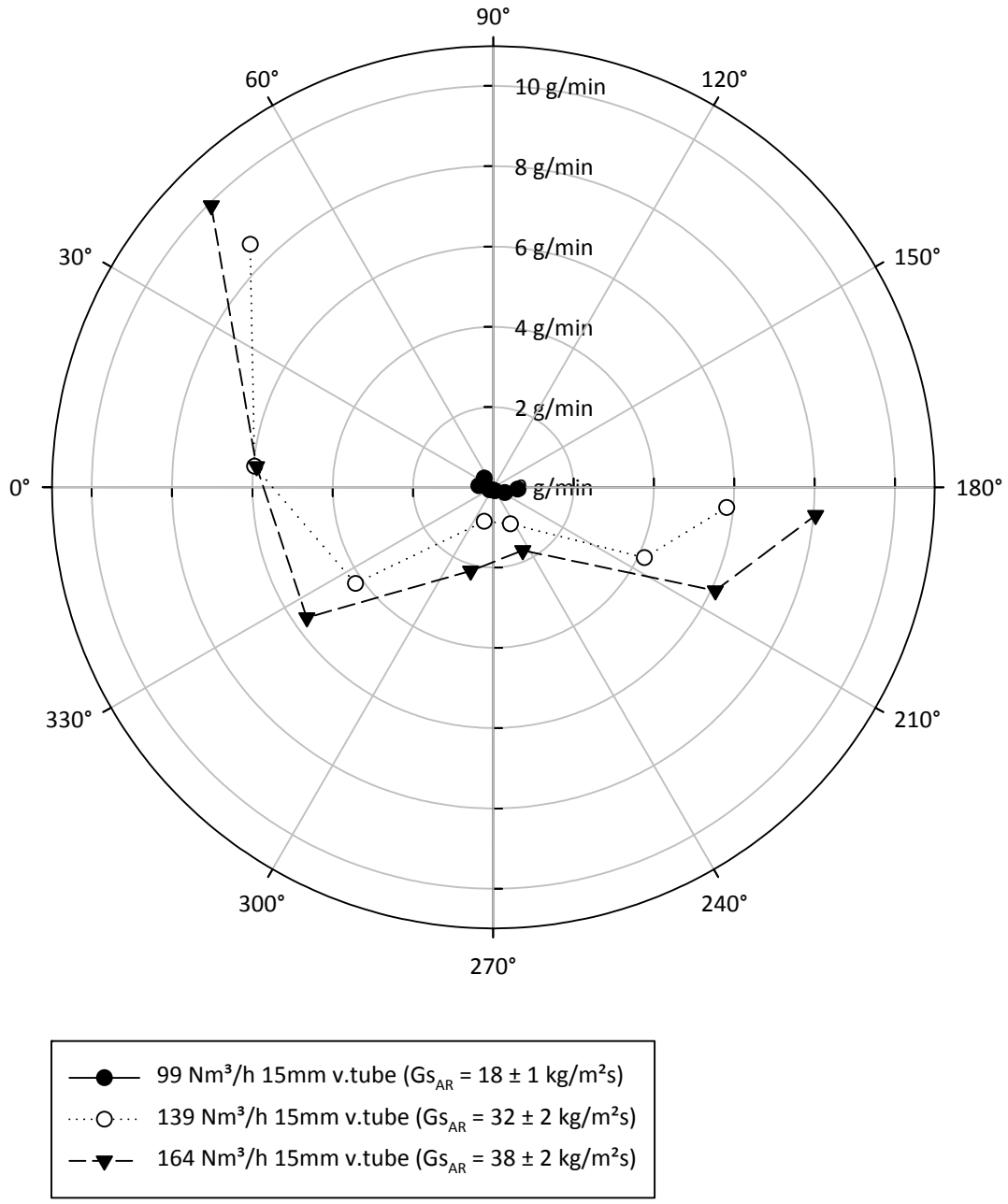

Figure 4.3: Discharge of AR cyclone with a 15 mm vortex tube, 35 kg inventory and varied air distribution (99 Nm³/h with Gs_{AR} = 18 kg/m²s, 139 Nm³/h with Gs_{AR} = 32 kg/m²s, 164 Nm³/h with Gs_{AR} = 38 kg/m²s)

The experiments reveal that the AR cyclone performance is best at a vortex finder outlet position of 285° according to Figure 3.12a. This is in accordance with the optical observation of the motion of solids at the cyclone inlet where part of them are deflected upwards reaching the cyclones top at an angle of approximately 150°.

With respect to these findings the AR cyclone's vortex finder is adjusted to a position at 285° and a length of 15 mm to ensure stable operating conditions. These adjustments are maintained in the following experiments.

4.2.2 Fuel reactor cyclone

Similarly to the AR cyclone a whole rotation of the lid was not possible because of the geometric arrangement. So it is rotated from 45° to 205°. In the design case with no vortex tube and an outlet position of 45° the bed material discharge for design fluidization rates is 4.03 g/min at a solids flow rate of 20.5 kg/m²s referring to the FR riser cross section. Figure 4.4 shows the discharge polar plot for the fuel reactor cyclone. Different solids flow rates and the influence of the vortex tube is depicted. The discharge of the cyclone can be reduced to 55% by changing the outlet position to 5°. As expected, a lower FR solids flux causes lower discharge. The highest impact on the solids entrainment can be reached with a vortex tube. The installation of a 15 mm vortex tube causes a reduction by the factor 10.

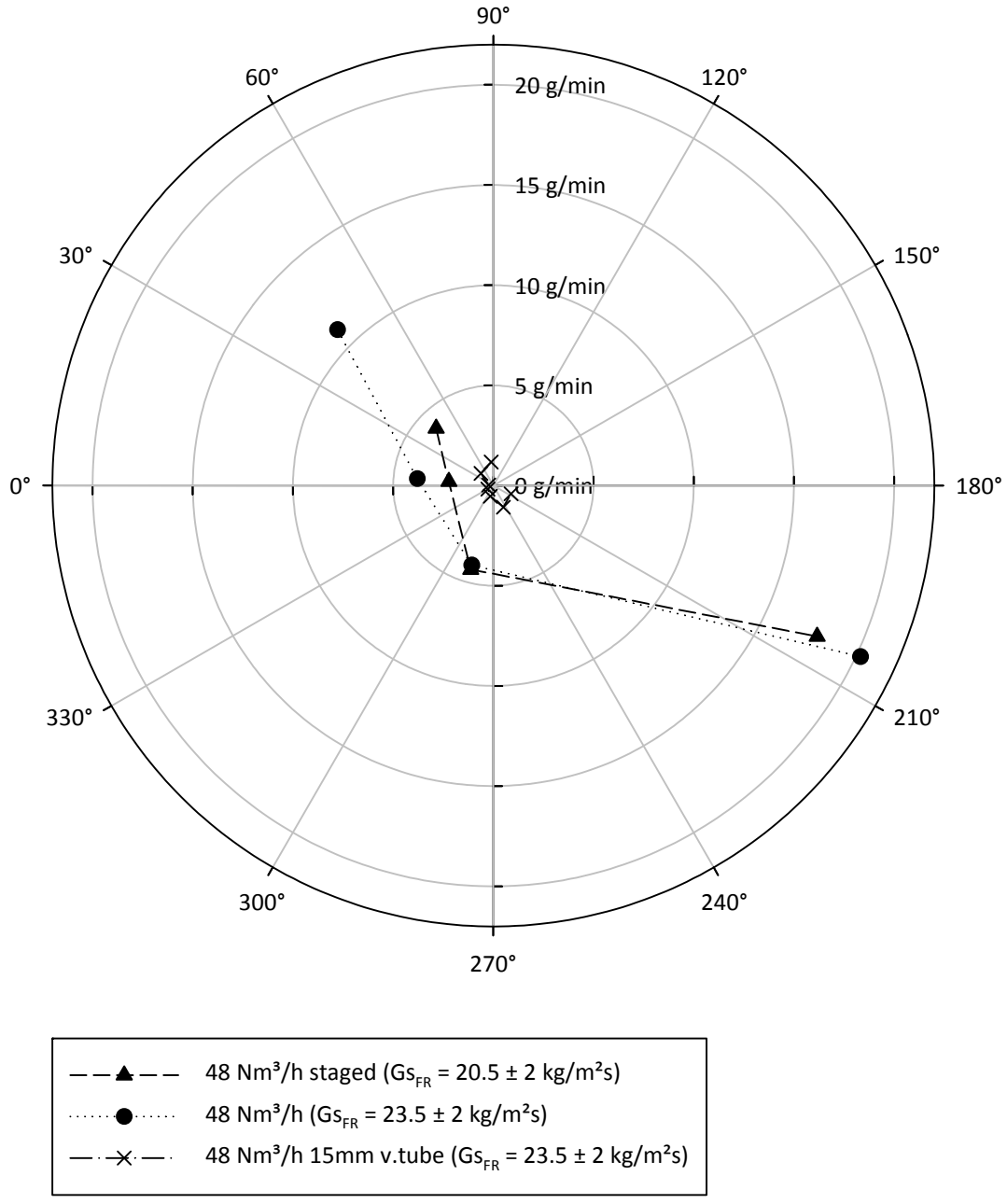

Figure 4.4: Discharge polar plot of the FR cyclone without and with a 15 mm vortex tube, at a solids flux of 20.5 kg/m²s and 23.5 kg/m²s

Figure 4.5 shows the polar plot of the FR cyclone discharge with a solids flux of 23 kg/m²s. The experiments reveal that the FR cyclone performance is best at a vortex finder outlet position of 5°. The discharge at this position is 0.25 g/min, which leads to a reduction of 97.7% based on 11.34 g/min for the high solids flux or an improvement of the cyclone performance by the factor of 45.

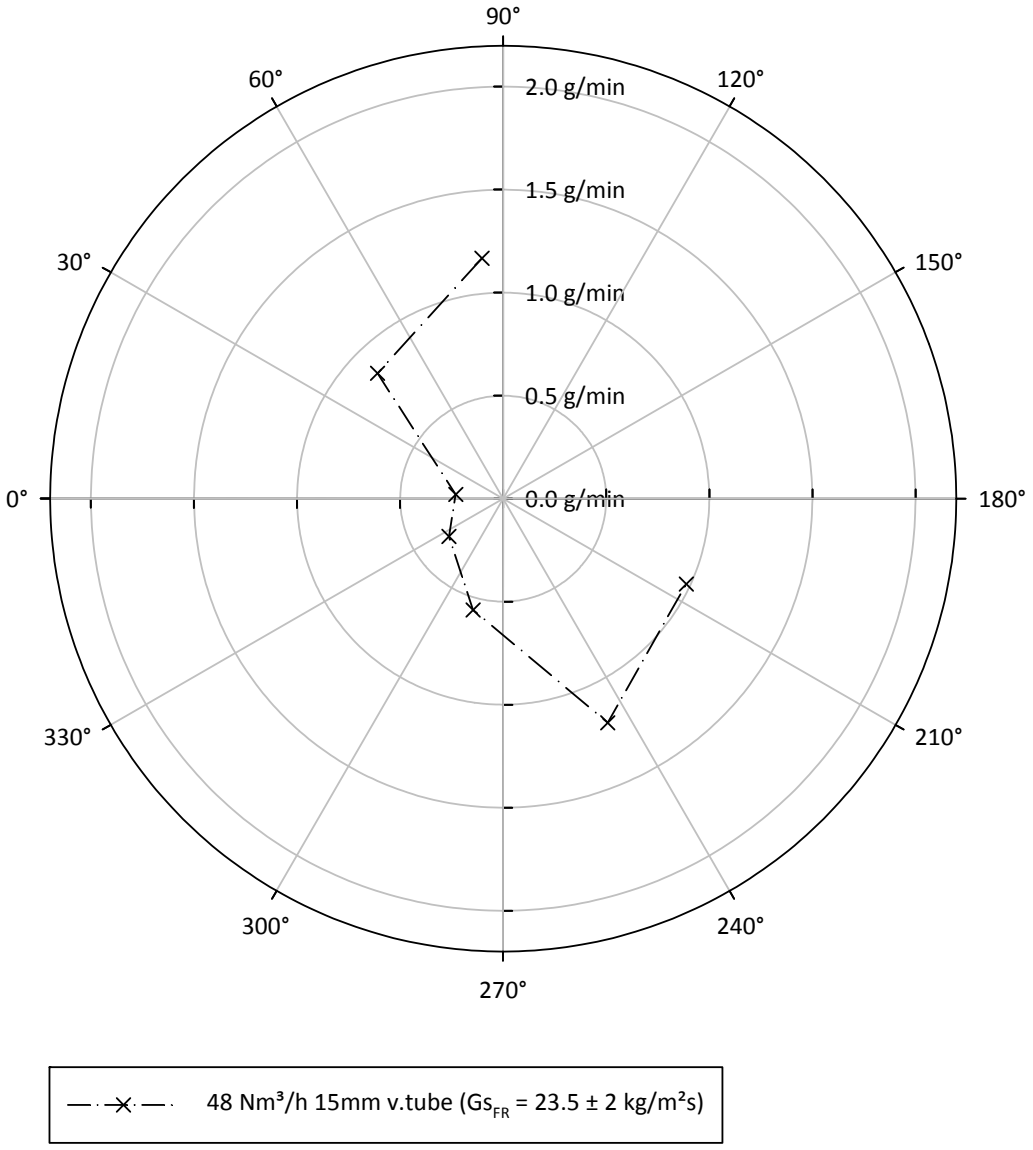

Figure 4.5: FR discharge measurements with 15 mm vortex tube and a solids flow rate of 23.5 kg/m²s

With respect to these findings the FR cyclone's vortex finder ensures a stable operation at an outlet position of 5° and a length of 15 mm. These adjustments are maintained in the following experiments.

Figure 4.6 shows the influence of the vortex tube depth on the pressure drop and the discharge. As previous experiments showed, the discharge decreases with higher vortex depths. The high pressure drop at 0 mm can be explained with the high solids flow out of the cyclone, which causes a higher pressure drop. The increasing of the pressure drop at higher vortex depths is expected because of higher flow losses.

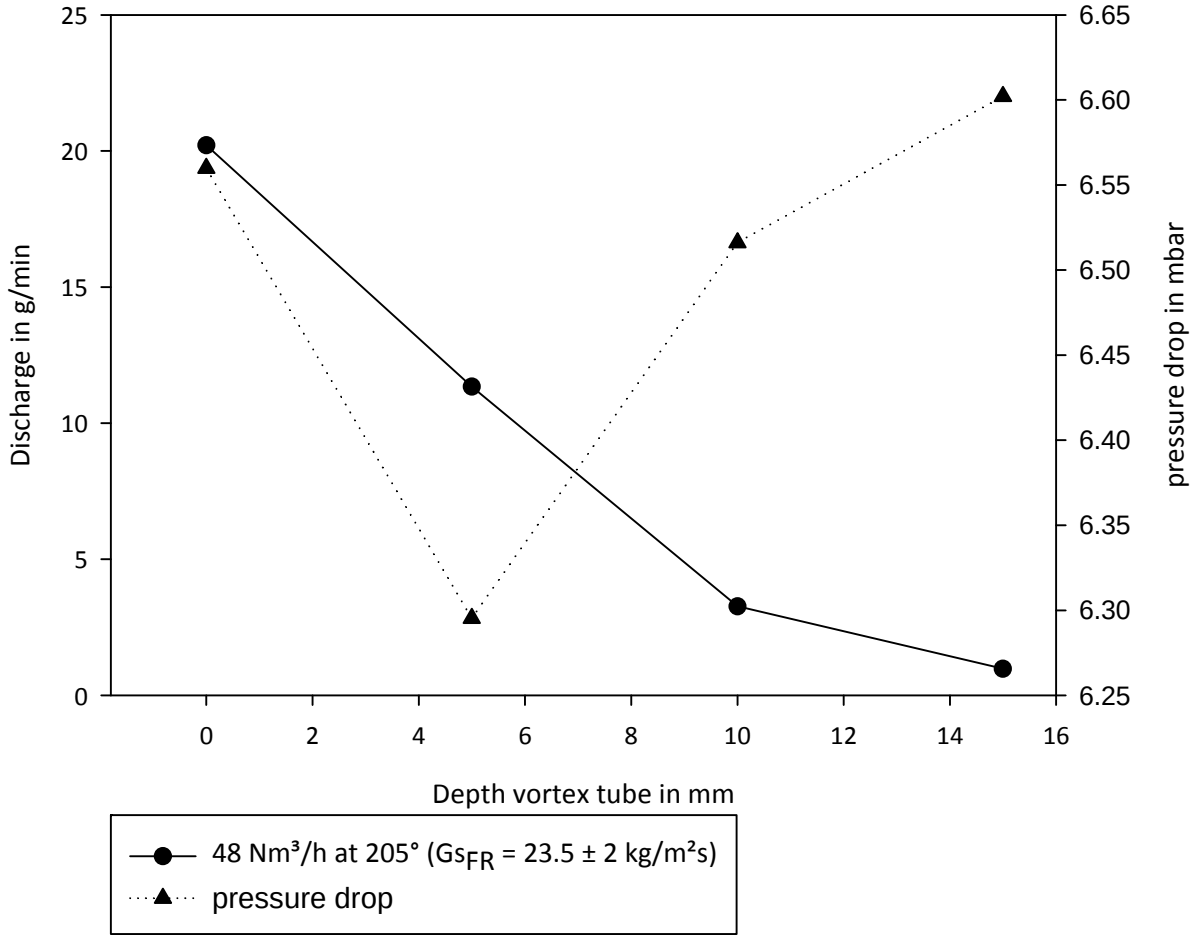

Figure 4.6: Dependence of discharge and pressure drop on vortex tube depth at an outlet position of 205° and 48 Nm³/h air flux.

Table 4.3 summarizes the achieved reductions of the cyclones discharge for the AR and the FR. It is important to consider that the design case measurements of the AR are executed with 30 kg global inventory. This leads to smaller solids circulation rates and therefore to smaller discharges. In respect to this the effective reduction of the AR is slightly higher than 47.9.

Table 4.3: Summary of achieved discharge reductions for AR and FR with 35 kg global inventory and design air flow rates in the cyclone

	Design case			**Optimized**			
	outlet position	vortex tube depth	discharge	outlet position	vortex tube depth	discharge	**Reduction**
	°	mm	g/min	°	mm	g/min	$^{design}/_{optimised}$
AR	45	0	86.2*	285	15	1.8	47.9
FR	45	0	11.35	5	15	0.25	45.4

*30 kg global inventory

The previous experiments, in special the discharge experiments, showed a high influence of the active bed material on the solids flow rates.

4.3 Optimization of the loop seals

4.3.1 Lower loop seal (LLS)

The results of the loop seal operation optimization are presented in Figure 4.7. It shows how the solids throughput of the lower loop seal is affected by fluidization conditions. At low fluidization rates the increase of friction inhibits solids motion. Anyhow, even stopping loop seal fluidization in one area cannot provoke loop seal blockage. This means that even in this case the inner friction of the loop seal is smaller than the pressure of the solids in the loop seal inlet. While the loop seal solids throughput increased constantly with fluidization of the outlet and centre area, an inhibition of solids motion with fluidization of the loop seal inlet area is observed. This is obviouly caused by the increasing air stream in adverse direction of the bed material flow.

As the minimum fluidization for centre variation is 200 Nl/h higher than the others, the solids flow rate starts at a higher level. After a period of nearly constant slope the loop seal is a kind of saturated and fluidization looses its influence on the solids flow rate. The outlet variation reaches slightly higher circulation rates than the centre variation.

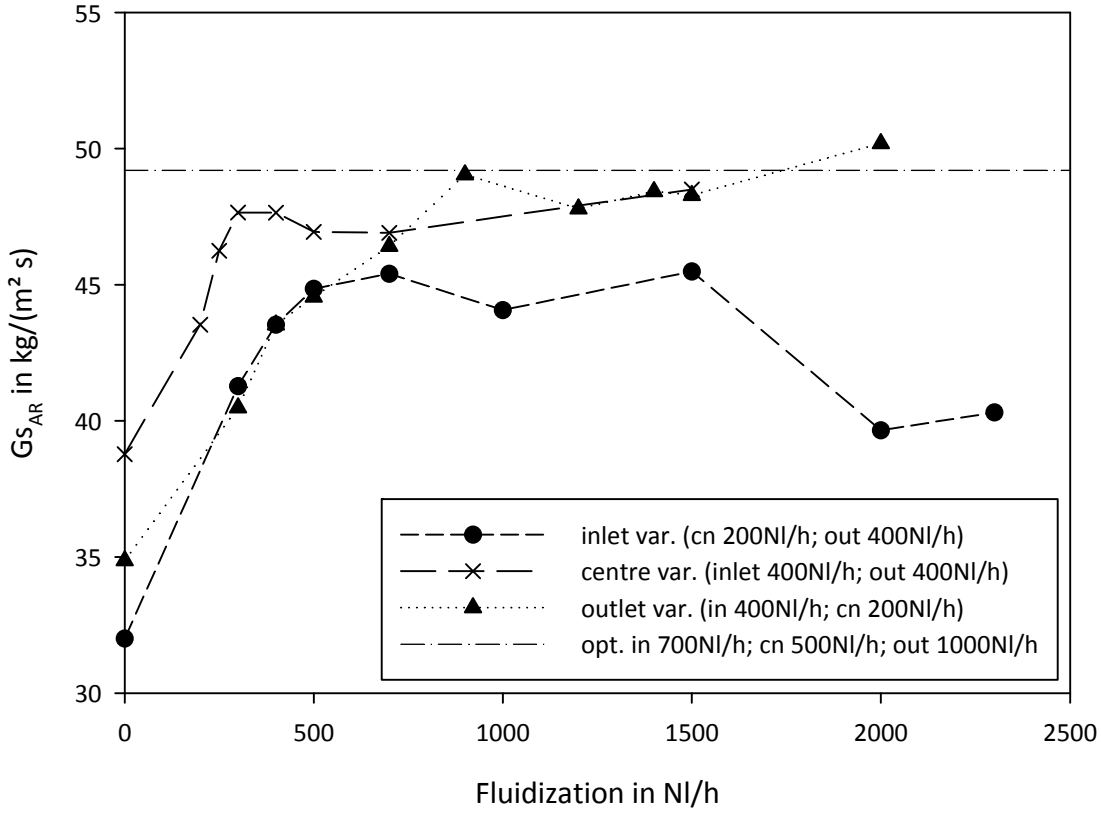

Figure 4.7: Dependence of solids flow rate on LLS fluidization with 35 kg solids inventory

The dot dashed line in Figure 4.7 shows the chosen optimized fluidization for the LLS, where the inlet area is fluidized with 700 Nl/h, the centre with 500 Nl/h and the outlet with 1000 Nl/h. The comparison of the design and the optimized fluidization are presented in Table 4.4. As one can see, the reduction of operating material is 400 Nl/h, which would lead to a significant reduction of steam requirement in the full scale plant.

Table 4.4: Fluidization of LLS in design and optimized conditions in Nl/h

	Design	Optimized	Reduction	
	Nl/h	Nl/h	Nl/h	%
Inlet	1100	700	400	36.4
Centre	400	500	-100	-25
Outlet	1100	1000	100	9.1
Sum	2600	2200	400	15.4

4.3.2 Upper loop seal (ULS)

The upper loop seal shows a similar behavior like the LLS, as displayed in Figure 4.8. At low fluidizations the global solids flow increases proportionally to fluidization and changes to nearly constant values at higher velocities. The starting gab of the centre variation is caused by different constant fluidization of the loop seals. This causes a difference of 100 Nl/h. The value at 0 Nl/h inlet fluidization is missing, because the loop seal is getting blocked and the bed material accumulates in the downcomer. The reaction of the system, which occurs at high inlet fluidization in the LLS, cannot be identified. This effect may occur at higher inlet fluidizations which are not measured because of the limited variable area flow meter range.

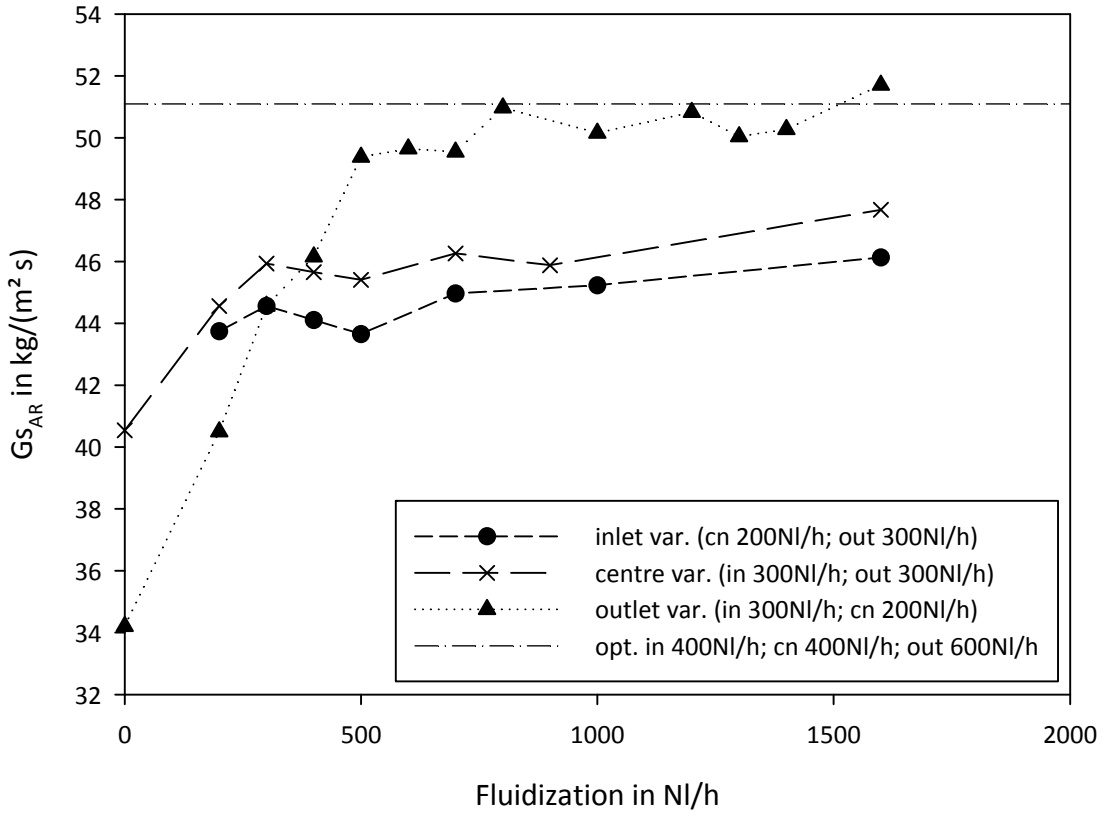

Figure 4.8: Dependence of solids flow rate on ULS fluidization with 35 kg solids inventory

Compared with the LLS the influence of the outlet air velocity is higher at the ULS. This is due to the construction of the loop seal. The difference is that bed material has to overcome the barrier to get into the FR. So if the velocity in the outlet is higher, more bed material gets over the barrier and leaves the loop seal. In the AR the bed material had to be transported away by the fluidization air.

Figure 4.8 also shows the optimized solids flow rate (51.1 kg/m²s), which is displayed as dot dashed line, where the inlet is fluidized with 400 Nl/h, the centre with 400 Nl/h and the outlet with 600 Nl/h. The comparison and possible reduction of the needed fluidization air is summed up in Table 4.5. The reached reduction is 600Nl/h, which is a reduction of 30% of the needed operating material.

Table 4.5: Fluidization of ULS in design and optimized conditions in Nl/h

	Design	Optimized	Reduction	
	Nl/h	Nl/h	Nl/h	%
Inlet	750	400	350	46.7
Centre	500	400	100	20
Outlet	750	600	150	20
Sum	2000	1400	600	30

4.3.3 Internal loop seal (ILS)

Figure 4.9 shows the results of the internal loop seals optimization. Differently from the other loop seals the ILS doesn't reach a constant solids flow for increasing inlet fluidization. This may occur because it is much smaller than the others and the air from the inlet leak throw to the outlet at high gas velocities. This effect is enhanced at the centre fluidization. Therefore it correlates with the outlet influence. The second affect which relies on the loop seals size is that the wall friction effects block solids flow at very low fluidization rates under 100 Nl/h in all areas.

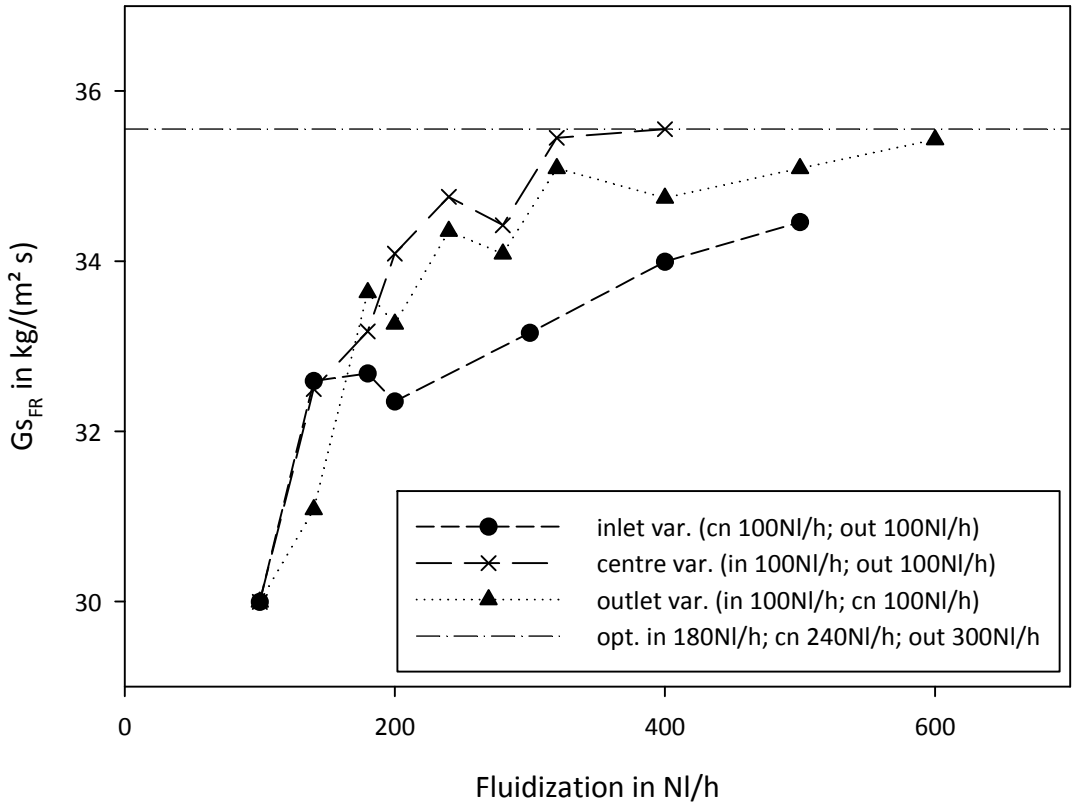

Figure 4.9: Dependence of solids flow rate on ILS fluidization with 35 kg solids inventory

As Table 4.6 shows, the air support which is needed for the internal loop seal couldn't be reduced. But the air distribution is changed slightly. The dot dashed line displays the solids flow rate in the FR at the new optimized conditions given in Table 4.6.

Table 4.6: Fluidization of ILS in design and optimized conditions in Nl/h

	Design	**Optimized**	**Reduction**	
	Nl/h	Nl/h	Nl/h	%
Inlet	240	180	60	25
Centre	240	240	0	0
Outlet	240	300	-60	-25
Sum	720	720	0	0

The achieved reductions and the new optimized fluidization air flow rates are summed up in Table 4.7. The optimized air rates are set to new standard conditions.

Table 4.7: Summary of achieved reductions and optimized loop seal fluidizations in Nl/h

		Design	**Optimized**	**Reduction**	
		Nl/h	Nl/h	Nl/h	%
LLS	inlet	1100	700	400	36.4
	centre	400	500	-100	-25
	outlet	1100	1000	100	9.1
ULS	inlet	750	400	350	46.7
	centre	500	400	100	20
	outlet	750	600	150	20
ILS	inlet	240	180	60	25
	centre	240	240	0	0
	outlet	240	300	-60	-25
	Sum	5320	4320	1000	18.8

4.4 Linear sensitivity analysis

Figure 4.10 shows the results of the sensitivity analysis with Gs_{AR} as dependent variable. The variation of the fluidization is applied to the design fluidization rates described in chapter 3.5.1.

One can clearly see that a variation of the AR primary and the AR bottom has the highest impacts on the solids flow rate in the AR riser. This effect occurs because the bed in the bubbling fluidized bottom region is expanding with the bottom fluidization causing a solids carryover to the CFB part of the AR riser (above the AR primary fluidization nozzles).

This means that increasing the gas flow in the bottom region causes higher inventory in the circulating fluidized bed mode operated part of the AR, which causes an increase in the riser solids entrainment. In the CFB operated part of the AR the primary fluidization has the largest impact on the solids flux which is in accordance with the literature on circulating fluidized beds. This is because with higher AR primary fluidization more solids are carried to the upper riser section resulting that the AR primary fluidization has the greatest relative effect on the solids flux. Anyhow, in absolute values the fluidization in the bottom region has the largest effect since the gas flow to this region is low at design conditions.

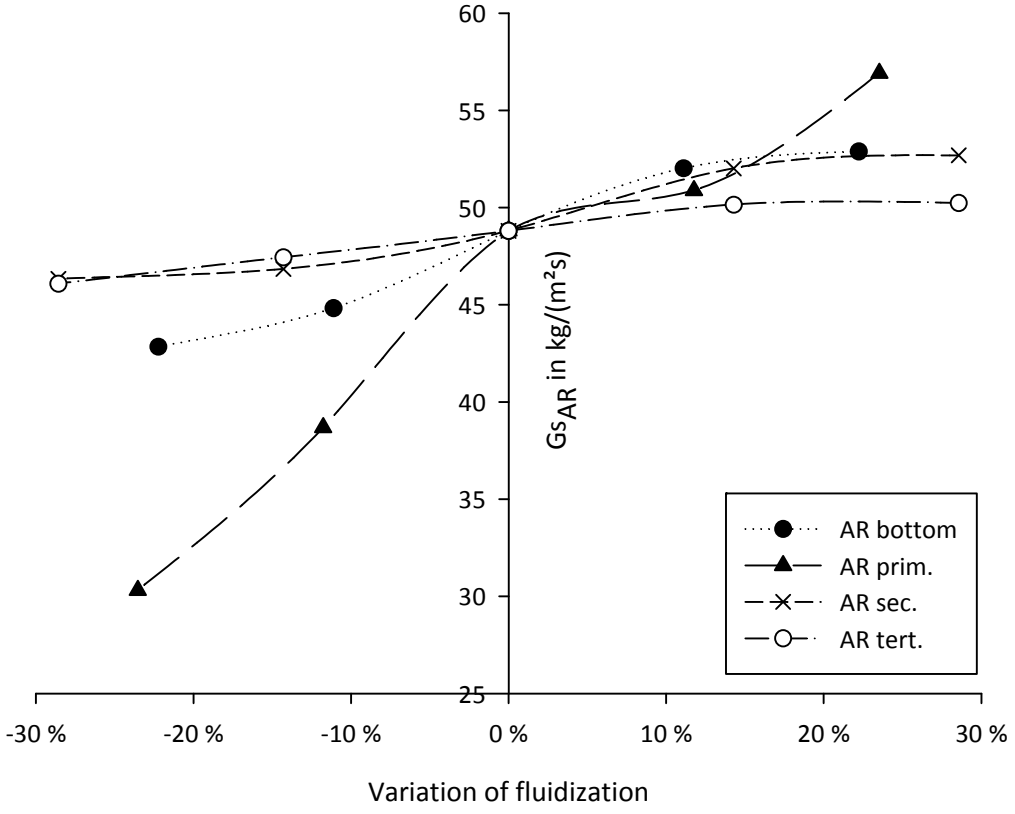

Figure 4.10: Influence of AR fluidization on Gs_{AR} with 35 kg global inventory

The AR primary influence is also, excepting the averaged standard value, nearly linear. The other dependencies are S-shaped although the influence of the AR secondary and tertiary fluidization has only a small impact on the solids flow rate in the AR riser.

Figure 4.11 depicts the bar chart of the linear sensitivity analysis for the AR solids circulation rate. The influences of fluidization are displayed as ±10% and ±20%. The inventory influence is assigned as a variation of ±14%.

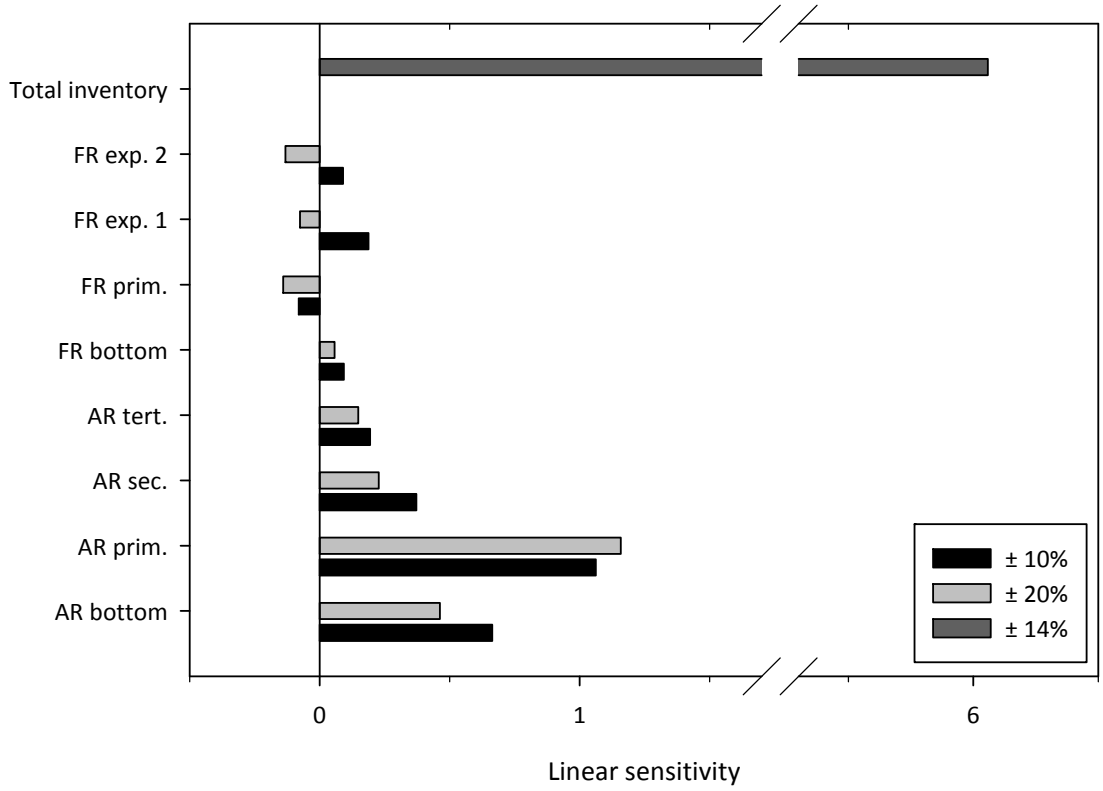

Figure 4.11: Sensitivity analysis for AR solids flow rate

It is easy to see that the inventory has a strong impact on the solids flow rate, which is about six times higher than the influence of the AR primary fluidization. As expected FR fluidization has no significant influence on the AR solids circulation rate. This effect occurs because changes in the FR fluidization conditions do not significantly influence the available bed material for the AR. The fluctuation of the FR sensitivity can be explained by the errors of the measurement method.

Figure 4.12 shows the impact of the main fluidization parameters on the FR solids flow rate. The variation is based on the design air flow rates (Table 3.7 and Table 4.7). The highest positive influence on the FR bed material circulation, which is nearly linear, has the FR primary fluidization rate (FR prim.) The impacts of the FR expansion 1 and 2 are also linear but not that high. The variation of FR bottom fluidization rate shows the same S-shaped curve as the AR bottom does in Figure 4.10

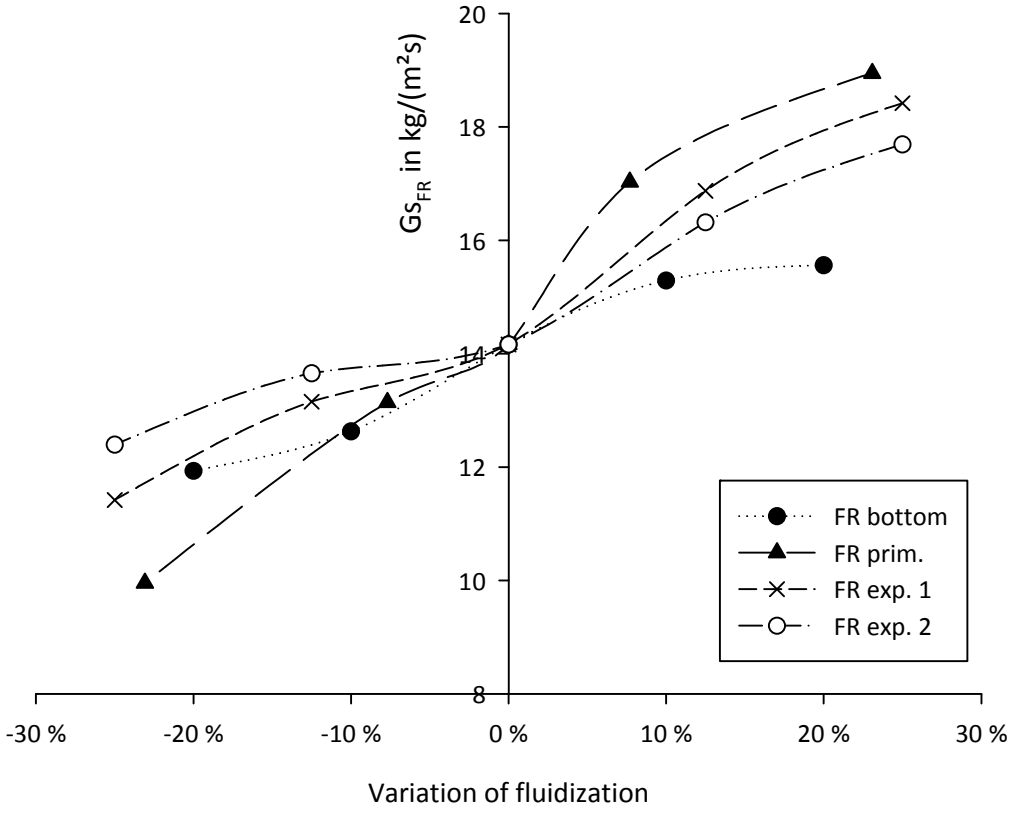

Figure 4.12: Influence of fluidization on Gs_{FR}

Figure 4.13 shows the linear sensitivity analysis for the FR solids circulation rate. The fluidization influence is displayed for ±10% and ±20%. The Inventory was varied by ±14%. Compared with the results for the AR the inventory has again the highest impact, but not that high as on the AR solids flow rate. Similar to the AR the FR primary air flow rate has the highest impact on fluidization side. The higher influence concerning the FR expansion 1 and 2 can be explained by the bed material falling down from the ILS and ULS and the different air staging in the FR riser.

Figure 4.13 also depicts that AR fluidization has a negative impact on FR circulation rate. In this case the influence of AR primary is obviously higher. This effect occurs because more bed material is distributed in the air reactor. Thus the solid flow rate in the FR decreases.

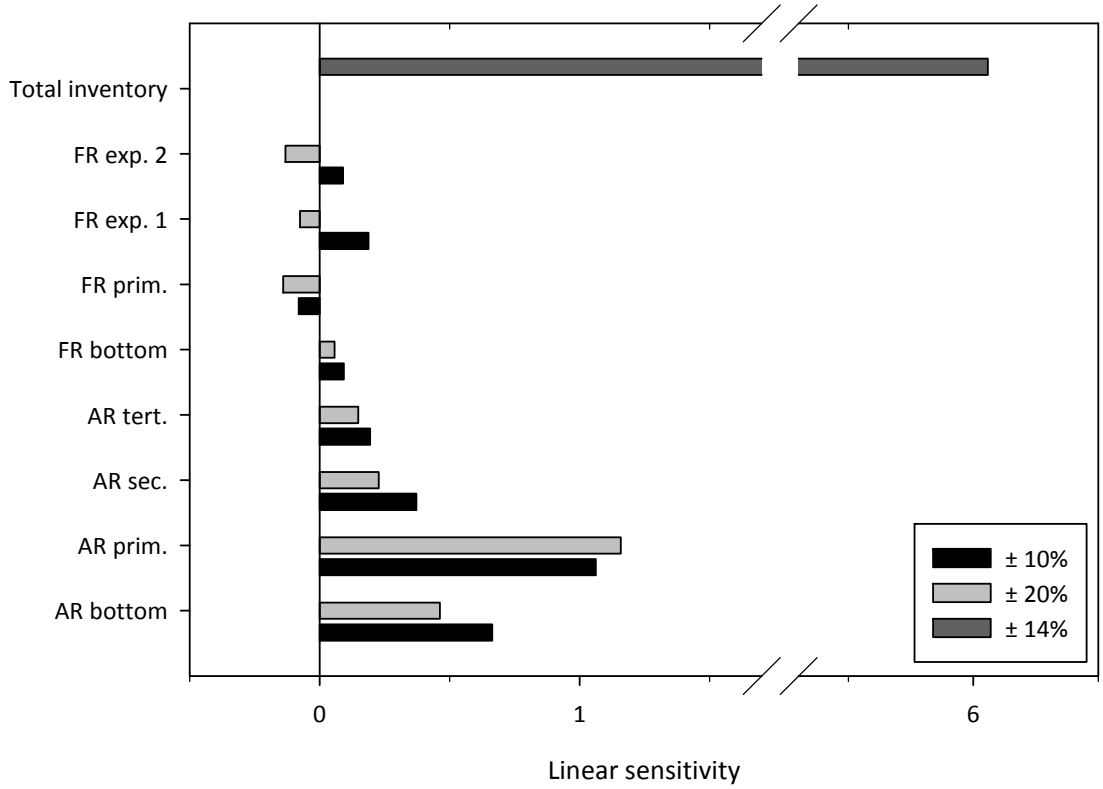

Figure 4.13: Sensitivity analysis for FR solids flow rate

As said before, AR primary has a negative influence on FR solids flow rate. This effect occurs because the higher AR fluidization rates reduce the active inventory in the FR riser an thus the FR solids flux. However the influence of AR secondary and tertiary and the bottom at ±10% are not in relevant magnitudes.

4.5 Impact of the SCV on the BMC solids flow

The Impact of the SCV on the BMC solids flow ratio is depicted in Figure 4.14. As one can see, there is a range of linear dependence from 0.6 to 2 mm SCV opening.

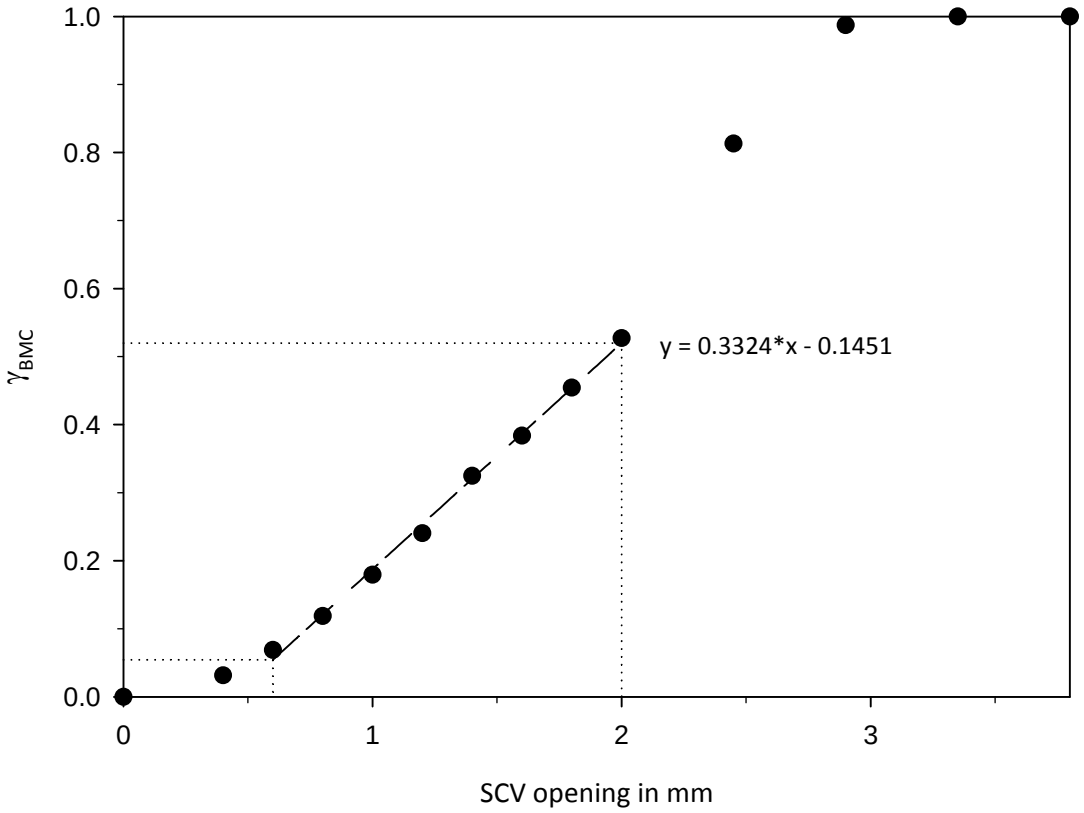

Figure 4.14: Impact of SCV opening on the BMC solids flow ratio with linear regression between 0.8 and 2 mm

Measurements show that an opening of 3.35 mm causes the complete mass to flow through the BMC. In this case no solids are transported through the ULS and the global solids circle is redirected. This point is hard to detect because the bubbling bed produces a fluctuating bed surface. Therefore a stable bed height can only be assumed. If the SCV is opened further, the ULS is running out of bed material which would cause gas leakage.

4.6 Pressure profile and solids fraction at design operating conditions

In the pressure profile (Figure 4.15) one can see a high pressure in the lower region of the FR and AR which is caused by the bubbling bed regime at the riser bottoms. In bubbling beds the pressure drop increases proportionally to the bed depth like fluids. This flow pattern changes at the height of the primary fluidization nozzles at about 220 mm, because solids concentration decreases. In the risers the pressure drop decreases only slightly.

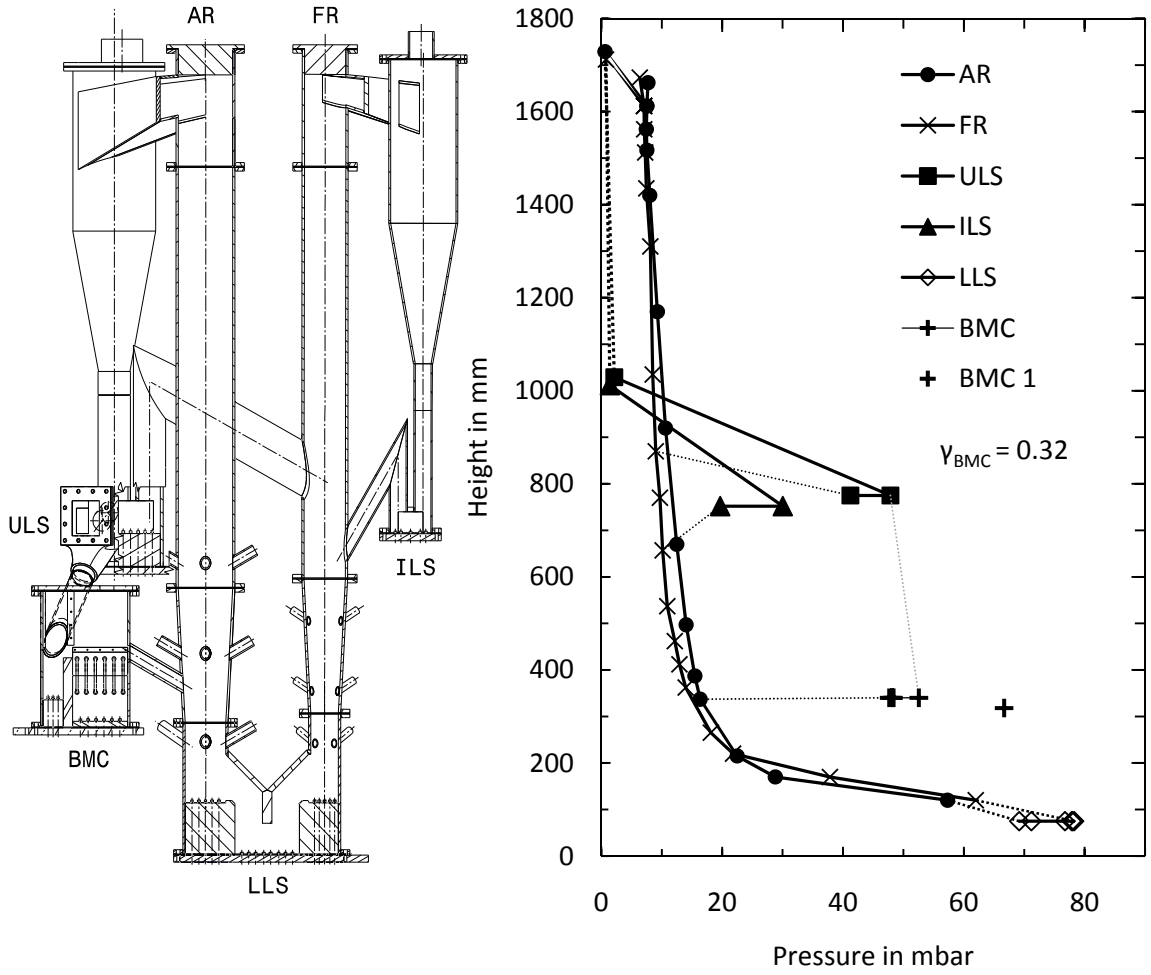

Figure 4.15: Pressure profile at design conditions for a SCV position of -1.4 mm, a AR solids flux of 42.3 kg/m²s, a FR solids flux of 15.6 kg/m²s, a BMC to AR ratio of 0.32 and 35 kg global inventory

As expected, the lowest pressure is located at the cyclone outlet where only the pressure loss in the dust filter applies. As one can see, the combined filter cyclones after the cyclones have a very low pressure drop. In the upper loop seal the accumulation of the solids in the loop seal causes a higher pressure than in the fluid beds at the specific heights. The pressure profiles show that the depth of the loop seal is sufficient for a stable operation over a wide operating range which means that the loop seal is insensitive to pressure fluctuations at the riser outlets. One can see that the pressure drop between the inlet and the outlet in the ILS is bigger than in the ULS. This effect is attributable to the higher wall-volume-ratio because of the smaller dimensions in the ILS. A higher wall-volume-ratio causes higher friction losses in the ILS and this leads to higher pressure drops.

The expected pressure drop gradient in the BMC is necessary for the bed material transport through it. The gap between BMC 1 and the others is explained by the position of this pressure port, which is placed with a 22 mm vertical spacing in relation to the other BMC pressure ports. The investigation

of different SCV positions also shows that the pressure difference in the ULS increases and the pressure difference in the BMC decreases with decreasing SCV opening. This behavior is expected because of the different material transport though the ULS and the BMC. As logical result the bed material flow distribution changes.

Figure 4.16 shows the solids fraction in the AR and FR. In the lower reactor regions the solids fraction reaches typical values of about 0.6 for bubbling bed regimes [**25**]. The solids fraction in the regions of the primary fluidization rapidly decreases to 0.02 which conforms a fast fluidizing bed with low solids fractions.

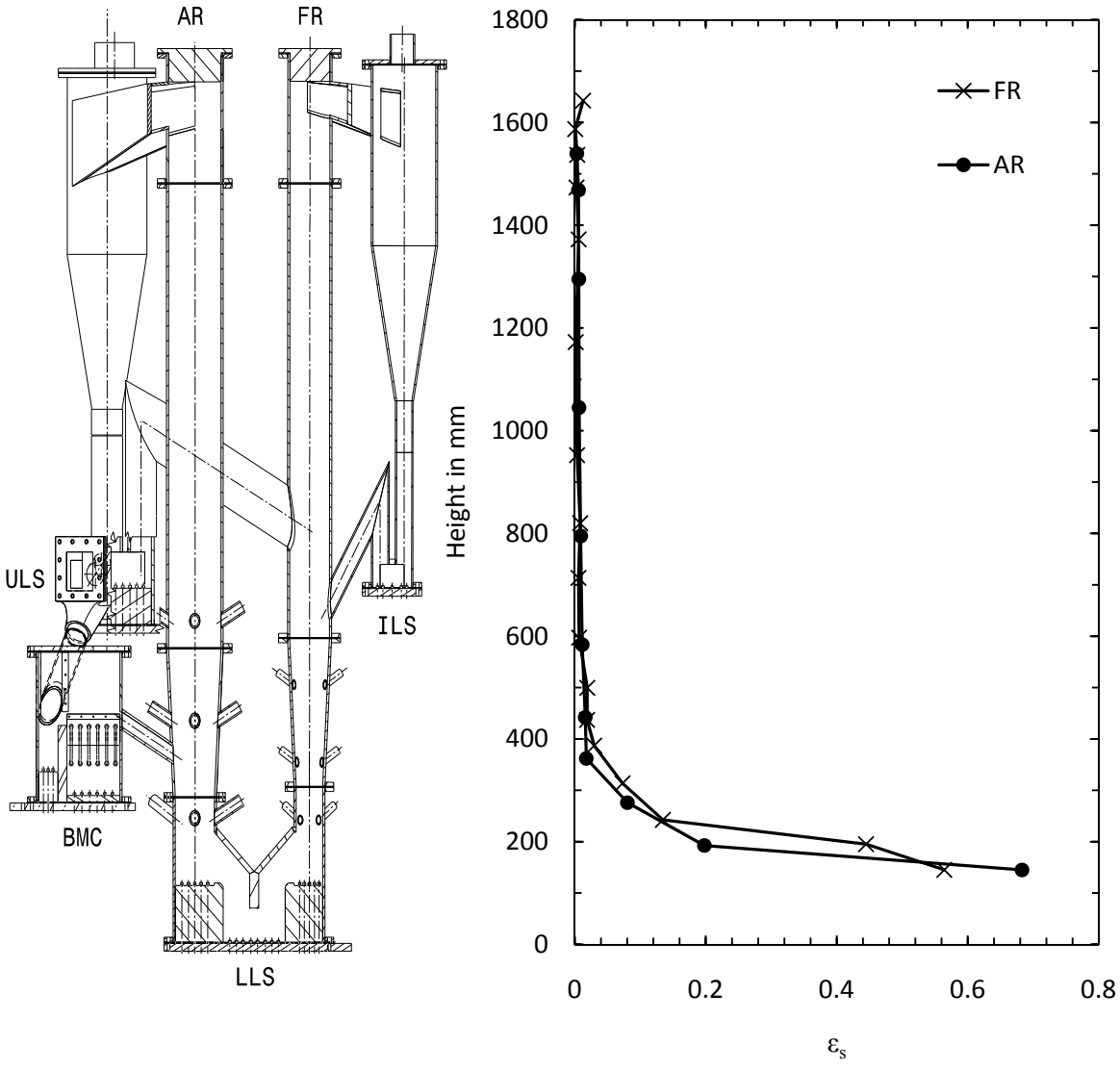

Figure 4.16: Solids fraction at design conditions with 35 kg global inventory and deactivated BMC

5 Summary, Conclusion and Outlook

5.1 Summary

The cold flow model of a 10MW CLC plant was successfully commissioned and put in operation. The pressure transmitting system was set up and a data acquisition system was developed. The evolved data acquisition system provides the possibility to control the multi phase motor of the SCV and the magnetic valves for the fluidization. It also contains an inlet pressure controller and a visualization of the current pressure profiles with an adjustable average during measurement.

The first operating hour showed that the bed material discharge of the recycle cyclones was too high to ensure a stable measurement. So the cyclones were optimized by varying the gas outlet position and installing a vortex finder. The optimal positions for the eccentrical gas outlet were found at 285° for the AR and at 5° for the FR. In both cyclones a discharge reduction of 1/50 was reached with a vortex tube and the optimal outlet position. In this way the bed material discharge could be reduced to reach stable conditions for the following investigations.

The second experimental part concerned the optimization of the loop seal fluidization. As the loop seals could be fluidized in three different areas, fluidization air can be distributed over the loop seal. This optimization was carried out for all three loop seals, whereby fluidization in one region was varied, while the others were kept on a constant low level. These investigations showed that the solids flow can be optimized by higher fluidizations at the loop seal outlet and that two high fluidizations in the inlet harm solids transport. The achieved saving in the LLS were 15% and in the ULS 30%. In the ILS no reduction was achieved, but the distribution of fluidization air was optimized.

To investigate the influence of the riser fluidization on the solids flow rate a sensitivity analysis was done. This analysis showed that the bottom and primary fluidizations have the highest impacts on the solids flux. The results also show that the FR fluidization has no significant influence on the AR solids flow rate. However a higher AR fluidization causes a slightly decreasing FR solids flux because more bed material is hold in the AR.

The global bed material inventory has clearly higher influence on the solids flow rate than fluidization. In the AR the impact is about 6 times higher and in the FR about 2 times for a bed material variation of ±14%.

The investigated characteristic of the SCV showed a linear range of the BMC/AR ratio between 0.2 and 0.6 mm opening with a gradient of 0.3324 mm^{-1}. The normal operation area of the BMC, which is necessary for part load operation, is located in this linear area. Figure 4.15 shows the pressure profile for a SCV position of -1.4 which causes a BMC/AR ratio of 0.32. The recorded pressure profiles show a typical pressure drop for circulating fluidized beds. Figure 4.15 also shows a sketch of the cold flow model, which was used. The pressure difference from ULS and ILS to the FR is high enough to ensure a stable operation of the loop seals and the ULS can react on pressure fluctuations at the cyclone output, which could occur in full scale plants. The pressure gradient from FR to AR in the LLS ensures a good solids transport between them.

5.2 Conclusion

From fluid dynamical point of view the operation of the 10 MW CLC demonstration plant is expected to be possible. The reactor design by Marx [**51**] shows a stable operation behavior with no unwanted bed material accumulations and a proper riser and loop seal fluidization. The solid control valve regulates the solids flow through the bed material cooler linear over a wide range. Bed material cooler operation works without any fluid dynamic problems like gas backflow. After some modifications the solids entrainment through the cyclones reach am acceptable value. To prevent bed material accumulations at the cyclone gas inlets, they should be fluidized or designed stepper.

5.3 Outlook

Concerning this work further interesting fields of investigation could be:

- **Loop seal leakage** investigations, because the leakage of the loop seals cause an efficiency decrease in fuel conversion and CO_2 capturing
- **Gas splitting** of the loop seals, to detect the gas streams in the loop seals
- Studies with **further bed materials**, because of new potential oxygen carriers developments
- Discharge investigations of **new cyclone designs**
- **Residence time studies** to get deeper information for the prediction of chemical reactions and conversion rates
- Design of **a full scale 10 MW hot plant** and operation

6 Nomenclature

Symbol	Notation	Dimension
$(d_p^*)_{AB}$	dimensionless particle diameter at A-B boundary	-
$(d_p^*)_{BD}$	dimensionless particle diameter at B-D boundary	-
$(d_p^*)_{CA}$	dimensionless particle diameter at C-A boundary	-
$\dot{m}_{OC}$	mass flow of oxygen carrier	kg/s
$\dot{n}_{O_2,i}$	amount of O_2	mol/h
h_{mf}	bed height at minimum fluidization	m
ϕ_s	sphericity	-
A_{AR}	AR rectangular cross-section area	m^2
A_{FR}	FR circle cross-section area	m^2
A_p	cross section area of the particle normal to the stream	m^2
C_D	drag coefficient	-
M_{O_2}	molar mass of O_2	g/mol
P_{fuel}	fuel input power	MW
$\dot{Q}$	gas flow rate	m^3/s
$Q_{r,i}$	cumulative distribution	-
R_O	oxygen capacity	-
S_P	particle surface	m^2
$S_{i,j,\pm 10\%}$	sensitivity	-
U^*	dimensionless velocity	-
U_0	superficial gas velocity	m/s
U_{mb}	minimum bubbling velocity	m/s
U_{mf}	minimum fluidization velocity	m/s
U_{ms}	minimum slugging velocity	m/s
U_t	terminal velocity	m/s
$V_{AR,exh}$	AR exhaust gas flow rate	m^3/h
$V_{FR,exh}$	FR exhaust gas flow rate	m^3/h
V_P	particle volume	m^3
V_b	bed volume	m^3
V_j	gas flow rate	m^3/h
V_{pores}	volume of pores	m^3
X_s	degree of oxidation	-
d_P	sieve diameter	m
d_{SV}	Sauter mean diameter	m
d_V	volume diameter	m
d_{eff}	effective diameter	m
d_i	diameter in class i	m
d_p	particle diameter	μm
d_p^*	dimensionless particle diameter	-
d_s	surface diameter	m

Symbol	Notation	Dimension
d_{sph}	equivalent spherical diameter	m
m_{actual}	actual mass of oxygen carrier	g
m_{ox}	molar mass reduced carrier	g
m_p	particle mass	kg
m_{red}	molar mass oxidized carrier	g
$q_{r,i}$	particle distribution density	-
x_i	particle size of the higher range end	m
x_{i-1}	particle size of the lower range end	m
μ_g	dynamic viscosity of gas	$kg/(m \cdot s)$
$\rho_{P_{abs}}$	particle density without pores and hallows	kg/m^3
ρ_b	bed density	kg/m^3
ρ_{bulk}	bulk density of bed material	kg/m^3
ρ_g	gas density	kg/m^3
ρ_p	particle density	kg/m^3
ϵ_b	voidage of fluidized bed	-
ϵ_{mf}	bed porosity at minimum fluidization	-
ϑ_{AR}	air reactor temperature	$°C$
ϑ_{FR}	fuel reactor temperature	$°C$
h	bed height	m
$\Delta H_{dir,comb}$	reaction enthalpy of the direct combustion	kJ/mol
Δh	difference in bed height	m
ΔH	reaction enthalpy	kJ/mol
Δp	pressure drop	Pa
A	cross section area of fluidized bed	m^2
Ar_{AB}	Archimedes number at A-B boundary	-
Ar_{BD}	Archimedes number at B-D boundary	-
Ar_{CA}	Archimedes number at C-A boundary	-
Ar	Archimedes number	-
D	bed diameter	m
Gs_i	bed material circulation	$kg/(m^2 \cdot s)$
H	risers height	m
Re_c	Reynolds number for change from bubbling to turbulent bed	-
Re_{mf}	Reynolds number of minimum fluidization	-
Re_{se}	Reynolds number for solids entrainment	-
g	gravitation constant	m/s^2
γ_{BMC}	mass flow ratio to BMC	-
$\dot{m}_{BMC}$	mass flow through the BMC	kg/s
t	measured time	s
β	coefficient of drag force	[**37**]

7 References

[1] Urs Siegenthaler, "Stable Carobn Cycle - Climate Relationship During the Late Pleistocene," *Science*, 2005.

[2] Josep Canadella, "Contributions to accelerating atmospheric CO2 growth from economic activity, carbon intensity and efficiency of natural sinks," *Proceedings of the Nationacl Academy of Sciences*, 2007.

[3] Intergovermental Panel of Climate Change, *Special Report on Carbon Dioxide Capture and Storage*., 2007.

[4] BMAA, "Protokoll von Kyoto zum Rahmenübereinkommen der Vereinten Nationen über Klimaänderungne samt Anlagen," *BGBl III Nr. 89/2005*, 2005.

[5] European Environment Agency. EEA. [Online]. http://www.eea.europa.eu/

[6] Ted Trainer, "Can renewables etc. solve the greenhouse problem? The negative case," *Energy Policy*, no. 38 (8), pp. 4107 - 4114, 2010.

[7] Global CCS Institute, "The global status of CCS 2012," Canberra, 2012.

[8] T. Mattisson, H. Leion, and A. Lyngfelt, "Chemical-looping with oxygen uncoupling for combustion of solid fuels," *Int. Journal of Greenhouse Gas Control*, no. 3, pp. 11-19, 2009.

[9] T. Mattisson and H. Leion, "Chemical-looping with oxygen uncoupling using CuO/ZrO2 with petroleum coke," *Fuel*, no. 88(4), pp. 683 - 690, 2009.

[10] A. Lyngfelt, B. Leckner, and T. Mattisson, "A fluidized-bed combustion process with inhernet CO2 separation; Application of chemical-looping combustion," *Chemical Engineering Science*, pp. 3101-3113, 2001.

[11] T. Pröll and H. Hofbauer, "Chemical Looping Combustion and Reforming. Proceeding of the 9th European Confernce on Industrial Furnaces and Boilers," Estoril, Portugal, 2001.

[12] P. Kolbitsch, T. Pröll, and H. Hofbauer, *Chemical looping combustion for 100% carbon capture - Desing, operation modeling of a 120kW pilot rig*., 2009.

[13] E. Jerndal, T. Mattisson, I. Thijs, F. Snijkers, and A. Lyngfelt, "NiO particles with Ca and Mg based additives produced by spraydrying," *Energy Procedia*, no. 1, pp. 479 - 486, 2009.

[14] W.K Lewis and E.R. Gilliland, "Production of pure carbon dioxide," 2,665,971, Jan 12, 1954.

[15] H.J. Richter and K.F. Knoche, "Verbesserung der Reversibilitaet von Verbrennungsprozessen," *Brennstoff-Waerme-Kraft*, pp. 205-211, 1968.

[16] M. Ishida, D. Zheng, and T. Akehata, "Evaluation of a chemical-looping-combustion power-generation system by graphic exergy analysis," *Energy*, pp. 147-154, 1987.

[17] A. Lyngfelt, B. Kronberger, J. Adánez, X. Morin, and P. Hurst, "The GRACE project. Development of oxygen carrier particles for chemical-looping combustion. Design and operation of a 10 kW chemical-looping combustor," *The 7th International Conference on Greenhouse Gas Control Technologies*, 2004.

[18] A. Lyngfelt, "Oxygen Carriers for Chemical Looping Combustion 4000h of Operational Experience," *Oil & Gas Science and Technology*, no. 66, pp. 161 - 172, 2001.

[19] Tobias Pröll, Philipp Kolbitsch, Johannes Bolhàr-Nordenkampf, and Hermann Hofbauer, "A novel dual circulating fluidized bed system for chemical looping processes," *AIChE Journal*, pp. 3255-3266, 2009.

[20] P. Markström, A. Lyngfelt, and C. Linderholm, "CHEMICAL-LOOPING COMBUSTION IN A 100 KW UNIT FOR SOLID FUELS," *21st International Conference on Fluidized Bed Combustion*, 2012.

[21] Matthias Stieß, *Mechanische Verfahrenstechnik - Partikeltechnologie 1*. Berlin Heidelberg: Springer-Verlag, 2009.

[22] D. Geldart, "Types of gas fluidization," *Powder Technology*, pp. 285-292, 1973.

[23] John R. Grace, "Contacting models and behaviour classification of gas-solid and other two-phase suspension," *The Canadian Journal of Chemical Engineering*, pp. 353-363, 1986.

[24] W.C. Yang, "Modification and re-interpretation of Geldart's classification of powders," *Powder Technology*, pp. 69-74, 2007.

[25] Daizo Kunnii and Octave Levenspiel, *Fluidization Engineering*.: Butterworth - Heinemann, 1991.

[26] H. T. Bi and J. R. Grace, "Flow regime diagrams of gas-solid fluidization and upward transport.," *International Journal of Mulitphase Flow*, vol. 5, pp. 1229-1236, 1995.

[27] D. Geldart and A. R. Abrahamsen, "Homogenous fluidization of fine powders using various gases and pressures," *Powder Technology*, vol. 1, pp. 133-136, 1978.

[28] P.S.B. Stewart and J.F. Davidson, "Slug flow in fluidised beds," *Powder Technology*, pp. 61-80, 1967.

[29] J. R. Grace, "Contacing modes and behaviour classification of gas-solid and other twophase suspensions," *The Canadian Journal of Chemical Engineering*, pp. 353-363, 1986.

[30] R. Clift, J. R. Grace, and M. E. Weber, *Bubbles, drops and particles*. New York: Academic Press, 1978.

[31] Verein Deutscher Ingenieure VDI-Gesellschaft Verfahrenstechnik und Chemieingenieurwesen, *VDI-Wärmeatlas*. Karlsruhe, Düsseldorf: Springer-Verlag, 2005.

[32] P.C. Carman, "Fluid flow through granular beds," *Transactions -*, pp. 150-166, 1937.

[33] S. Ergun, "Fluid Flow through Packed Columns," *Chemical Engineering Progress*, 1952.

[34] (2012, Dec.) dqadmin.com. [Online]. http://dqadmin.com/

[35] Ain A. Sonin, *The Physical Basis of Dimensional Analysis*. Cambridge, Massachusetts: Department of Mechanical Engineering, 2001.

[36] Organisation Intergouvernementale de la Convention du Mètre, *The International System of Units*, 8th ed. Paris: STEDI Media, 2006.

[37] L. R. Glicksman, "Scaling relationships for fluidized bed," *Chemical Engineering Science*, no. 39, pp. 1373 - 1379, 1984.

[38] T. R. Ake and L. R. Glicksman, "Scale model and full scale test results of a circulating fluidized bed combustor," *Proceedings of 1988 Seminar on Fluidized Bed Combustion Technology for Utility App.*, pp. 1-24, 1988.

[39] L. R. Glicksman, M. Hyre, and K. Woloshun, "Simplified scaling relatinosships for fluidized beds," *Powder Technology*, no. 77, pp. 177-199, 1993.

[40] O. M. Morse, "Staubsammler," DRP Nr. 39219, July 25, 1886.

[41] B. Bonn, "VGB-Konferenz "Wirbelschichtfeuerung und Dampferzeugung"," in *Umweltschutzaspekte von Wirbelschichtfeuerungssystemen*, Essen, 1988.

[42] U. Muschelknautz and E. Muschelknautz, "Separation Efficiency of Recirculating Cyclones in Circulating Fluidized Bed Combustions," *VGB PowerTech*, no. 4, pp. 48-53, 1999.

[43] M. Trefz, *Die verschiedenen Abscheidevorgänge im höher und hoch beladenen Gaszyklon unter besonderer Berücksichtigung der Sekundärströmungen*. Düsseldorf: VDI-Verlag, 1992.

[44] E. Hugi and L. Reh, "Focus on solids strand formation improves separation performance of highly loaded circulating fluidized bed recycle cyclones," *Chemical Engineering and Processing*, no. 39, pp. 263-273, 2000.

[45] S. Koppatz, M. Fuchs, S. Müller, and J.C. Schmid, *Join the research platform FUTURE ENERGY TECHNOLOGY to bring visions to life*. Vienna: Vienna University of Technology, Institute of Chemical Engineering, 2012.

[46] F. Garcia-Labiano, L.F. de Diego, J. Adánez, A. Abad, and P. Gayán, "Reduction and Oxidation Kinetics of a Copper-Based Oxygen Carrier Prepared by Impregnation for Chemical-Looping Combustion," *Industrial and Engineering Chemistry Research*, no. 43, pp. 8168 - 8177, 2004.

[47] K. Marx, T. Pröll, and H. Hofbauer, "Next Scale Chemical Looping Combustion: Fluidized Bed System Design for Demonstration Unit".

[48] P. Kolbitsch, T. Pröll, J. Bolhàr-Nordenkampf, and H. Hofbauer, *Energy Procedia*, pp. 1465-1472, 2009.

[49] T. Pröll, P. Kolbitsch, J. Bolhàr-Nordenkampf, and H. Hofbauer, WO2009/021258 A1, 2009.

[50] M. A. Hamdan and A. M. Al-qaq, "The prediction of heat transfer coefficient in circulating fluidized bed combustors," *Energy Conversion and Management*, no. 49 (11), p. 3274 3277, 2008.

[51] K. Marx, T. Pröll, and H. Hofbauer, "Next scale chemical looping combustion: Fluidized bed system desing for demonstration unit".

[52] Klemens Marx, T. Pröll, and H. Hofbauer, "Next Scale Chemical Looping Combustion Project Report CLCSG PreFEED," Vienna University of Technology, 2011.

[53] Erich Hugi, *Auslegung hochbeladener Zyklonabscheider für zirkulierende Gas/Feststoff-Wirbelschicht-Reaktorsysteme*. Düsseldorf: VDI-Verlag, 1997.

[54] T. Igushi and H. Yoshida, "Investigation of low-angle laser light scattering patterns using the modified Twomey iterative method for particle sizing," *REVIEW OF SCIENTIFIC INSTRUMENTS*, 2011.

[55] Y.A. Sanmamed, D. Gonzalez-Salgado, J. Troncoso, C.A. Cerdeirina, and L. Romani, "Viscosity-induced errors in the density determination of room temperature ionic liquids using vibrating tube densitometry," *Fluid Phase Equilibrium*, pp. 96-102, 2007.

[56] K. Marx, O. Bertsch, T. Pröll, and H. Hofbauer, "Next scale chemical looping combustion: Process integration and part load investigations for a 10MW demonstration unit," *11th International Conference on Greenhouse Gas Technologies (GHGT-11)*, 2012.

8 Table of Figures

9 Table of Tables

10 Appendix

Table 10.1: Properties of pressure measurement cells

name	max pressure	port		pressure transmitter
	[mbar]	multiplug	measurement cards	
CAR 1	100	-	card 1.28	EPCOS AUR 0.100 F C4 TN H S2.0
CAR 2	50	lower 1	card 2.1	Kalinsky DS2-420
CAR 3	50	lower 2	card 2.2	Kalinsky DS2-420
CAR 4	250	lower 12	card 2.12	Kalinsky DS2-420
AR 1	500	lower 25	card 2.25	Kalinsky DS2-420
AR 2	250	lower 13	card 2.13	Kalinsky DS2-420
AR 3	250	lower 14	card 2.14	Kalinsky DS2-420
AR 4	250	lower 15	card 2.15	Kalinsky DS2-420
AR 5	250	lower 16	card 2.16	Kalinsky DS2-420
AR 6	250	lower 17	card 2.17	Kalinsky DS2-420
AR 7	250	lower 18	card 2.18	Kalinsky DS2-420
AR 8	100	lower 6	card 2.6	Kalinsky DS2-420
AR 9	100	lower 7	card 2.7	Kalinsky DS2-420
AR 10	100	lower 8	card 2.8	Kalinsky DS2-420
AR 11	100	lower 9	card 2.9	Kalinsky DS2-420
AR 12	100	lower 12	card 2.12	Kalinsky DS2-420
AR 13	50	lower3	card 2.3	Kalinsky DS2-420
AR 14	50	lower 4	card 2.4	Kalinsky DS2-420
FR 1	500	lower 24	card 2.24	Kalinsky DS2-420
FR 2	250	upper 13	card 1.13	Kalinsky DS2-420
FR 3	250	upper 14	card 1.14	Kalinsky DS2-420
FR 4	250	upper 15	card 1.15	Kalinsky DS2-420
FR 5	250	upper 16	card 1.16	Kalinsky DS2-420
FR 6	250	upper 17	card 1.17	Kalinsky DS2-420
FR 7	250	upper 18	card 1.18	Kalinsky DS2-420
FR 8	250	upper 19	card 1.19	Kalinsky DS2-420
FR 9	250	upper 20	card 1.20	Kalinsky DS2-420
FR 10	250	upper 21	card 1.21	Kalinsky DS2-420
FR 11	100	upper 5	card 1.5	Kalinsky DS2-420
FR 12	100	upper 6	card 1.6	Kalinsky DS2-420
FR 13	100	upper 7	card 1.7	Kalinsky DS2-420
FR 14	100	upper 8	card 1.8	Kalinsky DS2-420
FR 15	100	upper 9	card 1.9	Kalinsky DS2-420
FR 16	100	upper 10	card 1.10	Kalinsky DS2-420
FR 17	100	lower 5	card 2.5	Kalinsky DS2-420
FR 18	50	upper 3	card 1.3	Kalinsky DS2-420
FR 19	50	upper 4	card 1.4	Kalinsky DS2-420
CFR 1	100	-	card 1.27	EPCOS AUR 0.100 F C4 TN H S2.0
CFR 2	50	upper 1	card 1.1	Kalinsky DS2-420
CFR 3	50	upper 2	card 1.2	Kalinsky DS2-420
CFR 4	250	upper 12	card 1.12	Kalinsky DS2-420
BMC 1	250	lower 19	card 2.19	Kalinsky DS2-420
BMC 2	250	lower11	card 2.11	Kalinsky DS2-420
BMC 3	250	lower 20	card 2.20	Kalinsky DS2-420
BMC 4	250	upper 11	card 1.11	Kalinsky DS2-420
BMC 5	250	lower 21	card 2.21	Kalinsky DS2-420
LLS 1	500	lower 22	card 2.22	Kalinsky DS2-420
LLS 2	500	upper 22	card 1.22	Kalinsky DS2-420
LLS 3	500	upper 23	card 1.23	Kalinsky DS2-420
LLS 4	500	upper 24	card 1.24	Kalinsky DS2-420
LLS 5	500	upper 25	card 1.25	Kalinsky DS2-420
LLS6	500	lower 23	card 2.23	Kalinsky DS2-420